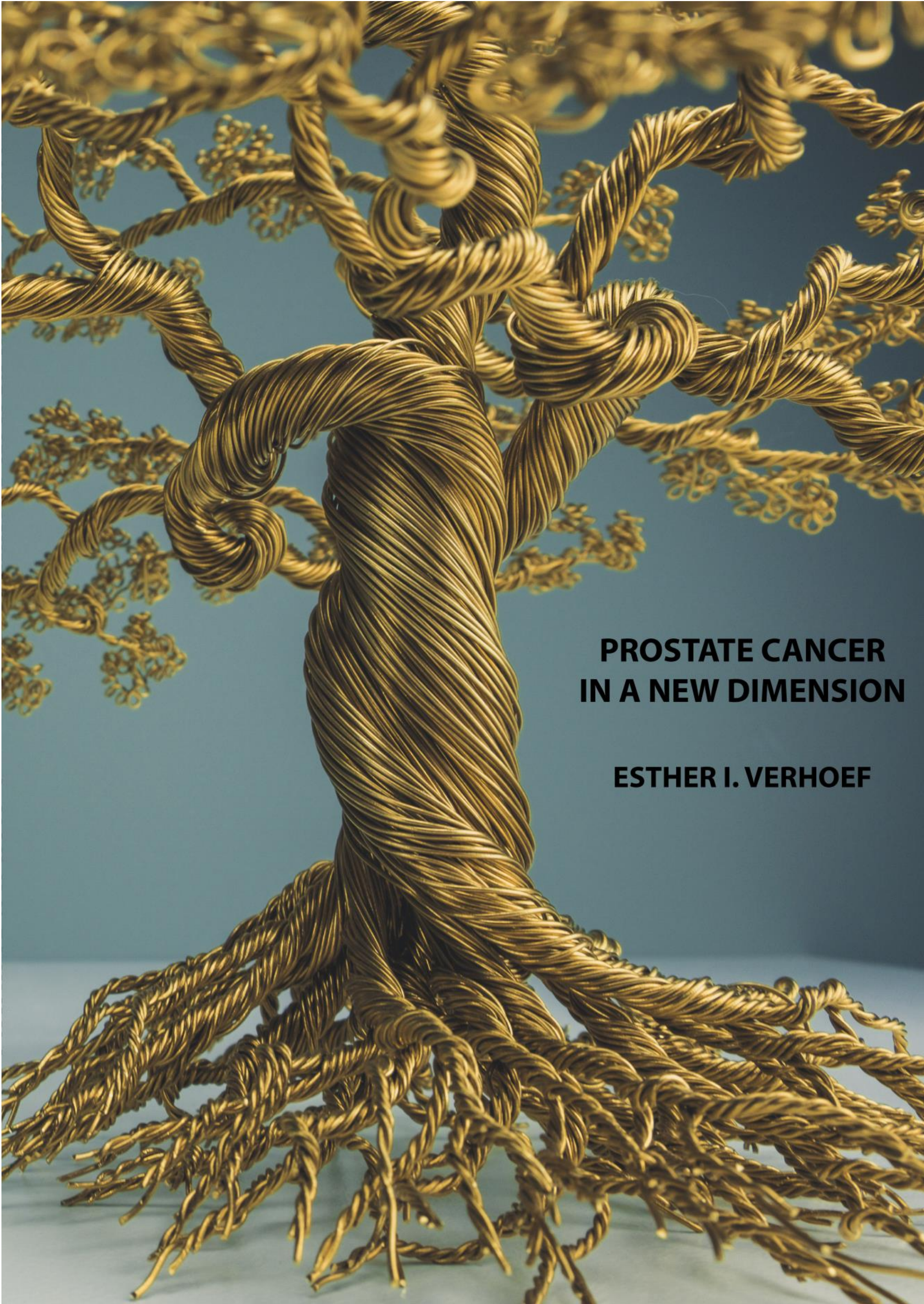

PROSTATE CANCER IN A NEW DIMENSION

ESTHER I. VERHOEF

COLOFON

Esther I. Verhoef

Prostate cancer in a new dimension
Lay-out: Esther I. Verhoef
Printed by: Gildeprint

The research described in this thesis was conducted at the Department of Pathology, Erasmus MC Cancer Institute, University Medical Center, Rotterdam, the Netherlands.

Printing of this thesis was kindly supported by Philips Research and Erasmus MC.

PROSTATE CANCER IN A NEW DIMENSION

PROSTAATKANKER IN EEN NIEUWE DIMENSIE

Proefschrift

ter verkrijging van de graad van doctor aan de
Erasmus Universiteit Rotterdam
op gezag van de rector magnificus

Prof.dr. R.C.M.E. Engels

en volgens besluit van het College voor Promoties.

De openbare verdediging zal plaatsvinden op
8 september 2020
door
Esther Ilona Verhoef
geboren te Dordrecht.

Erasmus University Rotterdam

PROMOTIECOMMISSIE

Promotor: Prof.dr. F.J. van Kemenade

Overige leden: Prof.dr. G.W. Jenster
Dr. R. Pelger
Dr. J. Kalkman

Copromotor: Dr. G.J.L.H. van Leenders

CONTENTS

CHAPTER I

General introduction

The prostate

The prostate is a male gland located in the pelvis underneath the bladder, surrounding the urethra. It consists of fibromuscular stroma and glandular tissue, of which the last is responsible for prostate fluid production. This fluid is slightly acidic and nourishes and protects sperm. The prostate glands consist of luminal epithelial cells on the inside surrounded by a flat layer of basal cells on the outside. Within the prostate, four different zones can be defined, of which the peripheral zone, located on the outside, and transition zone, located in the middle, are the zones mostly affected by disease.

The most commonly known affection of the prostate is benign prostate hyperplasia, which is an increase in the number of luminal and basal epithelial cells within the glands of the transition zone. As a result, the glands increase in size and this often leads to compression of the urethra and obstruction of the lower urinary tract, causing difficulties with urinating. Benign prostate hyperplasia is very common and occurs in most men over 75 years of age. It can be treated with medication or by trans-urethral resection, where small pieces of the transition zone constricting the urethra are surgically removed.

In contrast to benign prostate hyperplasia, prostate cancer usually arises in the peripheral zone and is characterised by abnormal growth and crowding of malignant prostate glands. In 1853, dr. Adams was the first surgeon to describe prostate cancer based on histological evaluation.[1] These malignant glands lack the basal cell layer and are lined by luminal epithelial cells only. In contrast to normal glands, they can invade into the surrounding fibromuscular tissue. Most prostate cancers are small and do not cause any symptoms, however more aggressive prostate cancer might cause urinary problems or blood in the urine. Most commonly, prostate cancers are found via a digital rectal examination or elevated serum prostate specific antigen (PSA). When an elevated PSA is detected in the blood, the urologist takes needle biopsies to establish the presence of prostate cancer. About 10 to 12 biopsies are routinely taken and processed for pathologic review. Men with clinically insignificant prostate cancer are usually put on active surveillance and are checked by the urologist annually.

Although most men do not have clinical significant or life-threatening prostate cancer, a high percentage of the patients undergoes active treatment. The urologist can either remove the prostate in the form of a radical prostatectomy, or recommend radiotherapy or hormonal therapy. All treatments are associated with side effects such as urinary incontinence, ejaculatory problems and erectile dysfunction. Radiotherapy is also applied in case the tumour recurs after surgery. Even though it is the most diagnosed form of cancer in Western men and approximately one out of six men above the age of 60 will develop prostate cancer, only one in 33 men will die of the disease.[2]

Prostate cancer pathology

Developments in the field of pathology in terms of tissue slicing and staining started in the 19th century with the introduction of the microscope, tissue fixation and embedding, and subsequent thin slicing.[3] Nowadays, tissue is collected after biopsy or operation, then thoroughly fixated with formalin and finally embedded in paraffin. Within the Erasmus MC, every prostate biopsy core is collected, fixated and embedded separately, ensuring adequate recording of the biopsy site. The embedded biopsies are then sectioned and stained at three levels to ensure adequate visualisation of the total biopsy core, as fewer levels may miss foci of cancer. To visualise different structures and cellular properties of the tissue, contrast is applied by means of the hematoxylin and eosin (HE) stain, which counts as the cornerstone of pathology.[4] The HE stain colours the nuclei of the cells violet and the cytoplasm of the cells pink. In addition, a broad range of specific protein-targeting antibodies is available to distinguish specific cells or cell types, visualised by immunohistochemistry.[5]

After staining, the tissue is examined by the pathologist. In case of prostate cancer, the tumour is graded microscopically using the Gleason scoring system, developed by Donald Gleason in the 1960s and used worldwide. This grading system is based on the great variability of growth patterns of the cancerous glands on histological slides and their varying prognosis.[6] Five different prostate cancer grades are recognised and a higher grade is associated with a more aggressive cancer. Since most patients show presence of multiple growth patterns, the sum of the two most predominant grades determines the final Gleason score. Gleason grade 1 consists of small well-delineated glands which are surrounded by a nodular stroma capsule, not invading the stroma of benign prostate glands. Grade 2 shows the same morphology as grade 1 but the glands have a more variable diameter. In grade 3 the glands infiltrate the surrounding stroma but still retain a similar morphology. Grade 4 consists of less differentiated glands with a wide morphologic variability, such as poorly-formed glands with irregular lumens and shapes, glomeruloid glands, fused glands and cribriform glands. Grade 5 consists of undifferentiated cells which lack obvious glandular formation and is subdivided in the patterns single cells, cords and solid fields (Fig. 1).[5, 7]

Histopathological characterisation of prostate cancer at diagnostic biopsies is important for the choice of therapy for the patient. Therefore it is important to realise that there is a high rate of undersampling when taking prostate biopsies. In up to 40% of the cases, the Gleason score is upgraded on subsequent radical prostatectomy specimens, which can have major impact on patient outcome and management.[8] A biopsy Gleason score of ≤3+3=6 is considered clinically insignificant and active treatment is often not necessary. On the other hand, patients with Gleason score ≥3+4=7 usually receive active treatment for their disease. Recent studies have shown that the individual growth patterns in Gleason score ≥3+4=7 have prognostic value as well. Currently, many pathologists do not mention these patterns separately in their reports. Especially for the cribriform growth pattern, it is of importance to investigate the rate of undersampling, for patients with presence of cribriform growth have adverse outcome.[9]

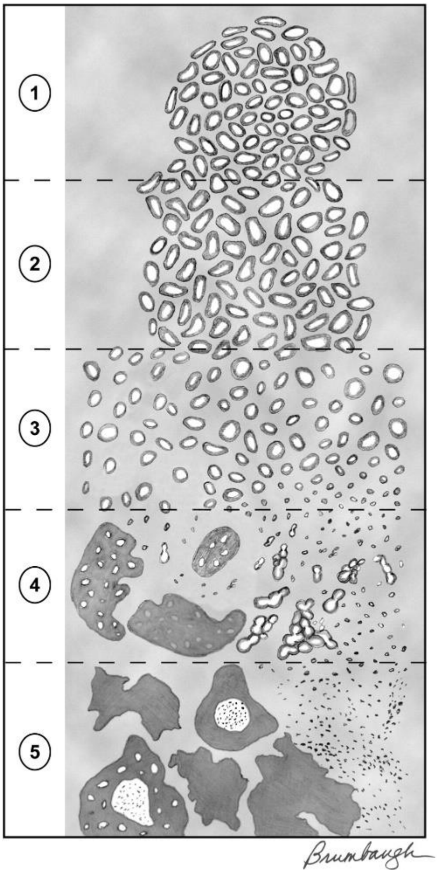

Figure 1. Gleason grading according to the International Society of Urological Pathology 2014 consensus meeting.[6]

Prostate biopsy processing and grading

Pathology reports of prostate biopsies contain detailed histopathological characterisation of the tumour. For each prostate cancer positive biopsy for instance the Gleason score and extent of cancer are mentioned. In addition, high-grade prostate epithelial neoplasia and intraductal carcinoma are reported separately.[10] However, these aberrant glands do not influence the cancer grade. Presence of perineural invasion is usually also reported.[11]

In case the distinction between prostate cancer and benign lesions is not evident, immunohistochemical stainings can be done. To discern cancer from benign mimickers, a basal cell staining such as Keratin 5 or p63 may be done to visualise the presence or absence of basal cells. However, the basal layer is not always evident in benign lesions mimicking prostate cancer, and therefore additional stainings may be performed. For instance, in the majority of cases prostate cancer strongly expresses the alpha-methylacyl-CoA-racemace (AMACR) protein, which is a clear marker to confirm the definitive diagnosis.[12] More recently available immunostaining for the ETS-related gene (ERG) can also be used, for it is a very specific prostate cancer marker, however this protein is only present in 50% of the prostate cancer patients.[13]

When prostate cancer is diagnosed, a Gleason score is assigned to each individual biopsy core. However, due to tumour heterogeneity individual cores might have a different Gleason score. In this case, an overall Gleason might be given for the entire case. At this moment it is not clear yet whether the individual Gleason score or the overall Gleason score for the entire case should be used for clinical decision making.

The pathology report also states the tumour extent of the biopsies containing prostate cancer. However, the parameter for reporting tumour extent on prostate biopsies has not yet been standardised. Several parameters have been proposed as measure of tumour extent, for example absolute tumour length, tumour percentage of only prostate cancer positive cores and tumour percentage of all biopsies including the negative cores.[14] Both absolute tumour length and tumour percentage have been associated with pathological staging and outcome after radical prostatectomy.[15-18] Tumour length is usually measured using a ruler, whereas tumour percentages are often estimated by eye-balling. It is not yet clear whether all different tumour volume parameters have a similar prognostic value and this should be studied further.

Three-dimensional imaging

Recently, it has been shown that individual Gleason growth patterns have distinct prognostic impart. Pathologic reporting and biological investigation of individual growth patterns will give better clinical and mechanistic insight in prostate cancer, and therefore it is important to define these growth patterns. However, routine pathological grading is done on thin sectioned tissue slices of approximately 5 µm whilst prostate cancer grows three-dimensionally. Since tissue scatters light, it is not feasible to use sections much thicker than 5 µm, limiting the understanding of actual growth of the prostate cancer patterns. As the 3D morphology might elucidate mutual relations between growth patterns and explain the inter-observer variability between some growth patterns, there is need for development of a robust protocol to visualise tissue structures in their native 3D environment. The most commonly used method for 3D reconstruction is serial slicing and stacking of thin slices, which enables imaging of large areas of interest. The advantage of this technique is the preservation of pathologic features to which pathologists are accustomed. However, this method is very labour- and time intensive, and highly sensitive to cutting artefacts. Also, registration and alignment of these tissue slices can be problematic.[19, 20] Algorithms for proper alignment are under construction to develop fully automated methods to reassemble continuous volumes, whilst minimizing deformations due to bad registration.[21-25] Another disadvantage of serial slicing and stacking is that the method is tissue destructive and does not allow further analysis or staining of used slices. In the past, several studies have shown the feasibility of serial slicing in the reconstruction of prostate tissue.[26-31]

A different method to visualise 3D structures is the use of whole tissue processing and imaging, allowing full view of the structures without the need of sectioning. However, structures within the tissue are obscured by intrinsically scattered light hindering visualisation of structures at lower levels. Due to this, evaluation of thick tissue sections by light or fluorescent microscopy is limited to depths of up to 10-20 micrometre. Beyond this depth over-projection of tissue structures severely inhibits visualisation. Use of confocal laser scanning microscopy (CLSM) has enabled visualisation of structures lying deeper within the tissues, up to a depth of 70 micrometres. However, beyond this depth emitted fluorescent light is scattered by the molecular structures in the intervening tissue between the fluorescent source and the camera. Therefore imaging at deeper levels can only be performed when light scattering is eliminated through for instance clearing of the tissue by matching the refractive indexes of both tissue and surrounding medium.

A century ago Spalteholtz was the first to describe such method with a laborious clearing technique for large tissues using organic solving agents. Unfortunately this technique damaged the upper layer of the tissues and was only useful for clearing of large samples.[32, 33] Another method is the removal of fatty acids in the tissue by electrophoresis and subsequent submerging of the tissue in a clearing agent which removes scattering and allows for imaging of fluorescent proteins deep within the tissue.[34] Recently, new advances have been made in the field of solvent-based tissue clearing, which can be applied to archival fixated and embedded tissue. The clearing capacity of these new solvents is based on the dehydration of the tissue and subsequent matching of the refractive index of the tissue with that of the organic solvent, resulting in optical clearing.[35] In combination with confocal laser scanning microscopy and fluorescent immunostaining this allows visualisation of formalin-fixed, paraffin embedded tissues up to a depth of 1 mm. The recent advances create opportunities for 3D visualisation of prostate cancer tissues, enabling imaging of structures deep within the tissue.

The scope of this thesis is to reveal the three-dimensional morphology of prostate cancer and its benign mimickers and to investigate parameters predictive for patient outcome on prostate cancer biopsies. In more detail, in this thesis:

- A tissue clearing method was optimised for use with archival formalin-fixed paraffin-embedded prostate tissues (**Chapter II**). This opened the opportunity to study specific structures within their three-dimensional context, while tissue remained suitable for subsequent two-dimensional analysis.

- The three-dimensional structures of prostate epithelial structures were extensively visualised. We investigated the actual growth of common benign lesions (**Chapter III**) as well as the morphology of individual prostate cancer growth patterns (**Chapter IV**) in intact tissue samples.

- Presence of cribriform growth at biopsy and subsequent radical prostatectomy was investigated, as well as parameters predictive for outcome of patients with false-negative biopsies (**Chapter V**).

- The characteristics and outcome of prostate cancer patients with overall Gleason score 3+4=7 and highest individual Gleason score > 3+4=7 on biopsy were determined (**Chapter VI**).

- Five tumour volume parameters were compared in relation to outcome after radical prostatectomy or radiotherapy (**Chapter VII**).

CHAPTER II

Three-dimensional microscopic analysis of clinical prostate specimens

van Royen*, Verhoef EI*, Kweldam CF, van Cappellen WA, Kremers GJ,
Houtsmuller AB, van Leenders GJ

Histopathology 2016 Dec;69(6):985-992

* These authors contributed equally to this paper

ABSTRACT

Aims: Microscopic evaluation of prostate specimens for both clinical and research purposes is generally performed on 5 µm thick tissue sections. Because cross-sections give a two-dimensional (2D) representation, little is known about the actual underlying three-dimensional (3D) architectural features of benign prostate tissue and prostate cancer. The aim of this study was to show that a combination of tissue-clearing protocols and confocal microscopy can successfully be applied to investigate the 3D architecture of human prostate tissue.

Methods and results: Optical clearing of intact fresh and formalin-fixed paraffin-embedded (FFPE) clinical prostate specimens allowed us to visualise tissue structures up to a depth of 800 µm, whereas, in un-cleared tissue, detection of fluorescence was only possible up to 70 µm. Fluorescent labelling with a general nuclear dye and antibodies against cytokeratin (CK) 5 and CK 8-18 resulted in comprehensive 3D imaging of benign peripheral and transition prostate zones, as well as individual prostate cancer growth patterns. After staining, clearing and imaging, samples could still be processed for 2D (immuno)histochemical staining and DNA analysis, enabling additional molecular and diagnostic characterisation of small tissue specimens.

Conclusions: In conclusion, the applicability of 3D imaging to archival FFPE and fresh clinical specimens offers unlimited opportunities to study clinical and biological topics of interest in their actual 3D context.

INTRODUCTION

The Gleason grade is an important parameter for therapeutic decision-making and predicting outcome of patients with clinical prostate cancer, and is entirely based on architectural tumour growth patterns.[36] Pathological investigation for both diagnostic and research purposes is routinely carried out by microscopic evaluation of 4 to 5 μm thick tissue slides, resulting in a two-dimensional (2D) tissue cross-section. In fact, little is known about the actual three-dimensional (3D) architecture of diseases such as prostate cancer.

Three-dimensional microscopic tissue reconstruction has mostly been carried out by serial sectioning, staining and imaging of up to hundreds of 2D sections.[37-39] Although developments in image stacking have improved 3D reconstruction, serial slicing is laborious and sensitive to tissue deformations.[40-43] Confocal laser scanning microscopy (CLSM) allows fluorescent 3D imaging without the need of sectioning, but is limited to depths of tens of micrometres owing to scattering and absorption of emitted fluorescent light. Several protocols have recently been developed to optically clear tissue and thereby enhance the detection of emitted fluorescent light at increased tissue depths.[35, 44-48] Three-dimensional imaging by combination of tissue clearance and CLSM has predominantly been used for investigation of mouse models, sometimes primarily labelled with green fluorescent protein.[34, 46, 49] The aim of the current study was to investigate the feasibility of using tissue clearing protocols and imaging techniques on fresh and formalin-fixed paraffin-embedded (FFPE) prostate specimens, in order to analyse both clinical and biological prostate cancer features in their actual 3D context.

MATERIALS AND METHODS

Clinical specimens

Prostate samples were derived from radical prostatectomies, performed at Erasmus Medical Centre, Rotterdam, The Netherlands between September 2014 and March 2016. Use of fresh and archival tissue samples for research purposes was approved by the local Medical Ethical Committee (MEC 2011-295 and 2011-296). After arrival at the pathology department, fresh samples of 5 x 5 mm from both normal and tumour tissue were collected for 3D imaging (N=13). From each sample a 1 mm slice was cut and processed for reference 5 µm slice hematoxylin & eosin (HE) staining. Tissue samples for 3D imaging were sliced within 24 hours in ice-cold Phosphate Buffered Saline (PBS) using a vibrating blade microtome Leica VT 1200 S (Leica, Rijswijk, The Netherlands). Slices of 500 to 1000 µm thickness were fixed overnight in 1% formaldehyde in PBS at 4°C. After fixation tissue slices were washed in PBS, gradually incubated in methanol/PBS up to 100% methanol, and stored at -20°C until further processing.

Staining of formalin-fixed non-embedded tissue

Fixation, staining and clearing of fresh, non-embedded tissue was performed as described previously.[50] Briefly, fixed tissue was rehydrated in methanol/PBS gradients up to 100% PBS, and blocked in PBS-1% non-fat dry milk- 0.4% Triton X100. This was followed by incubation with RedDot2 (1:400; Biotium, Hayward, USA) fluorescent nuclear dye, or primary antibodies targeting cytokeratin (CK) 5 (1:100, ab52635; AbCam, Cambridge, UK) and CK8-18 (1:100; MS-743S, Immunologic, Duiven, The Netherlands) in PBS-1% non-fat dry milk- 0.4% Triton X100 for a minimum of 7 days. After washing in PBS/0.4% Triton X100, specimens were incubated with secondary Alexa 514- or Alexa 647-conjugated antibodies (1:200; Life Technologies, Bleiswijk, The Netherlands) in PBS-1% non-fat dry milk- 0.4% Triton X100 for 7 days. Subsequent washing steps in PBS/0.4% Triton X100 were followed by gradient tissue dehydration in methanol. Prior to clearing, tissues were incubated with a mixture of 50% methanol and 50% 1:2 benzyl alcohol:benzyl benzoate (BABB) solution (Sigma, Zwijndrecht, The Netherlands) for 10 minutes. Optical transparency was achieved after incubation with 100% BABB solution for 10 minutes. Tissue was stored in BABB at 4°C until imaging for a maximum of four weeks.

Staining of FFPE tissue

For 3D imaging of archival FFPE prostate samples (N=38), areas of interest were indicated on coverslips of HE stained slides derived from diagnostic biopsies and radical prostatectomy specimens. Punches of 500 µm thickness were collected from the corresponding FFPE block using tissue micro-array punching needles (Estigen Tissue Science, Tartu, Estonia). 3D immunofluorescent tissue staining was performed according to the iDISCO protocol.[49] Briefly, tissues were de-waxed overnight and subsequently incubated in methanol for 60 minutes, incubated in 20% dimethylsulfoxide (DMSO), 20% H_2O_2 in methanol at 4°C, followed by overnight incubation in 20% DMSO in methanol. Tissue was rehydrated gradually in methanol:PBS, followed by a blocking step with 0.2%TritonX100/10%DMSO/0.3M Glycine/PBS. Primary antibodies targeting CK5 (1:100) and CK8-18 (1:100) were incubated for 7 days in 0.2%/Tween/20-10ug/ml Heparin/5%DMSO/1%Milk/PBS at 37°C, followed by washing in 0.2% Tween20/20-10ug/ml Heparin/PBS and incubation with secondary fluorescent Alexa 514- or Alexa 647-labelled antibodies (1:200, Life Technologies, Bleiswijk, The Netherlands) in 0.2%Tween20/10ug/ml Heparin/5%DMSO/1%Milk/PBS for 7 days at 37°C. Prior to clearing, tissue was washed in 0.2%Tween20/10ug/ml Heparin/PBS overnight at 37°C, dehydrated in methanol gradients at room temperature and subsequently incubated in a mixture of 50% methanol and 50% BABB. Optical transparency was achieved in 100% BABB solution after 10 minutes incubation. After clearing, tissue was stored for a maximum of four weeks in BABB at 4°C until imaging.

Confocal microscopy

For imaging the samples were mounted in 100% BABB in glass bottom microwell dishes (MatTek corp, Ashland (MA), USA) and covered with #1 coverglasses (Menzel-Gläser, Braunschweig, Germany) to avoid direct contact of the microscope objective with the BABB. Imaging was done using an upright Leica SP5 confocal microscope **(**Leica Microsystems, Eindhoven, The Netherlands) equipped with a 20x NA1.0 APO water dipping objective with a 1.95 mm working distance through a 170 µm thick coverslip. Z-stacks were recorded with a 0.72 µm pixel size and a 1 to 3 µm step-size in Z, using a 488 Argon and a 633 HeNe laser. Emission was detected in the 525-600 nm and 643-700 nm emission ranges, respectively. To compensate loss of signal and optimise the collection of structural information, laser intensity and detector sensitivity were (semi-)automatically adjusted within a pre-set range. The settings were identical within each experiment. Images were de-convoluted using the Huygens Professional software (SVI, Hilversum, The Netherlands). 3D rendering and image editing was performed with Fiji (ImageJ 1.49s) and Amira (version 5.5.0, FEI, Hillsboro, Oregon, USA) software.[51]

Immunohistochemistry

For subsequent 2D immunohistochemistry, cleared and 3D imaged tissues were returned to 100% methanol. Methanol was replaced by ethanol, and tissue was gradually rehydrated in PBS for re-embedding in paraffin. Five micron FFPE sections of post-cleared tissues were deparaffinised and rehydrated using xylene and ethanol. Endogenous peroxidase was blocked in 0.3% H_2O_2 in PBS and heat-induced antigen retrieval was performed for 15 minutes in TRIS-EDTA buffer (pH=9; Klinipath, Duiven, The Netherlands). Primary antibodies targeting CK8-18 (1:500), CD31 (1:500; AbCam, Cambridge, USA), KI67 (1:200; DAKO, Heverlee, Belgium) and Vimentin (1:500; DAKO) diluted in normal antibody diluent (APG-500, Scytek, Utah, USA) were incubated overnight at 4°C and visualised using the Envision kit (DAKO). Slides were counterstained with hematoxylin and visualised on an Olympus BX41 light microscope (Olympus, Zoeterwoude, The Netherlands).

Molecular analysis

BABB cleared tissues were placed in methanol and rehydrated in methanol:PBS gradients. DNA from tissue punches was isolated in lysis buffer (Promega, Leiden, The Netherlands) containing 5% chelex (Bio-Rad, Veenendaal, The Netherlands) with protease K (Promega) overnight at 56°C. Protease deactivation was achieved by heating to 95°C for 10 minutes. PCR was performed with primers for housekeeping genes TBXAS1, RAG1, PLZF and AF4 for 35 cycli at 60°C. DNA from non-cleared FFPE prostate samples served as control. DNA concentration and purity were measured of 6 fresh cleared and 6 FFPE cleared tissues using the Nanodrop system (Thermo Scientific, Wilmington, USA). As a control, 0.5 mm punches of 2 non-cleared samples derived from the same patients were included.

RESULTS

Three-dimensional imaging of fresh prostate tissue

To evaluate the efficacy of tissue clearing, we first compared fluorescent staining in cleared versus non-cleared prostate tissue samples (n=4). Thick tissue slices were stained with RedDot2 and imaged using CLSM. Nuclear RedDot2 signals could be detected throughout the whole BABB cleared tissue slice of 800 µm. Without tissue clearing, the Reddot2 signal was lost at 70 µm within the tissue, and was only visible at the edges of the tissue up to a depth of 200 µm in the image stack (Fig. 1; Suppl. Fig. 1).

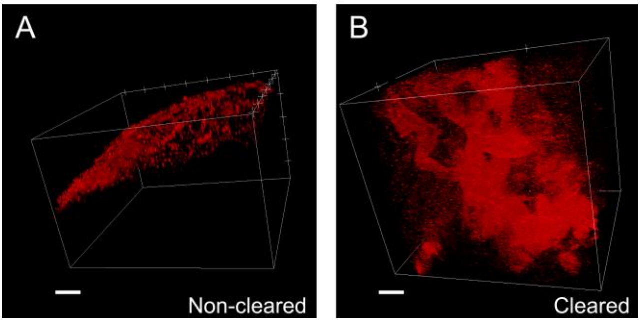

Figure 1. Tissue clearing of fresh clinical prostate cancer tissue. A three-dimensional projection of fluorescent images of A) nuclear Reddot2 in non-cleared and B) benzyl alcohol/benzyl benzoate-cleared clinical prostate tissue showed that tissue clearing enhanced the depth of imaging up to 0.8 mm. Scale bars: 100 µm.

To gain insights into 3D normal and malignant prostate glandular architecture, we performed IF double-staining for CK5 and CK8-18.[52, 53] In general, CK5 labels pre-existent basal cells surrounding CK8-18-positive luminal epithelial cells in benign prostate glands. Prostate cancer almost exclusively exists of CK8-18-positive luminal cells and lacks a CK5-positive basal cell layer.[54, 55] By using IF double-labelling, we were able to routinely image approximately 500 µm thick tissues with sufficient signal throughout the stack. In the transition zone, 2D well-delineated round glandular structures were represented in three dimensions by organised acini (Fig. 2A-D, Suppl. Video 1). In the peripheral zone, 2D longitudinal tubule sections corresponded to 3D slit-like angulated tubular spaces (Fig. 2E-H, Suppl. Video 2).

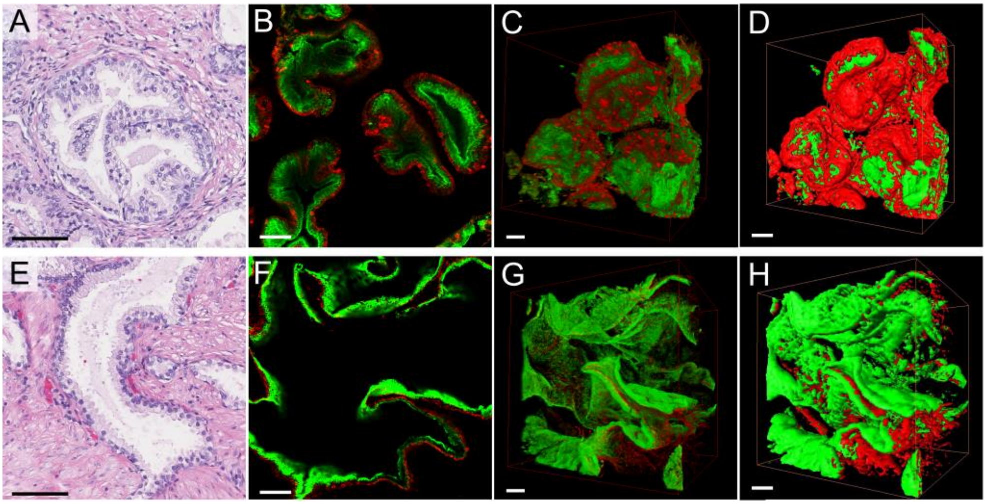

Figure 2. Three-dimensional imaging of antibody-stained fresh samples of benign prostate transition zone (A–D) and peripheral zone (E–H). A,E) Reference hematoxylin and eosin slide. B,F) Single two-dimensional optical plane of immunofluorescent cytokeratin (CK) 8-18 labelled (green) and CK5-labelled (red), benzyl alcohol/benzyl benzoate-cleared tissue. C,G,D,H) Three-dimensional projection (C,G) and 3D binary projection (D,H) of approximately 500-lm-thick tissue samples. Scale bars: 100 µm.

3D imaging of FFPE prostate tissue

The feasibility of clearing and 3D imaging on archival FFPE tissue samples was investigated at selected prostate cancer growth patterns on HE stained slides. Fig. 3A-D demonstrates closely packed well-delineated glands corresponding to Gleason score 3+3=6 prostate cancer; on HE branching and anastomosing of glands was not observed. Remarkably, 3D immunofluorescent imaging illustrated that respective prostate cancer glands actually represented an interconnecting glandular network (Suppl. Video 3). A Gleason score 7 prostate cancer consisting of well-delineated Gleason pattern 3 glands and Gleason pattern 4 with intra-luminal glomeruloid epithelial proliferations is depicted in Fig. 3E-H (Suppl. Video 4). 3D reconstruction revealed spatial transition of well-delineated Gleason pattern 3 glands and glomeruloid Gleason grade 4 patterns. The glandular structures with intra-luminal glomeruloid proliferations were continuous with well-delineated Gleason grade 3 glands, which was not appreciated in the corresponding HE slide. Fig. 3J-L depicts an area of ill-defined Gleason pattern 4 prostate cancer glands. 3D analysis revealed that these structures represented a highly anastomosing meshwork of small-sized tubules and cords of malignant cells (Suppl. Video 5). The inter observer variability of ill-defined tumour glands is relatively poor, as discriminating them from tangentially sectioned Gleason grade 3 or Gleason grade 5 is often difficult.[43] While the pattern is different from classical Gleason grade 3 (Fig. 3A-D), the 3D architectural differences between ill-defined Gleason grade 4 and Gleason grade 5 cords is not clear yet.

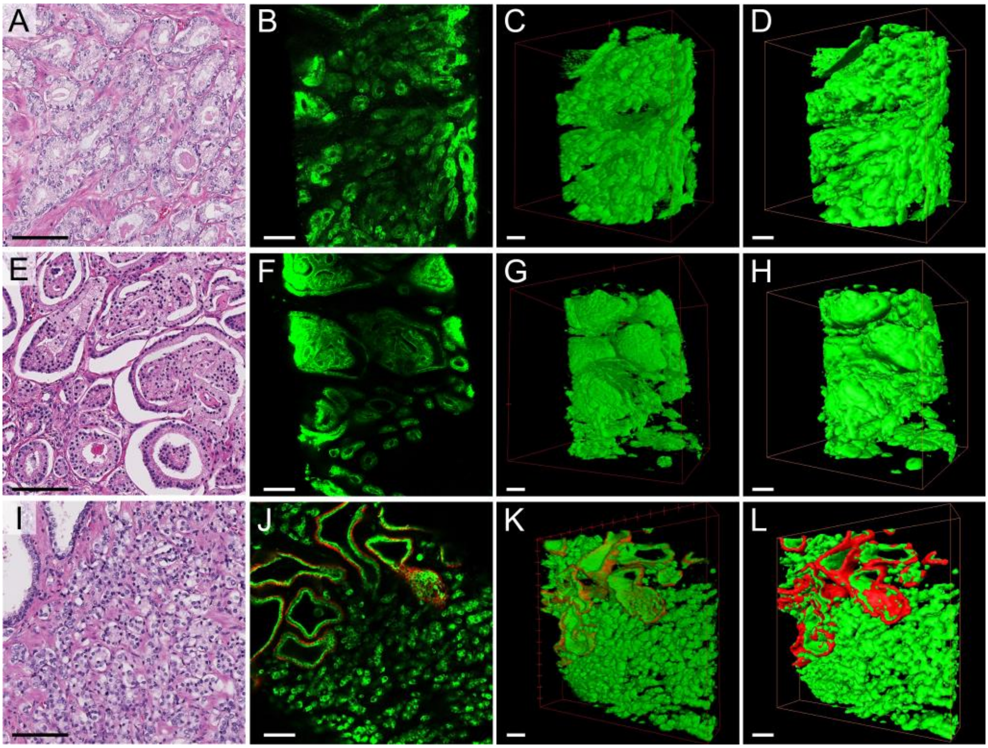

Figure 3. Three-dimensional (3D) pathology of prostate cancer growth patterns. A–D) Well-delineated Gleason grade 3 prostate cancer with regular 3D glandular interconnections. E–H) Well-delineated Gleason grade 3 and glomeruloid Gleason grade 4 glands. Three-dimensional spatial transitions between both structures exist. I–L) Three-dimensional projection of an ill-defined Gleason grade 4 gland demonstrates a highly interconnecting meshwork of small-sized tubules and cords. Vertical panels from left to right represent a reference hematoxylin and eosin slide, a single 2D optical plane of immunofluorescent cytokeratin (CK) 8-18-labelled (green) and CK5-labelled (red) benzyl alcohol/benzyl benzoate-cleared tissue, and original 3D and 3D binary projections. Scale bars: 100 µm.

Tissue processing after 3D imaging

To determine whether subsequent 2D immunohistochemistry and molecular analysis were compatible with 3D immunofluorescence and BABB clearing, we rehydrated and paraffin-embedded tissue samples after clearing and imaging. Tissue morphology on HE staining before and after 3D processing was comparable. Conventional immunohistochemical staining for CK8-18, CD31, Ki67 and Vimentin (Fig. 4A) demonstrated that specific protein labelling after 3D imaging is still feasible. In the CD31, KI67 and Vimentin staining in fresh tissue, basal epithelial cell staining was observed, due to presence of CK5 antibody with a high antigen affinity, added for 3D fluorescent imaging, and shared primary antibody hosts (Suppl. Fig. 1C).

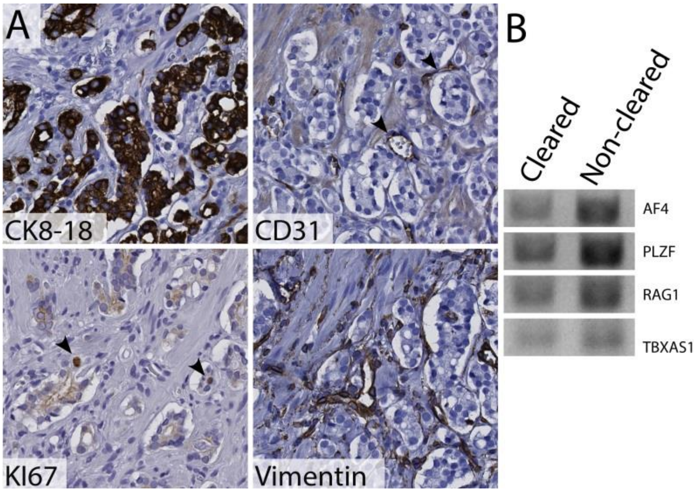

Figure 4. Processing of cleared formalin-fixed paraffin-embedded archival prostate cancer tissue. A) Immunohistochemical cytokeratin (CK) 8-18, CD31, Ki67 and Vimentin staining of cleared, re-embedded tissue sections demonstrates labelling of luminal epithelium, endothelium, proliferating cells, and stromal cells (arrowheads). B) Routine quality polymerase chain reaction on DNA isolated from cleared tissue samples shows the applicability of molecular analysis after 3D imaging, despite some degradation as compared with control non-cleared tissue.

After BABB clearing and 3D imaging, DNA could be isolated, amplified using PCR and analysed, however some degradation was observed (Fig. 4B and Suppl. Fig. 1D). DNA yield was sufficient for multiple DNA analysis (range 68.4 – 202.7 ng/µl) with minor loss of purity (range 0.7-1.1, Table 1). RNA isolation resulted overall in small amounts of degraded RNA (range 2.3 – 4.9 ng/l, purity range 1.3 – 6.8), which was non-sufficient for RNA analysis.

Table 1. DNA yield and purity of cleared and uncleared tissues.

	Yield in ng/µl (SD)	*Purity (SD)*
FFPE cleared (*n=6*)	68.4 (13.9)	0.7 (0.0)
FFPE uncleared (*n=2*)	145.8 (41.2)	1.0 (0.1)
Fresh cleared (*n=6*)	202.7 (96.2)	1.1 (0.2)
Fresh uncleared (*n=2*)	163.7 (2.9)	1.1 (0.0)

FFPE, formalin-fixed paraffin-embedded; SD, standard deviation

DISCUSSION

In this study, we have demonstrated that BABB mediated tissue clearing can successfully be applied for 3D imaging of fresh and FFPE clinical prostate specimens up to a depth of approximately 1000 µm. The feasibility of this methodology on FFPE tissues, particularly, offers the opportunity to study specific histopathologic areas of interest in their 3D context. We have also shown that, after 3D imaging, tissue samples are still suitable for routine 2D processing including immunohistochemistry and molecular analysis. The latter feature is of importance since 3D imaging has been raised as a novel diagnostic tissue processing methodology in the future.[56]

In this study, we were able to image small nuclear dyes and antibodies up to a depth of approximately 1000 µm, visualizing the 3D microscopic structure of both benign and malignant human prostate samples. We set out to develop 3D imaging in clinical prostate tissues to get more profound insight in prostate cancer growth patterns underlying the current Gleason grading system. A significant limitation of Gleason grading is its substantial inter-observer variability.[37-39, 43] This particularly accounts for distinguishing well-delineated Gleason grade 3 glands from ill-defined and fused Gleason grade 4 prostate cancer structures. Whereas Gleason score 6 prostate cancer patients are often eligible for active surveillance, patients with Gleason score 7 generally undergo active treatment, e.g. radical prostatectomy or radiotherapy.[57] This implies that inter-observer variability in distinguishing Gleason grade 3 and 4 patterns is of clinical relevance for individual patients. In active surveillance cohorts, for instance, 10% of patients would have had received different treatment recommendations based on pathologic re-evaluation of their biopsy samples.[39] Inter-observer agreement could be optimised by large-scale training sets or more detailed definition of distinguishing features. We hypothesise that providing comprehensive insight in 3D prostate growth pattern architectures will facilitate the interpretation of routine 2D diagnostic slides. While detailed characterisation of various growth patterns was not within the scope of this study, we were able to preliminarily interpret a subset of growth patterns i.e. we have shown that 1) Gleason grade 3 glands are branching and connecting, and 2) ill-defined Gleason grade 4 glands represent small tubules with more frequent interconnections. Instead of separate Gleason grades, both patterns seem to represent a continuum of tubular glands, showing differences in circumference and lumen volume. This could explain their considerable inter-observer variability. More extensive analysis of various growth patterns may further elucidate their 3D characteristics.

While 3D imaging is currently only used for research purposes, clearing techniques might offer an opportunity for diagnostic pathology in the future. Torres *et al*. demonstrated comparable morphology between BABB cleared of up to 1000 µm thick samples imaged by multi-photon microscopy with pseudo-colouring and reference HE 2D slides.[56] Advantages of such an approach would be that tissue samples remain intact and no material is lost due to tissue sectioning. We have showed that 2D immunohistochemistry and molecular analysis can still be performed on optically cleared tissue used for 3D imaging. With the current technological advancements in view, including light sheet microscopy, deep tissue scanning and optimisation of staining protocols, imaging of intact tissue samples might become an alternative to traditional 2D HE stained tissue slides in the future.

Current 3D imaging has few limitations. Passive antibody diffusion results in penetration for only up to 500 µm in one week, which hampers the depth of tissue imaging. Whereas diffusion of small fluorescent molecules is significantly faster, modifications in antibody staining methodology such as incubation under pressure might accelerate staining procedures. Secondly, interpretation of 3D, as well as routine 2D growth patterns is subjective and requires the development of algorithms to more objectively describe and separate tissue structures.

In conclusion, we have described a methodology for clearing and 3D imaging of fresh and FFPE prostate specimens up to a depth 1000 µm. This methodology allows 3D analysis of an unlimited range of normal and pathologic structures in clinical tissue specimens. The procedure is compatible with subsequent tissue sectioning, 2D (immuno)histochemistry and molecular analysis, which are prerequisite adjuncts in current diagnostic practice.

Supplementary Figures and Videos may be found in the online version of this article.

ACKNOWLEDGEMENTS

We thank Peggy and Carolina for performing the DNA isolation and PCR.

CHAPTER III

Three-dimensional architecture of common benign and pre-cancerous prostate epithelial lesions

Verhoef EI, van Cappellen WA, Slotman J, Kremers GJ, Ewing-Graham PC,
Houtsmuller AB, van Royen ME, van Leenders GJ.

Histopathology 2019 Jun;74(7):1036-1044

ABSTRACT

Aims: Many glandular lesions can mimic prostate cancer microscopically including atrophic glands, adenosis and prostate intraepithelial neoplasia. While the characteristic histopathological and immunohistochemical features of these lesions have been well established, little is known about their three-dimensional architecture. Our objective was to evaluate the three-dimensional organisation of common prostate epithelial lesions.

Methods and results: Five hundred micron thick punches (n=42) were taken from radical prostatectomy specimens, and stained with antibodies targeting Keratin 8-18 and Keratin 5 for identification of luminal and basal cells respectively. Tissue samples were optically cleared in benzyl alcohol: benzyl benzoate and imaged using a confocal laser scanning microscope. The three-dimensional architecture of peripheral and transition zone glands was acinar, composed of interconnecting and blind-ending saccular tubules. In simple atrophy, partial atrophy and post-atrophic hyperplasia, the acinar structure was attenuated with branching blind-ending tubules from parental tubular structures. Three-dimensional imaging revealed a novel variant of prostate atrophy characterised by large Golgi-like atrophic spaces parallel to the prostate surface, which were represented by thin, elongated tubular structures on HE slides. Adenosis on the other hand lacked acinar organisation, so that it closely mimicked low-grade prostate cancer. High-grade prostate intraepithelial neoplasia displayed prominent papillary intra-luminal protrusions but retained an acinar organisation, whereas intraductal carcinoma predominantly consisted of cribriform proliferations with either spheroid, ellipsoid or complex interconnecting lumens.

Conclusions: While various prostate epithelial lesions might mimic malignancy on HE slides, their three-dimensional architecture is acinar and clearly different from the tubular structure of prostate cancer, with adenosis as exception.

INTRODUCTION

The vast majority of prostate cancers are diagnosed on histopathological slides of transrectal or transperineal biopsies prompted by an elevated Prostate Specific Antigen (PSA) serum level or lower urinary tract symptoms. Prostate cancer diagnosis is usually straightforward and does not require supportive immunohistochemical staining in most cases. However, immunohistochemistry with Keratin 5, p63, alpha-methylacyl-CoA racemase (AMACR) and ETS-related gene (ERG) antibodies can be used for accurate diagnosis of small tumour foci and for distinction from benign glandular mimickers.[58-62]

Many glandular lesions can resemble prostate cancer.[63, 64] Glandular atrophy most frequently enters the differential diagnosis with conventional prostate cancer.[65] Atypical adenomatous hyperplasia, or adenosis, and high-grade prostate intraepithelial neoplasia are other common lesions with resemblance prostate cancer. While immunohistochemical stains can aid decision-making, the classification of a small number of lesions remains uncertain and these have been referred to as atypical small acinar proliferations.[66]

Histopathological evaluation is generally performed by microscopic analysis of 4-5 µm hematoxylin & eosin (HE) stained tissue slides. Our knowledge of histopathology and conventional diagnostic criteria is therefore entirely based on two-dimensional features. Little is known about the three-dimensional (3D) architecture of normal prostate glands, benign epithelial lesions and prostate cancer. Recent developments in the field of optical tissue clearing allow for sensitive deep fluorescent imaging of tissue specimens. While these techniques have mostly been used for studying *in vitro* and animal models, we have recently adapted the methodology for use on formalin-fixed, paraffin-embedded prostate tissues. This allows 3D imaging of specific regions of interest.[67] In this study we aimed to clarify the 3D architecture of the most common benign and pre-cancerous prostate glandular lesions.

MATERIALS AND METHODS

Case selection

A selection of archival formalin-fixed, paraffin-embedded radical prostatectomy specimens from patients who had undergone radical prostatectomy at the Erasmus Medical Centre in Rotterdam between 2012 and 2017 was made. These tissue specimens were fixed in neutral-buffered formalin and routinely processed for histopathologic evaluation. A urogenital pathologist (GvL) indicated regions of interest on 5 µm thick HE stained tissue slides. In total, 42 areas from 32 patients were used. These areas included glands from the normal peripheral (n=3) and transition zone (n=7), simple atrophy (n=6), cystic atrophy (n=5), post-atrophic hyperplasia (n=1), partial atrophy (n=2), adenosis (n=4), high-grade prostate intraepithelial neoplasia (n=9) and intraductal carcinoma (n=5), as well as one prostate cancer case for reference purposes. The use of tissue samples for scientific purposes was approved by the institutional Medical Research Ethics Committee (MEC-2011-295, MEC-2011-296). Samples were used in accordance with the “Code for Proper Secondary Use of Human Tissue in The Netherlands” as developed by the Dutch Federation of Medical Scientific Societies (FMWV, version 2002, update 2011).

Immunofluorescent staining and optical clearing

The total workflow is depicted in Fig. 1. Tissue punches from the regions of interest were taken from the corresponding paraffin blocks using a 500 µm diameter needle (Estigen, Tartu, Estonia)) resulting in 3-4 mm long cylindrical tissue cores with a diameter of 500 µm. Immunofluorescent staining was performed according to an adapted iDISCO protocol as described previously.[49, 67] In short, punches were dewaxed and this was followed by an auto-fluorescence blocking step. Thereafter the tissue punches were gradually rehydrated and incubated with Keratin 5 and Keratin 8/18 targeting antibodies (1:150; EP1601Y; Abcam, Cambridge, UK and 1:75; MS-743; Immunologic, Duiven, The Netherlands). These were visualised with secondary fluorescent Alexa 514- and Alexa 647-labelled antibodies (1:200; Life Technologies, Bleiswijk, The Netherlands). After dehydration in methanol, an optical clearing step was performed by immersing the tissue in benzyl-alcohol: benzyl benzoate until optical transparency was achieved. Samples were stored at 4°C in the dark until imaging.

Sample imaging

Confocal fluorescent imaging was done with an upright Leica SP5 confocal microscope fitted with a 1.95 mm working distance 20x NA1.0 APO water dipping objective (Leica Microsystems GmbH, Wetzlar, Germany). A 488 nm Argon and a

633 nm HeNe laser were used to record two-dimensional Z-stack images, resulting in 300-600 images per sample with a 0.72x0.72 µm pixel size and 1-3 µm step-size. Thereafter, Z-stacks were de-convoluted using a theoretical point-spread-function (PSF) in the Huygens Professional software (SVI, Hilversum, The Netherlands). Image processing and 3D rendering was performed with Fiji (ImageJ 1.49s) and Amira (version 5.5.0, ThermoFisher Scientific, Waltham, USA) software. For 3D renderings as depicted in this manuscript, Z-stacks were loaded in Amira after which we applied combined surface rendering and volume rendering with standard settings.[51] Total Z-stacks and 3D renderings were 739 µm by 739 µm in size with a 500 to 1000 µm depth.

Pathological evaluation and statistical analysis

Visual analysis and tubule measurement was done on Z-stacks as well as on corresponding rendered 3D reconstructions. Benign and pre-cancerous lesions could be identified by Keratin 8/18 positive luminal cells surrounded by Keratin 5 positive basal cells, whereas prostate cancer lacked the basal cell layer. The outer edges of the epithelial lesions were measured in 3 to 5 separate slides per image and 3 to 10 individual epithelial structures per slide, depending on the lesion. This resulted in 15-50 measurements per tissue sample. Glandular diameters were calculated as the average of all measurements for that lesion. Mean diameters were compared with a student's T-test using the Statistical Package for Social Sciences (SPSS, version 24, IBM, Chicago, USA).

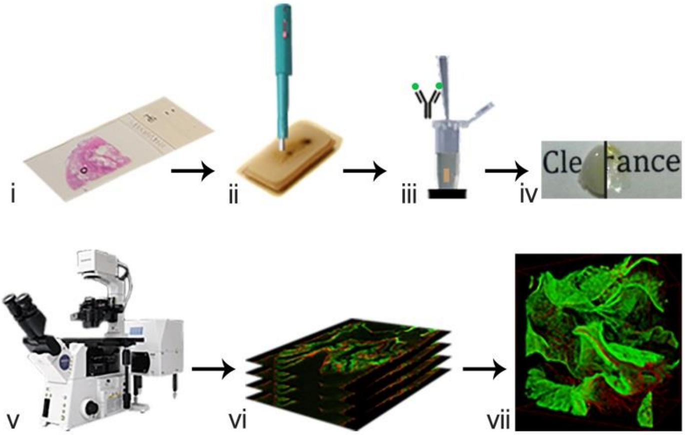

Figure 1. Workflow for 3D imaging of formalin-fixed, paraffin-embedded tissues. i) Tissue selection on HE slides, ii) tissue punching from corresponding blocks, in which the HE slide was directly adjacent to the top of the cylindrical biopsy punch, iii) incubation with fluorescently labelled antibodies, iv) optical tissue clearing, v) fluorescent confocal imaging, vi) stacking of confocal images and visual Z-stack analysis, vii) image processing and 3D rendering.

RESULTS

Peripheral and transition zone

On routine HE slides, peripheral zone glands consist of round, oval or slightly irregular glands with local small intraluminal protrusions with a fibrovascular core. Three-dimensional imaging revealed that peripheral zone glands had an acinar organisation, which was composed of interconnecting blind-ending saccular tubules with a mean diameter of 151 µm (standard deviation (SD) 55 µm, Fig. 2A,B). These tubules did not show a hierarchical pattern and a clear distinction between distal saccular structures and more central ducts was lacking (Suppl. Video 1). The scant intraluminal protrusions represented finger-like structures rather than longitudinal plicae. The 3D architecture of transition zone glands was similar to peripheral zone glands, with a mean tubular diameter of 165 µm (SD 75 µm). The most prominent difference was the abundance of intraluminal protrusions (Fig. 2C,D, Suppl. Video 2). Most acini were entirely surrounded by a compact sheet of Keratin 5 positive basal cells. However, regions of regularly spaced basal cells with slender interconnecting cytoplasmic sprouts were also identified, usually at tubule endings (Fig. 2D inset). The interconnecting saccular structures were more abundantly present in adenomatous hyperplastic nodules.

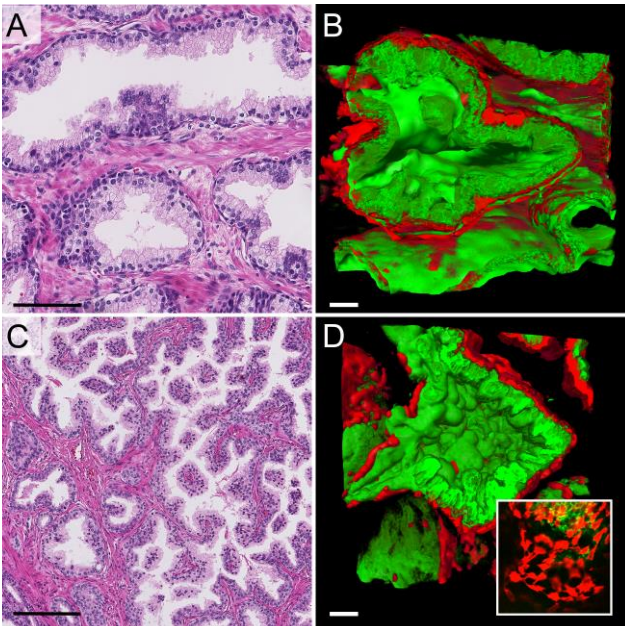

Figure 2. Peripheral zone A) HE slide and B) 3D rendering, showing large saccular tubules with interconnections, variable width and continuous layer of basal cells. Transition zone C) HE slide and D) 3D rendering with abundant presence of epithelial protrusions. Inset: 3D rendering of a tubule ending with scattered basal cells showing slender cytoplasmic interconnections. Original magnifications 10x (A, C) and 20x (B, D), green Keratin 8/18 and red Keratin 5 immunostaining in 3D renderings. Scalebars: 100 µm.

Atrophy

Four different variants of prostate glandular atrophy are recognised on HE slides: simple atrophy, simple atrophy with cyst formation, partial atrophy and post-atrophic hyperplasia.[68] The overall 3D glandular architecture of simple atrophy was tubular, emphasizing the prostatic acinar organisation of central tubules with branching and blind-ending tubules. The tubules had a mean diameter of 52 µm (SD 16 µm) and were surrounded by a continuous sheet of basal cells (Fig. 3A,B). In some cases connections were seen between atrophic tubules and larger glands with corpora amylacea (Suppl. Video 3). Cystic atrophy consisted of dilated glands with a mean diameter of 202 µm (SD 118 µm), significantly larger than the acini of the peripheral or transition zone ($P<.001$). Here, the overall acinar organisation was retained with presence of dilated saccular or tubular outpouchings from the cyst (Fig. 3C,D, Suppl. Video 4). In some cases, large corpora amylacea could be seen in the cystic tubules. Post-atrophic hyperplasia had a similar acinar organisation in which the difference between central and branching blind-ending tubules could be more clearly appreciated (Fig. 4A,B, Suppl. Video 5). Partially atrophic tubules displayed an acinar organisation, with basal cells typically lacking around a significant part of the lesion (Fig. 4C,D; Suppl. Video 6). Although four atrophic patterns have been defined previously on HE slides, 3D reconstruction clearly revealed an additional pattern. This pattern consisted of parallel large slit-like ellipsoid spaces with few interconnections resulting in a Golgi-like organisation (Fig. 4E,F; Suppl. Video 7). On HE slides this atrophic variant appeared as longitudinally sectioned tubules at the dorsolateral sides of the prostate.

Adenosis

On HE slides, adenosis can closely mimic Gleason score 6 prostate cancer, with closely packed round glands lined with slightly atypical luminal epithelial cells, often with intraluminal secretions and crystalloids. Three-dimensional renderings showed that adenosis was composed of small to medium sized tubules with a mean diameter of 71 µm (SD 33 µm). These tubules were smaller than transition zone gland tubules ($P<.001$) and discontinuously covered with basal cell clusters. The tubules were branching to such extent that no obvious acinar organisation could be appreciated (Fig. 5A,B, Suppl. Video 8). For comparison we have included a sample of Gleason score 6 prostate adenocarcinoma consisting of tubules with rare interconnections. These formed a disorganised network composed of luminal cells only and had no basal cell layer (Fig. 5C,D). For a complete and comprehensive description of the 3D architecture of prostate adenocarcinoma growth patterns, we refer to our previous study.[69]

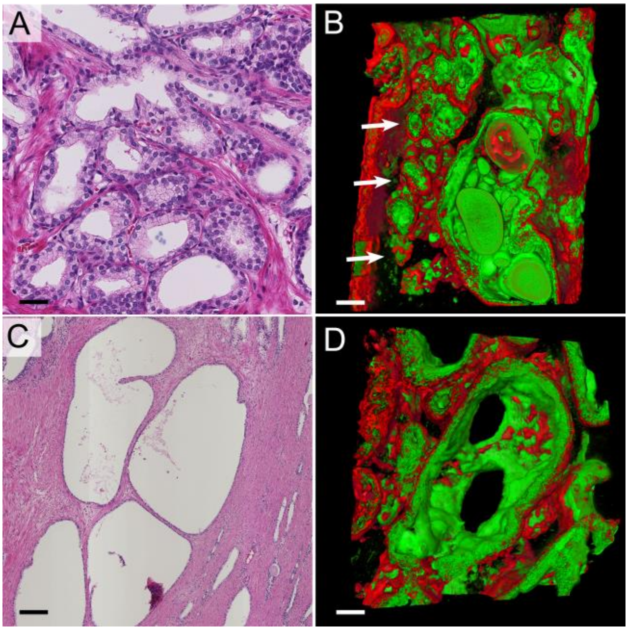

Figure 3. Simple atrophy **A**) HE slide and B) 3D rendering with acini of short saccular tubules (arrows) interconnecting with a dilated gland filled with corpora amylacea. Cystic atrophy C) HE slide and D) 3D rendering with large dilated glands in connection with adjacent glands, represented by dark oval openings. Original magnifications 20x, green Keratin 8/18 and red Keratin 5 immunostaining in 3D renderings. Scalebars:100 µm.

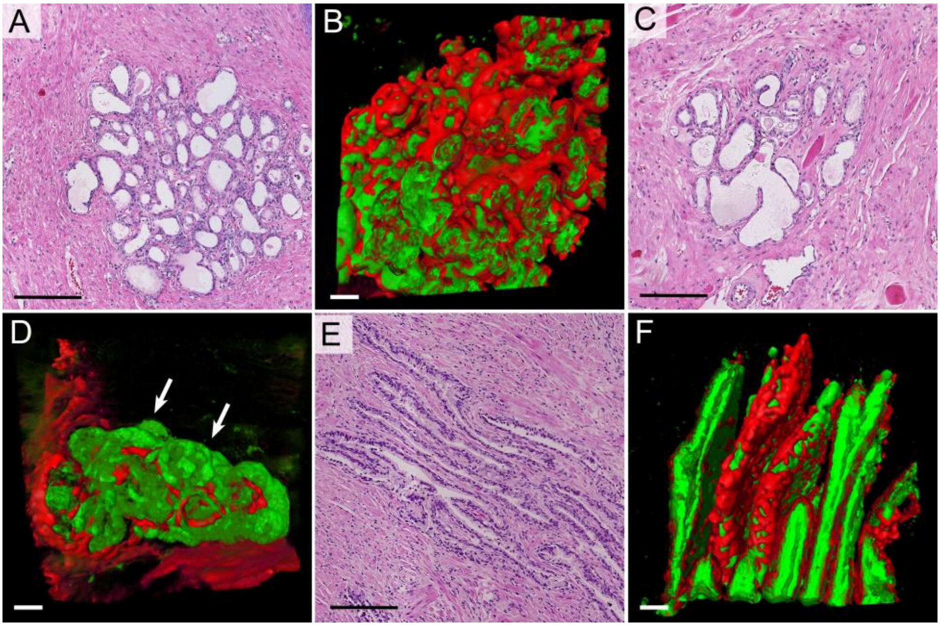

Figure 4. Post-atrophic hyperplasia A) HE slide and B) 3D rendering with an acinus of short saccular tubules. Partial atrophy C) HE slide and D) 3D rendering with an irregular acinus of short tubules with large areas lacking a basal cell layer (arrows). Golgi-like atrophy D) HE slide and F) 3D rendering, showing parallel longitudinal ellipsoid slit-like structures in an arrangement that resembles the Golgi apparatus. Original magnifications 10x (A,C,E) or 20x (B,D,F), green Keratin 8/18 and red Keratin 5 immunostaining in 3D renderings. Scalebars: 100 µm.

High-grade prostate intraepithelial neoplasia

On 3D imaging, high-grade prostate intraepithelial neoplasia retained an acinar organisation with short-tubular and saccular outpouchings of 171 µm (SD 76 µm). The diameter of these structures was not statistically different from peripheral or transition zone glands (P=.072). Most acini were lined with a compact sheet of basal cells, however there were only scattered basal cells present in some regions. Papillary intraluminal finger-like protrusions lined with luminal cells were abundant (Fig. 6A,B). High-grade prostate intraepithelial neoplasia was connecting to adjacent pre-existent glands in 3D reconstructions (Suppl. Video 9).

Intraductal carcinoma

Intraductal carcinoma of the prostate predominantly consists of malignant cribriform or solid epithelial proliferations spanning the entire lumen of dilated pre-existent glands on HE slides. Three-dimensional rendering revealed an intact distended acinar architecture of pre-existent glands with a mean diameter of 153 µm (SD 92 µm), filled with a solid or cribriform mass of luminal epithelial cells. In cribriform lesions, lumens were either small spheroid, ellipsoid or complex interconnecting spaces with rounded or sharp endings (Fig. 6C,D, Suppl. Video 10). While intraductal carcinoma is generally larger than high-grade prostate intraepithelial neoplasia, we selected relatively small lesions for 3D visualisation because of confocal field view limitations. The most prominent difference with high-grade prostate intraepithelial neoplasia was the presence of lumen-spanning epithelial proliferations.

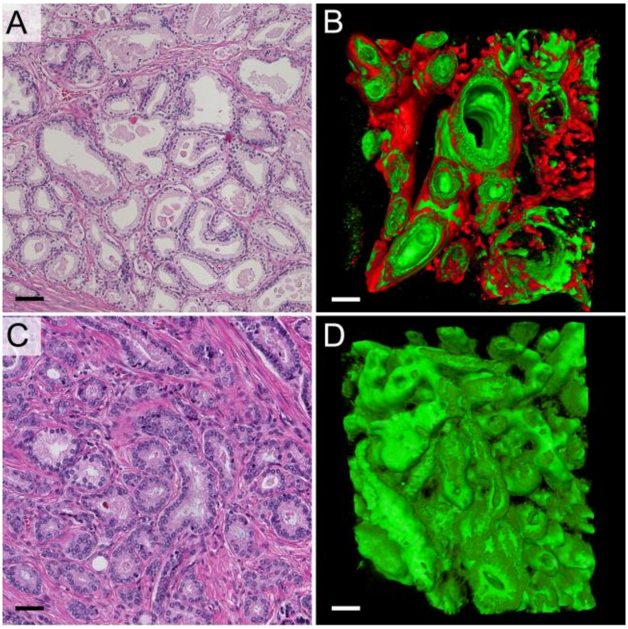

Figure 5. Adenosis A) HE slide and B) 3D rendering with tubular architecture, lacking a clear branching acinar structure. Gleason grade 3 prostate cancer C) HE slide and D) 3D rendering displaying a network of interconnecting tubules. Original magnifications 20x, green Keratin 8/18 and red Keratin 5 immunostaining in 3D renderings. Scalebars:100 µm.

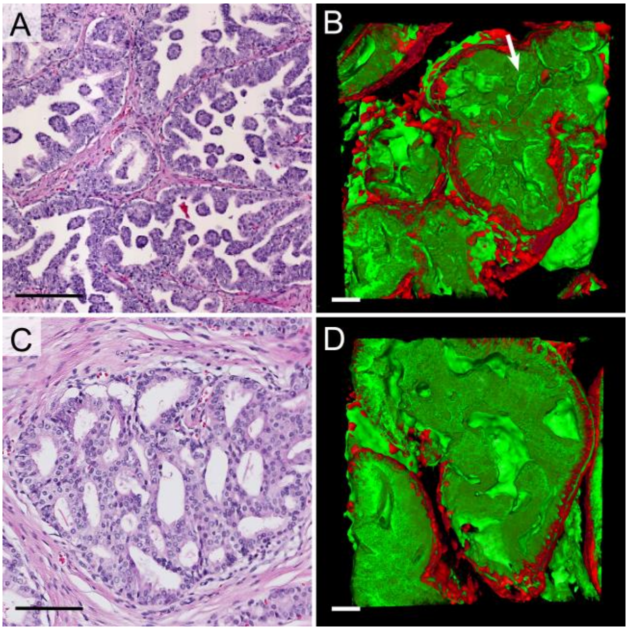

Figure 6. High-grade PIN A) HE slide and B) 3D rendering with saccular architecture and abundant papillary protrusions (arrow). Intraductal carcinoma of the prostate C) HE slide and D) 3D rendering with gland spanning liminal epithelial proliferation with irregular interconnecting luminal spaces. Original magnifications 10x (A,C) or 20x (B,D), green Keratin 8/18 and red Keratin 5 immunostaining in 3D renderings. Scalebars: 100 µm.

DISCUSSION

In this study we provided a comprehensive overview of the 3D architecture of common benign prostate epithelial lesions which might mimic prostate cancer on HE slides. We demonstrated that peripheral and transition zone glands have an acinar organisation, with interconnecting saccular blind-ended tubules without clear hierarchical arrangement. This basic acinar organisation was retained in adenomatous hyperplasia and high-grade prostate intraepithelial neoplasia and was emphasised in atrophy. We were able to identify a novel atrophic variant by 3D microscopy, consisting of large flat ellipsoid spaces with a Golgi-like appearance parallel to the prostate dorsolateral capsule. This atrophic variant showed longitudinally sectioned glands on HE slides, which were located in the peripheral zone of the prostate. Interestingly, adenosis was the only variant showing a tubular instead of an acinar organisation, closely mimicking Gleason score 6 prostate cancer.

The differential diagnoses of prostate cancer, including atrophy, adenosis and prostate intraepithelial neoplasia, have been described extensively in various studies.[70-72] Although their histopathological and immunohistochemical features are well known, little is known about the underlying 3D architecture of these benign mimickers.[73, 74] Benign and malignant prostate lesions can show overlapping morphological features on HE slides. However, we found that the 3D architecture of most benign epithelial lesions was entirely different.[67, 69] For instance, simple and partial atrophy might closely resemble on HE and immune-stained slides, showing partial loss of basal cells.[65] However, their 3D structure showed that these lesions clearly retain an acinar organisation, which is disrupted in prostate cancer.[67]

Simple atrophy, partial atrophy and post-atrophic hyperplasia most clearly revealed the basic acinar organisation of the prostate, showing branching of a central tubule into small blind-ended tubules. Peripheral and transition zone glands were organised in an acinar fashion as well, however this was less obvious owing to the larger size of these glands and to the presence of papillary protrusions. Atrophic tubules were sometimes connected to slightly distended glands with numerous corpora amylacea, suggesting glandular obstruction as cause of cystic atrophy. Importantly, we found the presence of large slit-like atrophic glands with a Golgi-like 3D organisation, which to our knowledge has not been reported before. We hypothesise that these structures are the result of compression of pre-existent glands, for instance by benign hyperplastic nodules. However, the dynamic pathophysiology of these benign glandular lesions remains to be elucidated.

Adenosis was the only lesion in this study that showed a 3D architecture with non-hierarchical interconnecting tubules, reminiscent of Gleason score 6. While most other prostatic lesions could be discriminated from prostate cancer by their 3D organisation, presence of basal cells was the only distinguishing feature in adenosis.

The similarity between the 3D growth of adenosis and prostate cancer Gleason grade 3 raises the question of whether adenosis and prostate cancer are related. Despite detection of rare molecular aberrations in adenosis, it is different from prostate cancer at the molecular level, for instance there is complete absence of *TMPRSS2:ERG* fusions in adenosis.[75-78] Although adenosis is not a malignant proliferation, it may share aberrant activation of molecular pathways involved in 3D glandular expansion with low-grade prostate cancer.

A strong point of the current study was the use of intact tissue samples from archival prostate specimens. This facilitated selection of specific regions-of-interest for 3D renderings. Imaging of small intact tissue samples prevents alignment artefacts that could occur when using many consecutively cut and stacked slides. However, use of fluorescently labelled antibodies to distinguish between luminal and basal epithelial cells restricts the potential sample volume to be visualised owing to limited antibody penetration, especially in compact glandular structures. Therefore, 3D imaging of larger areas was not feasible using the current protocol which is a disadvantage as compared to other 3D imaging techniques such as registration of serial sections.[31] In addition, image analysis is time consuming, and this meant that we were able to evaluate only a limited number of tissue samples, not covering the entire range of benign prostate epithelial lesions.

In conclusion, long-distance confocal microscopy and optical tissue clearing can be used to comprehensively visualise the unique 3D architecture of benign prostate epithelial lesions. While various lesions might mimic malignancy on routine tissue slides, we found that their 3D architecture is mostly entirely different from prostate cancer. Finally, 3D imaging can be helpful in elucidating the pathophysiology of benign prostate glandular lesions.

Supplementary Videos may be found in the online version of this article.

CHAPTER IV

Three-dimensional analysis reveals two major architectural subgroups of prostate cancer growth patterns

Verhoef EI, van Cappellen WA, Slotman J, Kremers GJ, Ewing-Graham PC,
Houtsmuller AB, van Royen ME, van Leenders GJ.

Modern Pathology 2019 Jul;32(7):1032-1041

ABSTRACT

Aims: The Gleason score is one of the most important parameters for therapeutic decision-making in prostate cancer patients. Gleason growth patterns are defined by their histological features on 4-5 µm cross-sections and little is known about their three-dimensional architecture. Our objective was to characterise the three-dimensional architecture of prostate cancer growth patterns.

Methods and results: Intact tissue punches (n=46) of representative Gleason growth patterns from radical prostatectomy specimens were fluorescently stained with antibodies targeting Keratin 8/18 and Keratin 5 for detection of luminal and basal epithelial cells, respectively. Punches were optically cleared in benzyl alcohol: benzyl benzoate and imaged using a confocal laser scanning microscope up to a depth of 500 µm.*:* Gleason pattern 3, poorly formed pattern 4 and cords pattern 5 all formed a continuum of interconnecting tubules where the diameter of the structures and the lumen size decreased with higher grade. In fused pattern 4 the interconnections between the tubules were markedly closer together. In these patterns all tumour cells were in direct contact with the surrounding stroma. In contrast, cribriform Gleason pattern 4 and solid pattern 5 demonstrated a three-dimensional continuum of contiguous tumour cells, where the vast majority of cells had no contact with the surrounding stroma. Transitions between cribriform pattern 4 and solid pattern 5 were seen. There was a decrease in the number and size of inter-cellular lumens from cribriform to solid growth pattern. Glomeruloid pattern 4 formed an intermediate structure consisting of a tubular network with intra-luminal epithelial protrusions close to tubule splitting points.

Conclusions: In conclusion, three-dimensional microscopy revealed two major architectural subgroups of prostate cancer growth patterns: 1) a tubular interconnecting network including Gleason pattern 3, poorly formed and fused Gleason pattern 4 and cords Gleason pattern 5, and 2) serpentine contiguous epithelial proliferations including cribriform Gleason pattern 4 and solid Gleason pattern 5.

INTRODUCTION

The Gleason score is one of the most important parameters for therapeutic decision making in men with prostate cancer and is entirely based on tumour growth patterns.[36, 79] Tumour heterogeneity is recognised by adding the two most common Gleason patterns in radical prostatectomy specimens. Gleason patterns 1, 2 and 3 prostate cancers are composed of well-delineated malignant glands, and distinction of these patterns is putatively of no clinical significance.[80] Gleason pattern 4 tumours consist of poorly formed, fused, cribriform or glomeruloid structures. Tumour growth in cords, single cells or solid fields, or the presence of comedonecrosis, characterises Gleason pattern 5. Whereas men with Gleason score 6 (ISUP group 1) prostate cancer are often eligible for surveillance, active treatment is usually offered to patients with Gleason score ≥ 7 (ISUP group ≥ 2).[57]

Although individual growth patterns within Gleason pattern 4 and 5 are not routinely mentioned in pathology reports, numerous studies have demonstrated poorer outcome when cribriform growth is present.[9, 81-84] Cribriform growth in radical prostatectomies and diagnostic biopsies has been associated with more post-operative biochemical recurrence and disease-specific death in ISUP group ≥ 2 prostate cancer patients.[83] On the other hand, ISUP group 2 patients with glomeruloid architecture may have better outcome than those without this pattern.[9] Consideration of individual growth patterns may therefore have added value for therapeutic stratification of ISUP group 2 prostate cancer patients.

A major limitation of the Gleason grading system is the substantial inter-observer variability.[85-87] Amongst others, Egevad *et al*. found that among 337 European pathologists only 56% agreement was achieved between expert consensus and participants' score.[88] Inter-observer variability in Gleason grading occurs predominantly in assessment of poorly formed and fused growth patterns.[9, 37, 81, 83, 87] In particular small glands with sporadic lumen formation may be interpreted as tangentially sectioned Gleason pattern 3, poorly formed pattern 4 or cords pattern 5. Inter-observer variability significantly affects clinical decision-making since distinction of ISUP group 1 prostate cancer from higher grades is an important threshold for active surveillance and treatment.[57]

Diagnostic criteria for histopathological grading of prostate cancer are entirely based on tumour features on routine 4-5 µm tissue sections. Very little is known about the underlying three-dimensional (3D) architecture of Gleason growth patterns. Serial sectioning and scanning of many tissue sections has given some insight into 3D tumour architecture, however, this is costly, time-consuming and susceptible to artefacts. In contrast, optical tissue clearing allows for sensitive fluorescent imaging of whole tissue specimens without physical sectioning.[21, 27, 52, 89]

We have already demonstrated the feasibility of this technique for 3D visualisation of formalin-fixed, paraffin-embedded prostate tissues up to a depth of 800 µm.[67] The objective of the current study was to characterise and provide a comprehensive overview of the 3D architecture of prostate cancer growth patterns.

MATERIALS AND METHODS

Case selection

Archival formalin-fixed paraffin-embedded radical prostatectomy specimens from patients who had undergone radical prostatectomy for prostate cancer at the Erasmus Medical Centre between 2012 and 2017 were included. Specimens were fixed in neutral-buffered formalin, transversely cut in 4 mm slices and entirely embedded for histopathologic evaluation. The mean age at operation was 66 years (SD 6.8 years). Regions of interest for 3D imaging were indicated on hematoxylin & eosin (HE) stained slides by a urogenital pathologist. In total, 46 tumour areas from 35 patients were selected for analysis, including Gleason pattern 3 (n=8), poorly formed (n=6), fused (n=6), glomeruloid (n=10) and cribriform (n=6) Gleason pattern 4, and cords (n=7) and solid fields (n=3) Gleason pattern 5. Three normal peripheral zone areas were included to serve as a reference. The use of tissue samples for scientific purposes was approved by the institutional Medical Research Ethics Committee (MEC-2011-295, MEC-2011-296) and was in accordance with the “Code for Proper Secondary Use of Human Tissue in The Netherlands” as developed by the Dutch Federation of Medical Scientific Societies (FMWV, version 2002, update 2011).

Immunofluorescent staining and optical clearing

Tissue punches from the areas with the selected growth patterns were taken from the corresponding paraffin blocks using a 500 µm diameter needle (Estigen Tissue Scuebcem, Tartu, Estonia) resulting in 3-4 mm long cylindrical tissue cores with a diameter of 500 µm. Immunofluorescent staining and optical clearing was carried out according to an adapted iDISCO protocol as described previously (Suppl. table 1).[49, 67] Briefly, punches were dewaxed after which auto-fluorescence was blocked overnight. Subsequently, punches were gradually rehydrated and incubated with primary Keratin 5 and Keratin 8/18 antibodies (1:150; EP1601Y; Abcam, Cambridge, UK and 1:75; MS-743; Immunologic, Duiven, The Netherlands) and secondary fluorescent Alexa-514 and Alexa-647 labelled antibodies (1:200; Life Technologies, Bleiswijk, The Netherlands). In order to visualise subtle connective tissue cores within fused Gleason pattern 4, these samples were additionally stained with Fibronectin (FN1; 1:50; ab2413, Abcam, Cambridge, United Kingdom) and secondary Alexa-647 antibodies. Tissue was again dehydrated in methanol and subsequently optically cleared in benzyl alcohol: benzyl benzoate. Samples were then stored at 4°C in the dark until imaging.

Sample imaging

Fluorescently stained punches were imaged with an upright Leica SP5 confocal microscope equipped with a 1.95 mm working distance 20x NA1.0 APO water dipping objective (Leica Microsystems GmbH, Wetzlar, Germany). Two-dimensional Z-stack images were recorded using a 488 nm Argon and a 633 nm HeNe laser with a 0.72x0.72 µm pixel size and 1-3 µm step-size, resulting in 300-600 images per sample. Huygens Professional software (SVI, Hilversum, The Netherlands) with a theoretical point-spread-function (PSF) was used for de-convolution of the Z-stacks, whereas 3D rendering and image measurements were performed with Fiji (ImageJ 1.49s) and Amira (version 5.5.0, ThermoFisher Scientific, Waltham, USA) software.[51] Z-stacks were loaded in Amira, after which we applied combined surface and volume rendering with standard settings. The total size of the Z-stacks and 3D renderings was 739 by 739 µm with a depth of 500 µm. Reference HE slides were positioned at a vertical side of the 3D renderings, but are not directly continuous with the depicted areas in each case, depending on the site of imaging in the 3-4 mm long cylindrical core.

Pathological evaluation and statistical analysis

Both consecutive Z-stacks and 3D rendered images were investigated. Pre-existent benign prostate glandular structures were identified by Keratin 8/18 positive luminal cells surrounded by Keratin 5 positive basal cells. Prostate cancer structures were recognised by architecturally disorganised Keratin 8/18 positive epithelial structures without a basal cell layer. Tubular blind-ending tips were identified by detailed analysis of both Z-stacks and 3D renderings, and could be well distinguished from transversely sectioned tubules at the border of the tissue samples. In each of the tissue specimens, the outer edges of the epithelial structures were measured in 3 to 5 consecutive 2D slides per image and 3 to 10 individual epithelial structures per slide, depending on the growth pattern. This resulted in 12-50 measurements per tissue sample. Statistics were performed with a student's T-test using the Statistical Package for Social Sciences (SPSS, version 24, IBM, Chicago, USA). Original magnifications of HEs and 3D renderings 20x, with green Keratin 8/18 and red Keratin 5 staining in 3D renderings.

RESULTS

Benign epithelial glands

Benign peripheral zone glands had an acinar organisation composed of interconnecting saccules with variable intraluminal papillary protrusions. Benign glands were composed of an inner Keratin 8/18 positive luminal cell layer and an outer flat Keratin 5 positive layer of basal cells (Fig. 1A,B; Suppl. Video 1). In all cases malignant epithelial structures could easily be distinguished from pre-existent benign glands by their architectural organisation and lack of basal cells (Fig. 1C,D).

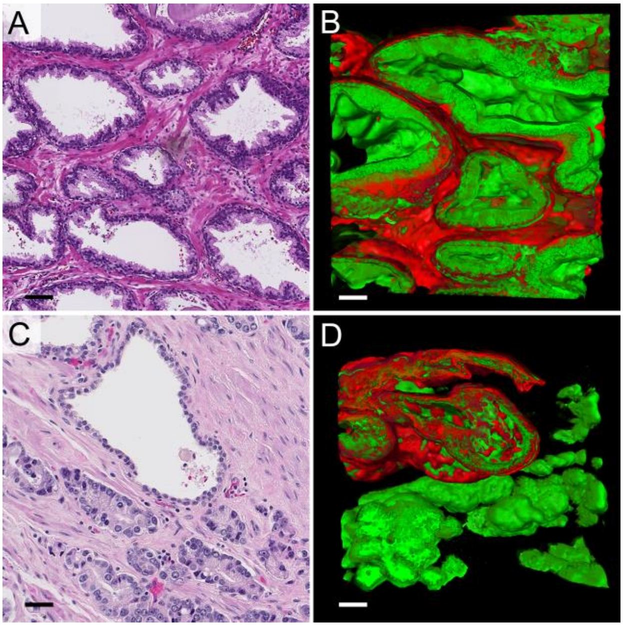

Figure 1. Peripheral zone A) HE slide and B) 3D rendering, showing interconnecting saccules of variable width containing intraluminal papillary protrusions and surrounded by a continuous Keratin 5 positive basal cell layer (red). C) HE slide and D) 3D rendering of pre-existent benign glands surrounded by basal cells (upper left) and irregular malignant epithelial structures without basal cell layer (lower). Original magnifications 20x, green Keratin 8/18 and red Keratin 5 immunostaining in 3D renderings. Scalebars: 100 µm.

Gleason pattern 3

Gleason pattern 3 prostate cancer was composed of round to slightly oval, well-delineated curving tubules with a mean diameter of 45 µm (SD 12 µm) with regular interconnections (Fig. 2A,B; Suppl. Video 2). All malignant epithelial cells had contact with surrounding stroma. We did not find any specific tubular orientation along the cranial-caudal, transverse or sagittal axis of the prostate. Blind-ending tubules were present sporadically and showed no specific location within the tubular network.

Gleason pattern 4

Poorly formed glands

Poorly formed Gleason pattern 4 glands were represented by small round tubules with a significantly smaller average diameter than Gleason pattern 3 tubules (24 µm, SD 7 µm; P<.001). Poorly formed glands showed more frequent interconnections and blind-endings than Gleason pattern 3 tubules (Fig. 2C,D). Regularly, we observed transitions between poorly formed Gleason pattern 4 glands and Gleason pattern 3 tubules (Fig. 2E; Suppl. Video 3).

Fused glands

Fused Gleason pattern 4 glands consisted of round to oval tubules with a diameter of 68 µm (SD 18 µm), slightly larger than Gleason pattern 3 tubules (P<.001). The hallmark of the fused pattern was the presence of abundant interconnections between the tubules, which occurred markedly closer together than in the aforementioned patterns (Fig. 3A,B). On HE slides fused Gleason pattern 4 can closely resemble cribriform architecture.[87, 88] Here 3D microscopy however revealed subtle intervening fibrovascular tissue in between and around all malignant tubules, revealing that all malignant cells had contact with surrounding stroma (Suppl. Video 4).

Cribriform fields

Cribriform Gleason pattern 4 was characterised by fields of contiguous epithelial tumour cells with a mean diameter of 151 µm (SD 68 µm). The vast majority of tumour cells did not have any contact with the surrounding stroma, in contrast with the patterns described previously. Three-dimensionally, this pattern showed a variable number of spherical, ellipsoid, slit-like or irregular interconnecting inter-cellular lumens (Fig. 3C,D). Adjacent cribriform fields with intervening stroma on HE slides represented continuously curving irregular serpentine structures on 3D renderings (Suppl. Video 5). We did not observe any transition between cribriform fields and aforementioned tubular structures in our cohort.

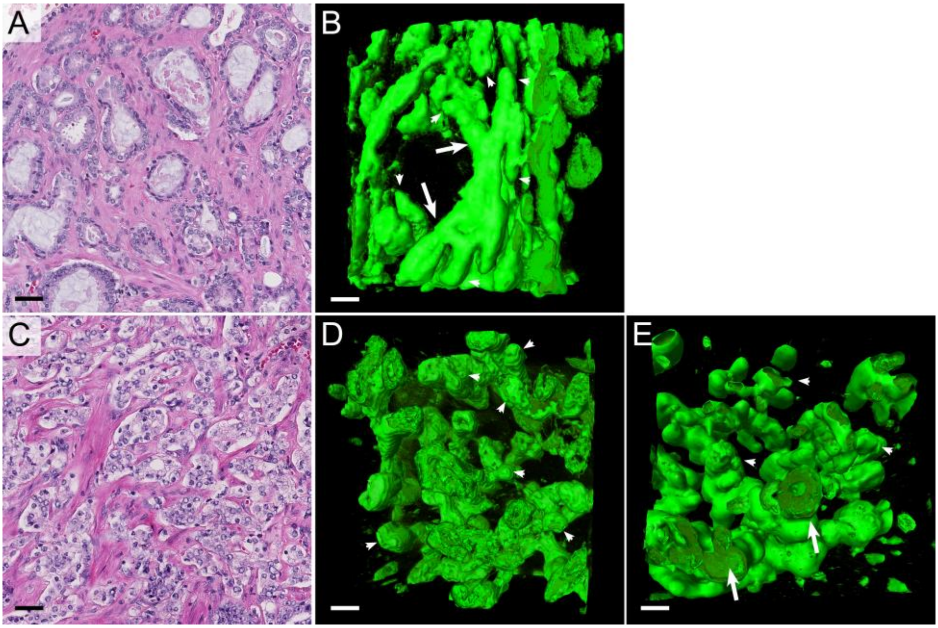

Figure 2. Gleason pattern 3 A) HE slide and B) 3D rendering showing a tubular network with interconnections (arrows) and blind-endings (arrowheads). Poorly formed Gleason pattern 4 C) HE slide and D) 3D rendering of small-sized interconnecting tubules with blind-endings (arrowheads). E) Well-delineated Gleason pattern 3 tubules (arrows) were directly connected to and continuous with poorly formed Gleason pattern 4 structures (arrowheads). Original magnifications 20x, green Keratin 8/18 and red Keratin 5 immunostaining in 3D renderings. Scalebars: 100 µm.

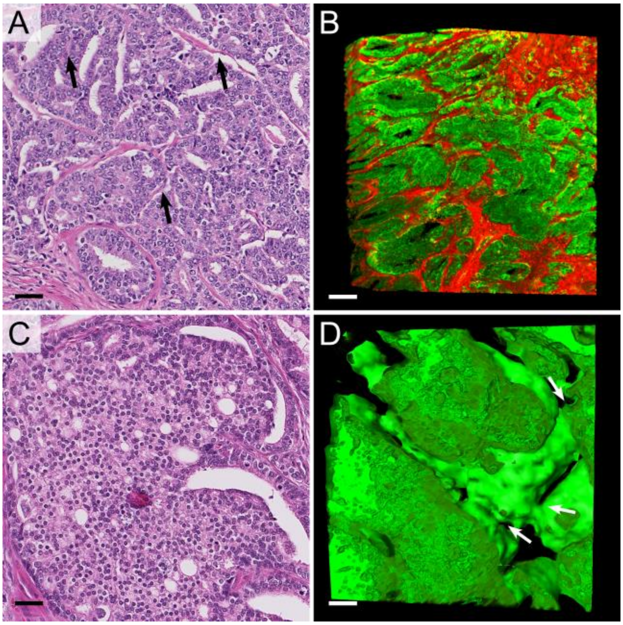

Figure 3. Fused Gleason pattern 4 A) HE slide with subtle fibrovascular cores (arrows) and B) 3D reconstruction revealing frequently interconnecting tubules. Cribriform Gleason pattern 4 C) HE slide and D) 3D rendering of cribriform fields displaying contiguous epithelial cells with spherical and ellipsoid inter-cellular lumens. The majority of tumour cells do not contact with the surrounding stroma. The cribriform areas formed serpentine structures with variably sized interconnections (arrows). Original magnifications 20x, green Keratin 8/18 and red Fibronectin (B) immunostaining in 3D renderings. Scalebars: 100 µm.

Glomeruloid glands

In two-dimensional cross-sections glomeruloid Gleason pattern 4 structures resemble renal glomeruli and are characterised by dilated glands with round protrusions of malignant epithelial cells (Fig. 4A,B). On 3D renderings, these glomeruloid structures were present within an interconnecting network of tubules, which had a mean diameter of 65 µm (SD 19 µm) reminiscent of Gleason pattern 3 glands but with larger tubule diameters (P<.001). Two different glomeruloid structures could be distinguished using 3D microscopy. The first type were nodular epithelial glomeruloid proliferations which connected to the tumour cells lining the tubule on one side, but did not make contact with the tubular lining on the opposite side or the surrounding stroma. These protrusions often occurred at tubular branching points (Suppl. Video 6). The second type showed presence of subtle fibrovascular cores on the HE slides, representing clusters of markedly curved tubules in three-dimensions. All the tumour cells within this glomeruloid variant made contact with the surrounding stroma. When glomeruloid structures are larger, distinction between glomeruloid and cribriform growth pattern on HE slides can be challenging (Fig. 4C).[87] These larger cribriform-like structures grew similar to the first type of glomeruloid pattern in 3D renderings. We did not observe continuity between glomeruloid structures and the cribriform pattern.

Gleason pattern 5

Cords and single cells

On HE slides, Gleason pattern 5 cords consist of one or two-layered cords of cells without distinctive lumens (Fig. 5A). In 3D, cords and single cell structures formed a continuous meshwork consisting of one or two cell-layers with extensive branching and interconnections. The average diameter of these cords was 15 µm (SD 7 µm; Fig. 5B), significantly smaller than poorly formed Gleason pattern 4 (P<.001). Small inter-cellular lumens were observed at deeper levels of the cord pattern in the Z-stack, indicating repetitive subtle transitions from Gleason pattern 4 poorly formed tubules to Gleason pattern 5 cords (Suppl. Video 7).

Solid fields

Solid fields Gleason pattern 5 are represented on hematoxylin & eosin slides as round or irregularly formed areas composed of tumour cells without intercellular lumens. Most cells do not make contact with the surrounding stroma (Fig. 5C). 3D reconstruction revealed that the solid fields represented round to ellipsoid irregular serpentine structures with an average diameter of 185 µm (SD 78 µm), interconnecting and varying in width (Fig. 5D; Suppl. Video 8). While intercellular lumens were inconspicuous on hematoxylin & eosin slides, the Z-stacks often showed small round and ellipsoid lumens reminiscent of cribriform Gleason pattern

4 at deeper levels, indicating transition between these patterns. In this cohort, we did not find transition between solid fields Gleason pattern 5 and tubular growth patterns.

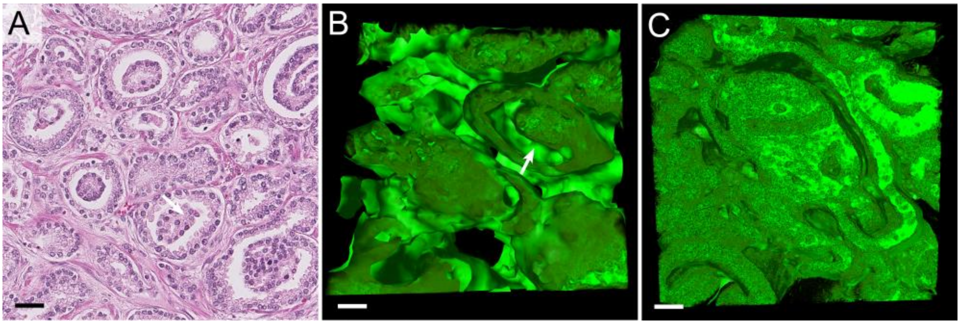

Figure 4. Glomeruloid Gleason pattern 4 A) HE slide and B) 3D rendering of small glomeruloid protrusions, consisting of malignant epithelial cells in contact with the epithelial tubular lining at one side of the tubule (arrow). C) Large glomeruloid protrusion with intercellular lumens. While this structure resembles cribriform architecture, the glomeruloid protrusion only makes contact with one side of the tubule. Original magnifications 20x, green Keratin 8/18 and red Keratin 5 (no basal cells present) immunostaining in 3D renderings. Scalebars: 100 µm.

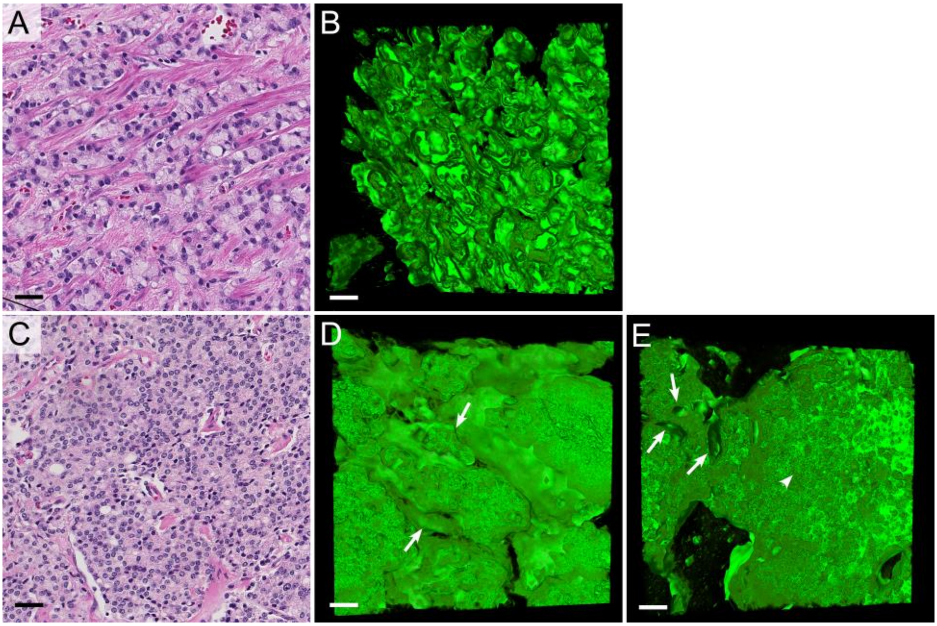

Figure 5. Gleason pattern 5 cords A) HE slide and B) 3D rendering with interconnecting cords consisting of one or two tumour cells without lumens. Solid Gleason pattern 5 C) HE slide and D) 3D rendering showing solid structures with variably sized interconnections (arrows). E) Transition from cribriform Gleason pattern 4 (left side) with multiple lumens (arrows) to solid Gleason pattern 5 (right side) lacking lumen formation (arrowhead). Original magnifications 20x, green Keratin 8/18 and red Keratin 5 (no basal cells present) immunostaining in 3D renderings. Scalebars: 100 µm.

DISCUSSION

In the current study we provided a comprehensive overview of the three-dimensional architecture of prostate cancer growth patterns and revealed two architecturally different growth pattern subgroups. The first subgroup consisted of a tubular network where the vast majority of the tumour cells made direct contact with the surrounding stroma. We demonstrated that Gleason pattern 3 glands formed a network of regularly interconnecting tubules. In poorly formed Gleason pattern 4 the network consisted of smaller sized tubules, and in fused Gleason pattern 4 the tubules showed frequent and closely spaced interconnections. In glomeruloid Gleason pattern 4 intra-luminal epithelial protrusions occurred within the tubular network, close to tubular branching points. Cords Gleason pattern 5 represented a network structure with frequent interconnections without lumens. The second subgroup was characterised by contiguous tumour cell proliferations where the vast majority of tumour cells did not make contact with the surrounding stroma, consisting of cribriform Gleason pattern 4 and solid pattern 5. This subgroup represented irregular serpentine structures of contiguous tumour cells with a decrease in frequency and size of intercellular lumens from cribriform to solid pattern.

An important advantage of 3D imaging is the visualisation of morphological transitions and continuity of growth patterns which can generally not be appreciated in routine 2D sections. Until now only a few studies have aimed to reconstruct prostate cancer growth patterns in three-dimensions, using sectioning and alignment of numerous sequential slides.[27, 29-31, 44, 90] For instance, Boag *et al*. used this method on 5 different cases to generate 3D renderings, showing interconnections between Gleason pattern 3 and pattern 4 glands.[30] Similarly, Tolkach *et al*. demonstrated continuity between Gleason pattern 3 and pattern 4 after serial sectioning and 3D rendering of one ISUP group 2 case.[31] Apart from being laborious, stacking of sequentially cut slides is prone to tissue malformation and registration artefacts. In contrast, fluorescent staining, tissue clearing and long-distance confocal scanning microscopy is performed on intact tissue samples without tissue sectioning, thus preventing alignment artefacts. It is also less laborious, although specialised microscopic equipment is required.[67] Our finding of three-dimensional continuity between Gleason patterns 3 and 4 is in line with the aforementioned studies, even though different methods were applied.

The most important observation of this study was that we identified two architecturally different growth pattern subgroups. Firstly, there are interconnecting tubular structures, consisting of Gleason pattern 3, poorly formed and fused Gleason pattern 4 and cords Gleason pattern 5. These patterns have variable tubule diameters, interconnection frequencies and lumen formations, but the vast majority of the tumour cells make direct contact with the surrounding stroma. In our cohort we observed frequent transitions between these growth patterns. While poorly formed glands had smaller sized tubules than Gleason pattern 3, no clear cut-off could be made between these patterns with respect to tubule diameter, number of interconnections or luminal size. Similarly, 3D spatial transitions between poorly formed Gleason pattern 4 and Gleason pattern 5 cords made strict delineation of these patterns impossible. The increased number of interconnections in fused Gleason pattern 4 was only arbitrarily distinguished from branching Gleason pattern 3 tubules. The three-dimensional continuity of these patterns is reflected by the substantial inter-observer variability in daily pathology practice. Distinguishing on the one hand tangentially sectioned Gleason pattern 3 glands from poorly formed and fused Gleason pattern 4 glands, and on the other hand poorly formed Gleason pattern 4 glands from Gleason pattern 5 cords on hematoxylin & eosin slides are the principal areas of difficulty.[37, 43, 87, 91] Secondly, there are serpentine compact irregular epithelial proliferations, consisting of cribriform Gleason pattern 4 and solid Gleason pattern 5, with decreasing inter-epithelial lumen sizes and frequencies. Both patterns have in common that the vast majority of tumour cells are contiguous and do not make contact with the surrounding stroma. Although we did not include comedonecrosis in this study, routine diagnostic slides reveal that comedonecrosis predominantly occurs in a background of cribriform and solid structures. We found transitions between cribriform Gleason pattern 4 and solid Gleason pattern 5 but did not observe transitions between these patterns and the aforementioned tubular growth pattern subgroup.

The inter-observer agreement of cribriform Gleason pattern 4 is excellent. The only variability there is occurs in the distinction with complex fused and large glomeruloid patterns.[87] Of interest, our 3D images showed that although complex fused Gleason pattern 4 glands might resemble cribriform Gleason grade 4 structures on hematoxylin & eosin slides, scattered subtle intra-lesion fibrovascular cores were present in complex fused Gleason pattern 4 glands as a distinguishing feature. On hematoxylin & eosin slides, glomeruloid growth morphologically represents an intermediate pattern between tubular and cribriform growth. While some glomeruloid structures with subtle fibrovascular cores actually closely resembled fused Gleason pattern 4 glands in 3D, most glomeruloid structures did not contain intra-lesional connective tissue. Based on morphological resemblance and frequent coexistence, Lotan and Epstein hypothesised that glomeruloid pattern is a precursor of cribriform growth.[92] However, Choy *et al*. found that ISUP group 2 and 3 prostate cancer patients with glomeruloid pattern had significantly lower biochemical recurrence rates than those with cribriform growth.[81] Our 3D reconstructions did not reveal continuity between glomeruloid and cribriform structures. Therefore, the clinical relevance of the glomeruloid pattern and its place as putative precursor of cribriform growth remains to be established.

Various studies have shown that prostate cancer patients with a ISUP group 2 tumour showing cribriform Gleason pattern 4 have a worse outcome than patients without this pattern. Kweldam *et al*. found that patients with a ISUP group 2 tumour without cribriform growth on biopsy had similar metastasis-free survival and biochemical recurrence rates as patients with ISUP group 1 prostate cancer.[9, 83] The adverse outcome related to cribriform growth was also present in men with ISUP group > 2 prostate cancer.[9, 93] A putative explanation for the worse outcome of patients with cribriform growth pattern is the fact that cribriform architecture is associated with genomic instability, while non-cribriform Gleason patterns 4 are genomically indistinguishable from Gleason pattern 3.[94-96] These clinical and molecular observations are in line with the two architectural subgroup hypothesis as raised in the current study. To the best of our knowledge there are as yet no studies on the clinical relevance of Gleason 5 growth patterns. Investigation into the prognostic value of these individual Gleason grade 5 patterns is essential for future tumour grading and understanding. Based on our current findings, we hypothesise that solid Gleason pattern 5 is likely to be associated with worse outcome than cords or single cells Gleason pattern 5.

This study represents the first comprehensive three-dimensional characterisation of relevant prostate cancer growth patterns. Optical clearing of intact samples allows visualisation and investigation of tumour growth patterns without the need for sectioning and alignment of numerous consecutive tissue slides. We studied the most common prostate cancer growth patterns, but did not include the full spectrum of growth patterns and variants that can be encountered in daily practice.[97, 98] While we selected unambiguous cases of the Gleason growth patterns, inter-observer variability might still exist, for instance in labelling as either poorly formed or fused Gleason pattern 4.[87, 88] Another disadvantage of 3D pathology is the descriptive terminology that is used for reporting. Three-dimensional imaging of prostate cancer, however, allows for objective geometrical modelling in a 3D matrix. Finally, while we identified two 3D growth pattern subgroups with glomeruloid architecture as an intermediate structure, the differences between these subgroups on the clinical and molecular level remain to be investigated.

In conclusion, this study gives a comprehensive overview of the 3D architecture of prostate cancer growth patterns. We show the existence of two major architectural growth patterns subgroups: 1) a tubular interconnecting network of tumour cells in direct contact with adjacent stroma, with a variable gland and lumen size, including Gleason pattern 3, poorly formed and fused Gleason pattern 4 and cords Gleason pattern 5, and 2) serpentine contiguous epithelial proliferations where the majority of tumour cells do not make contact with adjacent stroma and with variable inter-epithelial lumen frequency, including cribriform Gleason pattern 4 and solid Gleason pattern 5. Insight into tumour growth patterns facilitates comprehension of prostate cancer behaviour and biology beyond current Gleason grading.

Supplementary Tables and Videos may be found in the online version of this article.

CHAPTER V

Concordance of cribriform architecture in matched prostate cancer biopsy and radical prostatectomy specimens

Hollemans E*, Verhoef EI*, Bangma CH, Rietbergen J, Roobol MJ, Helleman J, van Leenders GJ.

Histopathology, 2019 Sep;75(3):338-345

*These authors contributed equally to this paper

ABSTRACT

Aims: Invasive cribriform and/or intraductal carcinoma have been identified as independent adverse parameters for prostate cancer outcome. Little is known on biopsy undersampling of cribriform architecture. Our aim was to determine the extent of cribriform architecture undersampling and to find predictive factors for identifying false cribriform negative cases.

Methods and results: We reviewed 186 matched prostate biopsies and radical prostatectomy specimens. Of 97 biopsy Grade Group 2 (Gleason score 3+4=7) patients, 22 (23%) had true cribriform negative (TN), 39 (40%) false negative (FN) and 36 (37%) true positive (TP) biopsies. Patients with FN biopsies had higher albeit not statistically significant (P=.06) median PSA levels than patients with TP biopsies (12 *versus* 8 ng/ml). A PI-RADS 5 lesion was present in 9/16 (54%) FN and 3/11 (27%) TN biopsies (P=.05). Positive biopsy rate (P=.47), percentage Gleason pattern 4 (P=.55) and glomeruloid architecture (P=1.0) were not different. Logistic regression identified PSA as independent predictor (Odds Ratio 3.5; 95% Confidence Interval 1.2-9.4, P=.02) for cribriform architecture on radical prostatectomy but PI-RADS score not. The FN rate for large cribriform architecture at radical prostatectomy was 27%, which was lower than for any cribriform architecture (P=.01). During follow-up (median 27 months), biochemical recurrence-free survival of patients with TP biopsies was significantly shorter than of those with FN biopsies (P=.03).

Conclusions: In conclusion, 40% of Grade Group 2 prostate cancer biopsies were FN for cribriform architecture. These patients had higher PSA levels and more frequent PI-RADS score 5 lesions than men with TN biopsies.

INTRODUCTION

Risk stratification and therapeutic decision-making in prostate cancer patients is affected by potential biopsy undersampling. The Gleason score is one of the most important parameters for predicting disease outcome and guiding individual treatment. Men with Gleason score 3+3=6 (International Society of Urological Pathology (ISUP) Grade Group 1) prostate cancer are eligible for active surveillance, whereas men with Gleason score ≥ 4+3=7 (Grade Group 3-5) are usually treated with radical prostatectomy, radiation therapy and/or hormonal therapy. The optimal therapeutic strategy for men with Gleason score 3+4=7 (Grade Group 2) still is a matter of debate. While most of these patients will undergo active treatment, surveillance is increasingly being considered in this subgroup. Incorporation of additional clinicopathological and molecular parameters might be able to support optimal decision-making in this large prostate cancer subpopulation.

Grade Group 2 prostate cancer is a heterogeneous disease with variable architectural growth patterns and Gleason pattern 4 quantities. While individual growth patterns are not routinely mentioned in pathology reports, recent studies have shown that patients with cribriform architecture have adverse outcome as compared to those without.[9, 99, 100] Both invasive and intraductal cribriform architecture have been associated with adverse clinicopathological characteristics, post-operative recurrence rates, metastasis and disease-specific death.[82, 84, 101-103] On the other hand, biopsy Grade Group 2 prostate cancer patients without cribriform architecture have comparable disease-specific survival and post-operative biochemical recurrence rates as men with Grade Group 1 disease.[9, 83] Quantification of Gleason pattern 4 can further add in risk stratification since post-operative biochemical recurrence rates increment with higher Gleason pattern 4 tumour percentage.[104] Cribriform architecture and Gleason pattern 4 quantification might therefore be important adjuncts in risk stratification of Grade Group 2 prostate cancer patients.

While pathological tumour characteristics are important for clinical decision-making, prostate biopsies are prone to undersampling. Prostate cancer is up-graded in up to 40% of subsequent radical prostatectomy specimens.[8, 105] At present, little is known on the extent of undersampling in detection of cribriform architecture or Gleason pattern 4 percentage. The aim of our study is to determine the extent of undersampling for the detection of cribriform architecture in matched prostate biopsy and radical prostatectomy specimens, and to identify potential factors for discriminating true from false cribriform negative prostate biopsies.

MATERIALS AND METHODS

Patient selection

We identified 186 patients who had undergone both biopsy and subsequent radical prostatectomy at Erasmus MC University Medical Centre, Rotterdam, The Netherlands between 2010 and 2017. Biopsies were prompted by elevated Prostate Specific Antigen (PSA) levels or obtained in the scope of active surveillance. The Prostate Imaging Reporting and Data System (PI-RADS) score was annotated by an expert uroradiologist, when patients had received multiparametric magnetic resonance imaging (MRI).[106] When suspicious lesions (PI-RADS 3 to 5) were visible on MRI, targeted MRI-ultrasound fusion biopsies were taken. Individual biopsy cores were enclosed in separate containers and radical prostatectomy specimens were completely embedded for diagnostic purposes. All slides of both biopsies and radical prostatectomies were available for pathologic review. This study was approved by the institutional Medical Research Ethics Committee (MEC-2018-1614).

Pathologic evaluation

All biopsies were reviewed by three investigators, who were blinded to clinical outcome and radical prostatectomy characteristics. For each biopsy core the following features were recorded: Gleason score, Grade Groups according to the WHO/ISUP 2014 guidelines, maximal single biopsy tumour length (mm), overall estimated percentage Gleason pattern 4 and individual tumour growth patterns.[36] Invasive cribriform Gleason pattern 4 was not distinguished from intraductal carcinoma because of their significant morphological overlap, which would require extensive immunohistochemical stainings for further discrimination.[9] In case targeted biopsies were obtained, these were considered as separate biopsies and not as one single biopsy. Matching radical prostatectomy specimens were evaluated as described previously.[101] We recorded Gleason score, Grade Group, pT-stage according to the AJCC TNM 8th edition, surgical margin status, percentage Gleason pattern 4 and individual growth patterns.[107] Furthermore, we distinguished small and large expansive cribriform growth pattern based on a cut-off of two times the size of adjacent pre-existent normal glands.[101]

Clinical follow-up

After radical prostatectomy, clinical follow-up consisted of bi-annual, and later annual monitoring of serum PSA levels. Biochemical recurrence was defined as PSA levels ≥ 0.2 ng/ml measured at two consecutive points in time, at least three months apart with undetectable PSA levels after operation, or as PSA increase of > 2.0 ng/ml when serum PSA had not declined to zero after operation. Survival was defined as time in months from radical prostatectomy to biochemical recurrence or last follow-up.

Statistical analysis

Continuous variables with normal distribution were compared by Student’s t-test and One-way ANOVA analysis, those without normal distribution with the Mann-Whitney U test. For categorical parameters Chi-square or Fishers exact were used. Correlation between continuous variables was analysed using Pearson’s correlation coefficient. Dichotomous outcome variables were analysed using logistic regression. Survival was visualised by Kaplan-Meier curves. Statistics were performed using R version 3.2.2 (R, Vienna, Austria) and results were considered significant when the two-sided P-value was <.05.

RESULTS

Clinicopathological characteristics

The entire cohort consisted of 186 patients with matched biopsy and radical prostatectomy specimens. The mean age at time of operation was 65 years (interquartile range (IQR) 62-70) and the mean PSA level was 12 ng/ml (IQR 6-15). In total 144 (77%) patients underwent systematic biopsies, 26 (14%) received systematic and targeted biopsies, and 16 (9%) had targeted biopsies only. The mean number of biopsies taken was 9 (IQR 8-10) with 4 (IQR 3-5) biopsies containing adenocarcinoma, representing 49% (IQR 30-66) of the total number of biopsy cores. Fifty (27%) patients had overall biopsy Grade Group 1, 99 (53%) Grade Group 2, 11 (6%) Grade Group 3, 15 (8%) Grade Group 4 and 11 (6%) Grade Group 5.

On radical prostatectomy, 87 (47%) adenocarcinomas were pT2, 76 (41%) pT3a and 23 (12%) pT3b. Distribution of the Grade Groups on radical prostatectomy was as follows: 19 (10%) Grade Group 1, 108 (58%) Grade Group 2, 25 (14%) Grade Group 3, 17 (9%) Grade Group 4 and 17 (9%) Grade Group 5. Tumour up-grading occurred in 65 (35%) and down-grading in 14 (8%) radical prostatectomies, while 107 (57%) cases had concordant tumour grades. Positive surgical margins were present in 63 (34%) patients. Eighty patients had simultaneously undergone pelvic lymph node dissection, of which 18 (23%) contained lymph node metastasis. The mean post-operative follow-up was 32 months (median 22, IQR 8-51).

Invasive cribriform and/or intraductal carcinoma was observed in 57 (31%) diagnostic biopsies and in 128 (69%) radical prostatectomy specimens (Table 1). Cribriform architecture was present in both matched biopsy and radical prostatectomy specimens in 55 (30%), and absent in 56 (30%) cases. In 73 (39%) men cribriform architecture was observed in the radical prostatectomy specimen, but not in preceding biopsies. Two cases (1%) had cribriform architecture at biopsy but not at subsequent radical prostatectomy, which is probably due to sampling error and these were excluded from further analyses. Therefore, the sensitivity for cribriform architecture on biopsies was 43%, while specificity was 97%. Cribriform architecture was observed more frequently in targeted (19/40; 48%) than systematic biopsies (36/144; 25%, P=.01).

Table 1. Prevalence of invasive cribriform and/or intraductal carcinoma (CR/IDC) in biopsies and matched radical prostatectomies.

	Radical prostatectomy	
Prostate biopsy	CR/IDC-	CR/IDC+
CR/IDC-	56 (30%)	73 (39%)
CR/IDC+	2 (1%)	55 (30%)

Concordance of cribriform architecture in Grade Group 2 prostate cancer biopsies

Since cribriform architecture might be most relevant for treatment decisions in patients with biopsy Grade Group 2 prostate cancer, we performed further analyses within this subgroup (n=97). Thirty six (37%) patients with biopsy Grade Group 2 demonstrated cribriform architecture on both matched biopsy and radical prostatectomy specimen (true cribriform positive, CR+/CR+), while cribriform architecture was absent in both specimens in 22 (23%) cases (true cribriform negative, CR-/CR-). In 39 (40%) patients cribriform architecture was present on radical prostatectomy but not on preceding biopsy; these patients were considered as having false cribriform negative (CR-/CR+) biopsies. None of the patients with biopsy Grade Group 2 had cribriform architecture on biopsy while radical prostatectomy was negative for cribriform architecture.

Identification of predictors in true and false cribriform negative Grade Group 2 prostate cancer biopsies

Patients with true negative biopsies were slightly younger (62 *versus* 65 years, P=.06) and had lower PSA levels (8 ng/ml *versus* 12 ng/ml, P=.06) than men with false negative biopsies, however these differences were not significant (Table 2). In total, 51 patients (53%) had undergone multiparametric MRI prior to biopsy. Out of 11 patients with true negative biopsies, 3 (27%) had a PI-RADS 5 lesion as compared to 9/16 (56%) of false negative and 17/24 (71%) of true positive biopsy patients (P=.05). The number of biopsies (P=.53), percentage of positive biopsies (P=.47) and maximal tumour length (P=.44) were not different between true and false negative biopsies. Since Gleason pattern 4 percentage and glomeruloid architecture have both been associated with cribriform architecture, we assessed the predictive value of these pathologic parameters[84, 92] Mean percentage of Gleason pattern 4 was 12% (IQR 5-10%) in true negative biopsies and 11% (IQR 5-16%) in false negative biopsies (P=.55). There was only a weak correlation between percentage Gleason pattern 4 on biopsies (mean 13%, IQR 5-20%) and matched radical prostatectomies (mean 31%, IQR 10-40%, R^2=0.093; P=.001). Glomeruloid growth pattern was encountered in 6/22 (27%) true negative and 11/39 (28%) false negative biopsies (P=1.0).

Logistic regression analysis on cribriform negative biopsy patients showed that age (odds ratio (OR) 1.1, 95% confidence interval (CI) 1.0-1.3, P=.02) and PSA (OR 3.3, 95% CI 1.2-9.1, P=.02) were independent predictive parameters for presence of cribriform architecture on radical prostatectomy in multivariable analysis, whereas PI-RADS score, number and percentage of positive biopsies, maximal tumour length, presence of targeted biopsies and percentage Gleason grade 4 were not (Table 3).

Table 2. Characteristics of biopsy Grade Group 2 prostate cancer (PCa) patients stratified for true cribriform negative (CR-/CR-), false cribriform negative (CR-/CR+) and true cribriform positive (CR+/CR+) biopsies.

	CR-/CR- (n=22)	CR-/CR+ (n=39)	CR+/CR+ (n=36)	P-value
Age	62 (63, 58-65)	65 (66, 62-71)	66 (66, 62-71)	.06[a]
PSA	8 (8, 6-10)	12 (10, 6-17)	16 (13, 9-19)	.06[b]
PI-RADS score				.10[c]
No MRI	11 (50%)	23 (59%)	12 (33%)	
1-2	3 (14%)	0 (0%)	0 (0%)	
3	1 (5%)	1 (3%)	2 (6%)	
4	4 (18%)	6 (15%)	5 (14%)	
5	3 (14%)	9 (23%)	17 (47%)	
Number of biopsies	9 (9, 8-10)	8 (8, 7-10)	10 (10, 8-12)	.53[d]
Number PCa positive biopsies	4 (3, 2-6)	4 (4, 3-5)	6 (5, 4-8)	.64[d]
Percentage PCa positive biopsies	47 (38, 25-71)	52 (50, 31-73)	59 (61, 40-76)	.47[d]
Maximal tumour length (mm)	7 (7, 5-8)	8 (7, 5-10)	9 (10, 7-12)	.44[d]
Percentage Gleason pattern 4	12 (8, 5-10)	11 (8, 5-16)	17 (15, 7-23)	.55[a]
Presence of glomeruloid growth	6 (27%)	11 (28%)	12 (33%)	1.0[e]
Presence of large cribriform growth	0	6 (15%)	16 (44%)	N/A
Presence of targeted biopsies	2 (9%)	8 (20%)	13 (36%)	.30[e]
ISUP grade on radical prostatectomy				.01[e]
1	2 (9%)	1 (3%)	1 (3%)	
2	18 (82%)	29 (74%)	26 (72%)	
3	0 (0%)	8 (20%)	7 (19%)	
4	0 (0%)	1 (3%)	1 (3%)	
5	2 (9%)	0 (0%)	1 (3%)	
Positive surgical margins	8 (36%)	12 (31%)	12 (33%)	.78[c]
pT stage (TNM 8th)				.66[c]
2	11 (50%)	15 (38%)	17 (47%)	
3a	10 (45%)	20 (51%)	12 (33%)	
3b	1 (5%)	4 (11%)	7 (20%)	
Biochemical recurrence	2 (9%)	6 (15%)	13 (36%)	.69[e]
Metastasis	0 (0%)	1 (3%)	4 (11%)	N/A

Mean (median, IQR) or n (%). [a] Wilcox-test, [b] t-test (log2 values were used for this test), [c] Chi-square (χ^2), [d] One-Way Anova, [e] Fisher test. P-values resemble comparison between CR-/CR- and CR-/CR+.

Comparison of false negative and true cribriform positive Grade Group 2 biopsies

PSA levels of men with true positive biopsies were slightly higher than of those with false negative biopsies, but this was not statistically significant (16 ng/ml *versus* 12 ng/ml, P=.13). Patients with true positive biopsies had a significantly higher total number of biopsies (10 *versus* 8, P=.02) and number of tumour positive biopsies (6 *versus* 4, P=.001), however no differences were seen in percentage positive biopsies (59% *versus* 52%, P=.19) when compared to patients with false negative biopsies. Percentage Gleason pattern 4 was higher in patients with cribriform positive biopsies than in those with false negative biopsies (17% *versus* 11%, P=.03). Final Grade Group (P=.97), pT stage (P=.27) and surgical margin status (P=.24) of the radical prostatectomy specimens were not different between these two groups. The tumour volume percentage of cribriform growth at radical prostatectomy was higher in patients with true positive biopsies than in those with false negative biopsies, but this did not meet conventional measures of significance (13% *versus* 6%, P=.06).

Large expansile cribriform architecture, which represents an aggressive subtype of invasive cribriform carcinoma, was present in 22/97 (23%) radical prostatectomy specimens.[101] Sixteen of these 22 (73%) patients had any size cribriform fields on biopsy, while biopsies were false negative in 6 (27%) men. The false negative rate for more aggressive large cribriform architecture (6/22; 27%) was lower than for any cribriform architecture (39/75; 52%, P=.01). In case large cribriform carcinoma was present at radical prostatectomy, the tumour volume percentage of any cribriform growth at the operation specimens did not differ between men with false cribriform negative and true positive biopsies (P=.5). This indicates that the lower false negative rate of large cribriform growth was not merely due to larger total cribriform tumour percentage at radical prostatectomy.

Clinicopathological outcome in Grade Group 2 patients

Of 97 patients with biopsy Grade Group 2 prostate cancer, 73 (75%) had concordant Grade Group at radical prostatectomy, 20 (21%) were up-graded to Grade Group 3 to 5, and 4 (4%) down-graded to Grade Group 1. Up-grading occurred in 9/36 (25%) true positive and in 9/39 (23%) false negative biopsies, and was significantly lower (P=.01) in true negative biopsies (2/22, 9%). Extra-prostatic expansion and surgical margins status were not significantly different between the three groups.

Biochemical recurrence occurred in 21 (22%) patients and was significantly more frequent in the true positive (13/36, 36%) than in the false negative group (6/39, 15%, P=.03). The true negative group (2/22, 9%) showed the lowest incidence of biochemical recurrence, however this difference was not significant (P=.13) when compared to the false negative group.

Table 3. Logistic regression analysis of biopsy Grade Group 2 cribriform negative prostate cancer (PCa) patients (n=61), predicting cribriform architecture on radical prostatectomy.

	Univariate			Multivariable		
	OR	95% CI	P-value	OR	95% CI	P-value
Age	1.1	1.0-1.2	.06	1.1	1.0-1.3	.02
PSA (log2)	2.2	1.0-4.8	.04	3.3	1.2-9.1	.02
PI-RADS score						
<5	*ref*					
5	1.9	0.5-7.9	.38	1.8	0.3-9.1	.49
Number of biopsies	0.9	0.8-1.1	.53	0.8	0.6-1.1	.21
Percentage PCa positive	2.1	0.3-15	.47	0.2	0.0-5.5	.35
Maximal tumour length (mm)	1.1	0.9-1.2	.43	1.0	0.9-1.3	.70
Percentage Gleason pattern 4	1.0	0.9-1.0	.70	1.0	0.9-1.0	.36
Presence of targeted biopsies						
No	*ref*					
Yes	2.6	0.5-13	.26	1.1	0.1-10	.91

[a] Per doubling unit. OR = odds ratio, CI = confidence interval.

The median post-operative follow-up of Grade Group 2 patients was 27 months (mean 18, IQR 6-40). Patients experienced biochemical recurrence after a median of 14 months (mean 24, IQR 5-32). Biochemical recurrence-free survival was not significantly different between patients with true negative and false negative biopsies (log rank P=.55). Patients with cribriform positive biopsies had significantly shorter biochemical recurrence-free survival than men with false negative biopsies (log rank P=.03, Fig. 1).

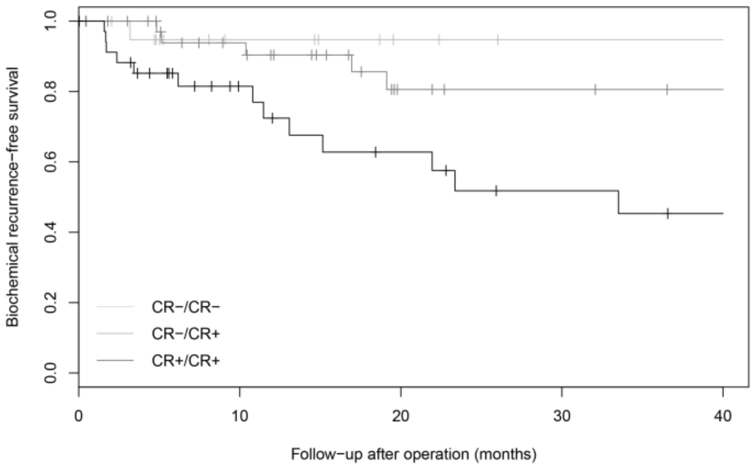

Figure 1. Biochemical recurrence-free survival of biopsy Grade Group 2 prostate cancer patients, stratified for the presence of cribriform architecture on biopsies and subsequent radical prostatectomies (log rank over all groups, P-value = .03).

DISCUSSION

Identification and pathologic reporting of invasive cribriform and/or intraductal carcinoma of the prostate are increasingly important since they are both associated with adverse clinical outcome.[9, 82, 100, 103] Biopsy undersampling is a well-known problem which might have significant impact on individual patient management.[105, 108, 109] Hitherto, little is known about biopsy undersampling in identifying cribriform architecture. In this study we demonstrated that biopsies were false negative for cribriform architecture in 39% of all cases and in 40% of patients with biopsy Grade Group 2 prostate cancer. In false negative Grade Group 2 patients, age and PSA level were independent predictive parameters for presence of cribriform architecture on subsequent radical prostatectomy, while percentage of positive biopsies, maximal biopsy tumour length, percentage Gleason pattern 4 and glomeruloid growth were not. Patients with the more aggressive large cribriform growth pattern on radical prostatectomy were, however, less likely to have cribriform negative biopsies.[101] Biopsy Grade Group 2 patients with false cribriform negative biopsies showed better biochemical recurrence-free survival rates than men with true cribriform positive biopsies albeit follow-up was relatively short.

Masoomian *et al*. studied concordance rates of cribriform architecture in 245 matched biopsies and operation specimens, and found a relatively low sensitivity of 47%, corresponding well with the 43% sensitivity in our study.[110] In their subset of Grade Group 2 biopsy patients, false negative and true positive biopsies both had more advanced stage as compared to true negative biopsies on radical prostatectomy suggesting men with false negative and true positive biopsies have comparable outcome. This contrasts with our study as we found that post-operative biochemical recurrence-free survival of men with true positive biopsies was significantly shorter than of those with false negative biopsies. The difference might be explained by the different and relatively small cohorts of both studies.

While most patients with biopsy Grade Group 2 prostate cancer undergo active treatment, the question is rising whether surveillance could be a safe alternative for subgroups of this large patient population. It has for instance been proposed that patients with biopsy Grade Group 2 prostate cancer and low Gleason pattern 4 percentage should be considered for surveillance.[111, 112] Others have suggested that biopsy Grade Group 2 prostate cancer patients without invasive cribriform and/or intraductal carcinoma might be eligible for surveillance.[83, 102] To further support clinical decision tools, it is important to get insight in the false negative rate of potentially aggressive disease parameters and to determine how this rate can be minimised to an acceptable level. In the current study, we showed that consideration of PSA level, which is an important parameter for active surveillance, might prevent men with potentially aggressive false negative biopsies from being abstained from immediate treatment. Furthermore, presence of a PI-RADS 5 lesion on multiparametric MRI might also be indicative of more aggressive disease. Truong *et al*. identified cribriform morphology in combined systematic and targeted biopsies in 37% of PI-RADS 5, 24% of PI-RADS 4 and 6% of PI-RADS 2 lesions, suggesting that high-grade MRI lesions are related to more aggressive tumours with cribriform morphology.[113] Prendeville *et al*. identified cribriform morphology in 8% of PI-RADS 3/4 lesions and in 39% of PI-RADS 5 lesions, indicating that PI-RADS score might be a predictor for cribriform positive prostate cancer.[114] Here we showed that 56% of false negative biopsies had a PI-RADS 5 lesion as compared to 27% of true negative biopsies. However, due to the small number of patients that had undergone MRI, PI-RADS score was not a predictor for cribriform architecture in logistic regression analysis.

We were not able to find any predictive value of biopsy percentage Gleason pattern 4 or glomeruloid growth pattern for cribriform architecture on radical prostatectomy. Presence of cribriform architecture has been associated with higher percentage Gleason pattern 4 on biopsies. In a cohort of 370 biopsy Grade Group 2 prostate cancer patients, we found cribriform architecture in 6% of men with <10% Gleason pattern 4, in 22% of men with 10-25% pattern 4, and in 44% of men with 25-50% pattern 4. Nevertheless, biopsy percentage Gleason pattern 4 was not predictive for cribriform architecture in false negative biopsies. This paradoxical outcome could be explained by the low level of concordance between percentage Gleason pattern 4 on biopsy and matched radical prostatectomy specimens in this study. Similarly, glomeruloid Gleason pattern 4 which has been hypothesised to represent a precursor lesion of cribriform growth, was not associated with cribriform architecture in false negative biopsies.[92]

Amongst patients with cribriform architecture, those with large expansive cribriform fields have the worst outcome.[101] The false negative rate of 27% for large cribriform pattern is significantly less than the rate of 52% for overall cribriform morphology. Since 44% of true positive biopsies had large cribriform fields on radical prostatectomy as compared to only 15% of false negative biopsies, this might explain the significantly better biochemical recurrence-free survival of false negative biopsies as compared to true positive biopsies, in addition to other clinicopathological confounding factors.

The strong points of this study are the detailed histological review of matched biopsies and radical prostatectomies. The study is however limited by its low number of patients, the heterogeneity of the study population including both patients with first-time diagnosis and progression during active surveillance, and variability of diagnostic work-up encompassing systematic and/or targeted biopsies as well as multiparametric MRI assessment. Finally, follow-up is relatively short with a median of 27 months.

In conclusion, we demonstrate that 40% of men with biopsy Grade Group 2 prostate cancer were false negative for invasive cribriform and/or intraductal carcinoma. Age and PSA were independent predictors for cribriform architecture in false negative biopsies, while patients with false negative biopsies more frequently had PI-RADS score 5 lesions than men with true negative biopsies. Multimodal evaluation of biopsy Grade Group 2 prostate cancer patients could therefore identify men with true cribriform negative biopsies who might become eligible for active surveillance.

ACKNOWLEDGEMENTS

This study was supported by a generous grant from the Jaap Schouten Foundation.

CHAPTER VI

Characteristics and outcome of prostate cancer patients with overall biopsy Gleason score 3 + 4 = 7 and highest Gleason score 3 + 4 = 7 or > 3 + 4 = 7

Verhoef EI, Kweldam CF, Kümmerlin IP, Nieboer D, Bangma CH, Incrocci L,
van der Kwast TH, Roobol MJ, van Leenders GJ.

Histopathology 2018 Apr;72(5):760-765

ABSTRACT

Aims: Prostate cancer heterogeneity and multifocality might result in different Gleason scores (GS) at individual biopsy cores. According to World Health Organization/ International Society of Urologic Pathology (WHO/ISUP) guidelines, the GS in each biopsy core should be recorded with optional reporting of overall GS for the entire case. We aimed to compare the clinicopathological characteristics and outcome of men with overall biopsy GS 3+4 = 7 with highest GS 3+4 = 7 (HI = OV) to those with highest GS > 3+4 = 7 (HI > OV).

Methods and results: Prostate cancer biopsies from the European Randomised Study of Screening for Prostate Cancer (ERSPC) were revised according to WHO/ISUP 2014 guidelines (*n* = 1031). In total, 370 patients had overall GS 3+4 = 7, 60 of whom (16%) had had at least one biopsy core with GS 4+3 = 7 or 4+4 = 8. Men with higher GS than 3+4 (HI > OV) in any of the cores had higher age, prostate-specific antigen (PSA) level, number of positive biopsies, percentage tumour involvement, percentage Gleason grade 4 and cribriform or intraductal growth (all P<.05) than those with GS 3+4 = 7 at highest (HI = OV). In multivariable Cox regression analysis, including PSA, percentage positive biopsies and percentage tumour involvement, biochemical recurrence-free survival after radical prostatectomy (P=.52) or radiotherapy (P=.35) was not statistically different between both groups.

Conclusions: Among patients with overall GS 3+4 = 7, those with highest GS > 3+4 = 7 had worse clinicopathological features, but clinical outcome was not statistically significant. Therefore, the use of overall GS instead of highest GS for clinical decision-making is justified, potentially preventing overtreatment in prostate cancer patients.

INTRODUCTION

Gleason score (GS) at diagnostic biopsy is an important parameter for therapeutic decision-making in men with prostate cancer. According to the International Society of Urologic Pathology (ISUP) and World Health Organization (WHO) guidelines, pathologists should grade each biopsy containing cancer separately, provided that individual cores can be identified, and may also give an overall score for the entire case.[36, 115] However, prostate cancer heterogeneity and multifocality might result in variability of individual biopsy core GS. In such cases it is not evident which GS should be recorded for patient stratification and treatment. For instance, a patient might have one biopsy core presenting with 6 mm GS 3+3 = 6 and another biopsy core with 2 mm GS 4+3 = 7. In this case, stratification might be based either on the overall GS 3+4 = 7 or highest GS 4+3 = 7. Discordancy between overall and highest GS particularly affects men with GS 7, as optimal individual therapeutic strategies are not well defined in this subgroup.[116] Studies on overall and highest GS show conflicting results, and have not focused on GS 3+4 = 7 in particular.[117-120] We aimed to compare the clinicopathological characteristics and outcome of men with overall biopsy GS 3+4 = 7 with highest GS 3+4 = 7 (HI = OV) to those with highest GS > 3+4 = 7 (HI > OV).

MATERIALS AND METHODS

Patient selection

Prostate biopsies were taken in the scope of the European Randomised Study of Screening for Prostate Cancer (ERSPC) section Rotterdam, initial screening round, the trial protocol of which has been published previously.[121, 122] Each individual biopsy core was included in a separate container facilitating detailed pathological evaluation. Three investigators (C.F.K., I.P.K., G.V.L.) reviewed all prostate biopsies taken between November 1993 and March 2000 according to WHO/ISUP 2014 guidelines.[9, 36, 83, 115] Cases were excluded when no slides were present for review or when metastasis was present at time of diagnosis. For each biopsy core GS, percentage tumour involvement, the presence of invasive cribriform or intraductal carcinoma (CR/IDC) and percentage Gleason 4 was recorded. Overall GS was determined by adding the most common and the highest grade in all biopsy cores. Highest GS referred to the individual biopsy core with the maximal GS of all biopsy cores. Percentage tumour involvement was defined as the total tumour length including intervening benign glands (mm) divided by the total biopsy length (mm). Percentage Gleason grade 4 was defined as the relative amount of Gleason grade 4 compared to the total number of tumour glands.

Clinical follow-up

Patients were monitored semi-annually after diagnosis and initial treatment to assess potential progression and secondary treatment. Biochemical recurrence after radical prostatectomy (RP) was defined as two sequential prostate-specific antigen (PSA) levels of ≥ 0.2 ng/ml, or any PSA increase > 2 ng/ml higher than the lowest PSA value after radiotherapy (RT).[123, 124] An independent cause-of-death committee reviewed cause of death, including deaths related to screening within the prostate cancer deaths, and determined disease-specific survival (DSS).[125]

Statistical analysis

Categorical parameters were analysed using Pearson's chi-square (χ^2). Normally distributed continuous parameters were analysed using the Student's *t*-test and non-normally distributed continuous parameters with the Mann–Whitney *U*-test. Crude and adjusted hazard ratios (HRs) for biochemical recurrence-free survival (BCRFS) and DSS were estimated using Cox regression analysis, in which men lost to follow-up or death of other causes were censored. P-values were calculated using the likelihood-ratio test, considering two-sided P-values of $< .05$ as statistically significant. All statistics were performed in R version 3.2.2 (R Foundation, Vienna, Austria).

RESULTS

Patient characteristics

The mean age of the entire study population (*n* = 1031) was 66 years (median: 67, interquartile range (IQR): 62–71) and the mean follow-up was 13 years (median: 15, IQR: 9.4–16). At the time of diagnosis, mean PSA level was 8.8 ng/ml (median: 5.6, IQR: 3.9–8.8), with an average of three positive biopsies (median: 2, IQR: 1–4). In 932 of 1031 patients (90%), overall and highest GS were identical, while 98 men (10%) had an overall GS lower than the highest GS (Table 1). One patient presented with highest GS 3+5 = 8 but overall GS 4+5 = 9, explained by the presence of another biopsy with 4+3 = 7.

Table 1. Overall and highest biopsy Gleason scores of the entire cohort (n=1031).

	Overall Gleason score					
Highest Gleason score	GS 6	GS 3+4=7	GS 4+3=7	GS 8	GS 9-10	Total
GS 6	486	0	0	0	0	486
GS 3+4=7	0	310	0	0	0	310
GS 4+3=7	0	54	50	0	0	104
GS 8	0	6	19	38	*1*	64
GS 9-10	0	0	0	*19*	48	67
Total	486	370	69	57	49	1031

Clinicopathological characteristics of biopsy GS 3+4=7

In total, 370 men had overall biopsy GS 3+4 = 7, 60 of whom (16.2%) had at least one core with a higher GS (HI > OV); 54 of 370 (14.6%) had the highest GS 4+3 = 7 and six of 370 (1.6%) GS 4+4 = 8. Age (P = .016), PSA (P<.001), number of positive biopsies (P<.001), percentage tumour involvement (P=.001), presence of CR/IDC growth (P<.001) and percentage Gleason grade 4 (P<.001) were all significantly higher in men with GS 4+3 = 7 or 4+4 = 8 in individual cores (HI > OV) than in men with highest GS 3+4 = 7 (HI = OV; Table 2). As primary treatment, a total of 146 men (39%) underwent RP, 195 (53%) received RT, 25 (8%) were included in an active surveillance protocol and three (1%) received endocrine therapy; treatment was unknown in one case.

Clinical outcome of biopsy GS 3+4=7

The mean follow-up of the overall GS 3+4 = 7 cohort was 13 years (median: 14, IQR: 9.6–17). Primary treatment of men with a biopsy core with GS 4+3 = 7 or GS 4+4 = 8 was significantly more often RT (41 of 60; 68%) than of patients without higher GS (154 of 310; 50%; P=.012). BCR occurred in 35 of 146 (24%) men after RP and 72 of 195 men (37%) after RT.

Extra-prostatic extention at RP was present in 37 of 129 cases with highest GS 3+4 = 7 (HI = OV) at biopsy (29%) and in nine of 17 cases (53%) with highest GS > 3+4 = 7 (HI > OV; P=.054), with one case presenting with seminal vesicle invasion. Surgical margins at RP were positive significantly more often in men with a biopsy core with GS 4+3 = 7 or GS 4+4 = 8 (10 of 17; 59%) than in men with highest GS 3+4 = 7 (38 of 129; 29%; P=.03). As we did not have information on the modified GS at RP according to ISUP/WHO 2005 or 2014 guidelines, we were unable to compare GS at RP. Although the presence of a higher GS in men with overall GS 3+4 = 7 (HI > OV) approached significance in predicting BCRFS after RP in univariate analysis (HR: 2.1, 95% confidence interval (CI): 0.91–4.8; P=.08), no relation was found when PSA, number of positive biopsies and tumour involvement were taken into account (HR: 1.4, 95% CI: 0.50–3.9; P=.52; Table 3).

Table 2. Clinicopathologic characteristics of prostate cancer patients with overall GS 3+4=7 and highest GS 3+4=7 (HI=OV) or GS >3+4=7 (HI>OV).

	Mean (median, IQR) or n (%)		
	Highest GS 3+4=7 (n=310)	Highest > GS 3+4=7 (n=60)	P-value
Age (years)	67 (67, 62-71)	68 (69, 65-73)	.016[a]
PSA ($\log_2$, ng/ml)	2.7 (2.5, 2.0-3.2)	3.3 (3.2; 2.5-4.2)	<.001[b]
Number of positive biopsies	2.9 (3.0, 2.0-4.0)	4.4 (4.0, 3.0-6.0)	<.001[b]
Tumour involvement (%)	43 (43, 26-57)	53 (55, 37-66)	.001[b]
Presence of CR/IDC	54 (17)	34 (57)	<.001[c]
Gleason grade 4 (%)	16 (13, 6.5-23)	33 (36, 27-40)	<.001[b]
Disease specific death	14 (5)	9 (15)	.005[c]

[a]Students t-test, [b]Mann-Whitney U, [c]Chi-Squared.

Table 3. Uni- and multivariable analysis of biochemical recurrence free survival after radical prostatectomy.

	Univariate			Multivariable		
	HR	95% CI	P-value	HR	95% CI	P-value
Age (years)	1.0	0.95-1.1	.49	1.0	0.94-1.1	.74
PSA (ng/ml)[a]	1.2	0.82-1.8	.33	1.1	0.71-1.8	.63
Positive biopsies (%)	3.7	0.85-16	.08	2.6	0.48-14	.27
Tumour involvement (%)	2.2	0.50-9.8	.30	2.0	0.44-9.1	.38
Higher Gleason score	2.1	0.91-4.8	.08	1.4	0.50-3.9	.52

[a]Per doubling unit. CI, confidence interval; HR, hazard ratio

Presence of a GS > 3+4 = 7 (HI > OV) on biopsy was associated with BCRFS after RT in univariate analysis (HR: 2.4, 95% CI: 1.5–4.0; P<.001). In multivariable analysis, percentage positive biopsies (HR: 7.8, 95% CI: 2.7–23; P<.001) and percentage tumour involvement (HR: 4.1, 95% CI: 1.3–13; P=.015) were associated significantly with BCFRS, while the presence of a higher GS was not (HR: 1.3, 95% CI: 0.75–2.3; P=.35; Table 4). In total, 21 men (11%) died of prostate cancer after RT and one after RP. Presence of a higher GS in overall GS 3+4 = 7 patients (HI > OV) was associated with DSS after RT in univariate analysis (HR: 3.4, 95% CI: 1.5–8.9, P=.005), but not in multivariable analysis (HR: 1.8, 95% CI: 0.71-4.7; P=.21; Table 5).

Table 4. Uni- and multivariable analysis of biochemical recurrence free survival after radiation therapy.

	Univariate			Multivariable		
	HR	95% CI	P-value	HR	95% CI	P-value
Age (years)	1.0	0.95-1.0	.90	1.0	0.96-1.1	.79
PSA (ng/ml)[a]	2.0	1.7-2.5	<.001	1.7	1.4-2.1	<.001
Positive biopsies (%)	20	7.7-52	<.001	7.8	2.7-23	<.001
Tumour involvement (%)	7.6	2.7-21	<.001	4.1	1.3-13	.015
Higher Gleason score	2.4	1.5-4.0	<.001	1.3	0.75-2.3	.35

[a]Per doubling unit. CI, confidence interval; HR, hazard ratio

Table 5. Uni- and multivariable analysis of disease specific survival after radiation therapy.

	Univariate			Multivariable		
	HR	95% CI	P-value	HR	95% CI	P-value
Age (years)	1.1	0.97-1.2	.186	1.1	0.98-1.2	.12
PSA (ng/ml)[a]	2.2	1.5-3.3	<.001	1.8	1.2-2.8	.0045
Positive biopsies (%)	29	5.0-167	<.001	8.4	1.2-59	.03
Tumour involvement (%)	19	2.5-146	.004	12	1.1-122	.04
Higher Gleason score	3.4	1.5-8.9	.005	1.8	0.71-4.7	.21

[a]Per doubling unit. CI, confidence interval; HR, hazard ratio

DISCUSSION

In the current study, we showed that 16% of men with overall biopsy GS 3+4 = 7 had at least one biopsy containing GS 4+3 = 7 or GS 4+4 = 8. These patients presented with higher PSA, more positive biopsies, higher percentage tumour involvement and more frequent CR/IDC growth. Despite these adverse features, presence of biopsies with higher GS (HI > OV) was not an independent predictive parameter for BCFRS after RP or RT when PSA, number of positive biopsies and percentage tumour involvement were taken into account.

Our findings are in concordance with those of Berney *et al*., who showed that overall and worst biopsy GS have similar predictive value for prostate cancer death in conservatively treated patients, and Tolonen *et al*., who showed a similar result for BCRFS after endocrine therapy.[117, 120] The rationale for using overall GS is the assumption that all biopsies are derived from one heterogeneous prostate cancer, and thus all single patterns should be considered part of the same tumour. Conversely, tumour multifocality is the motivation to consider the highest GS as the most relevant. As biopsies with different GS might represent separate tumours with variable GS, use of the highest GS precludes unwarranted down-grading of an aggressive tumour due to contamination with separate tumours with lower GS.[126, 127] Muezzinoglu *et al*. showed that the number of positive biopsies was not correlated with the number of tumour foci found in RPs, and we are not aware of other studies relating biopsy location outcomes to separate multifocal tumours at RP.[128]

The findings of this study and others indicate there is no scientific evidence for the preferential use of either overall or highest GS in clinical practice.[117, 120] Biopsy GS is an important parameter for clinical decision-making in prostate cancer patients, and although overall and highest GS are concordant in most patients, discordancy might lead to uncertainty on further treatment decisions. If the highest GS is considered, this might lead to overtreatment in a significant number of men. In order to prevent this, therapeutic decisions could be based on overall GS as long as other parameters such as PSA and number of positive biopsies are taken into account.

Even though patients with overall GS 3+4 = 7 but individual cores with higher GS than 3+4 = 7 (HI > OV) had adverse clinicopathological features, this did not account independently for worse outcome. This paradoxical result could be explained by influence of tumour volume parameters. When the highest GS was higher than the overall GS (HI > OV), by definition at least two biopsy cores were involved, while patients with one positive biopsy core always have similar overall and highest GS. In addition, men with dissimilar highest and overall GS generally have a higher tumour involvement of all biopsies ‘compensating’ for overall GS down-grading. In this study, both the number of positive biopsies and percentage tumour involvement were, indeed, independent parameters for BCRFS after RP and DSS.

While most men with GS 3+4 = 7 will be offered active treatment, active surveillance is considered increasingly in this group of patients.[129, 130] Generally, urologists will be hesitant to consider surveillance if individual biopsy cores contain GS 4+3 = 7 or GS 4+4 = 8, as this implicates the presence of aggressive disease components. It is acknowledged increasingly that histopathological parameters beyond GS such as percentage Gleason grade 4, the presence of invasive cribriform growth or intraductal carcinoma contribute significantly to risk stratification. For instance, men with non-cribriform GS 3+4 = 7 have similar BCRFS and DSS to those with biopsy GS 6, while patients with cribriform GS 3+4 = 7 behave significantly worse.[9, 83] To support optimal individual decision-making it is important that these pathological parameters are reported routinely and included in risk stratification models.

A limitation to our study is the sextant biopsy protocol used in the ERSPC first screening round, while current protocols include a significantly higher number of biopsies.[131] In addition, multiparametric magnetic resonance imaging (MRI) was not performed in the early 1990s, and RNA expression profiling for risk stratification was not available. Although RPs performed in the scope of the ERSPC were retrieved and reviewed in the 1990s, respective ‘classic’ GS could not be compared with current modified GS. Finally, the number of men with biopsy GS 3+4 = 7 was relatively low in our retrospective study, limiting the power to reveal subtle differences between groups.

In conclusion, we show that 16% of men with overall GS 3+4 = 7 have individual biopsies with a higher GS. Although these patients have adverse features on biopsy and RP, we found no significant difference in BCFRS or DSS between overall and highest GS in multivariable models. Therefore, the use of overall GS for clinical decision-making is justified to potentially prevent overtreatment in a significant number of prostate cancer patients, as long as other clinical parameters on tumour load are taken into account.

CHAPTER VII

Comparison of tumour volume parameters on prostate cancer biopsies

Verhoef EI, Kweldam CF, Kümmerlin IP, Nieboer D, Bangma CH, Incrocci L,
van der Kwast TH, Roobol MJ, van Leenders GJ.

Archives of Pathology and Laboratory Medicine. 2020 Jan 6

ABSTRACT

Aims: Prostate biopsy reports require an indication of prostate cancer volume. No consensus exists on the methodology of tumour volume reporting. We aimed to compare the prognostic value of different biopsy prostate cancer volume parameters.

Methods & Results: Prostate biopsies of the European Randomized Study of Screening for Prostate Cancer were reviewed (n=1031). Tumour volume was quantified in six ways: average estimated tumour percentage, measured total tumour length, average calculated tumour percentage, greatest tumour length, greatest tumour percentage, and average tumour percentage of all biopsies. Their prognostic value was determined using either logistic regression for extra-prostatic expansion (EPE) and surgical margin (SM) status after radical prostatectomy (RP), or Cox regression for biochemical recurrence-free survival (BCRFS) and disease-specific survival (DSS) after RP (n=406) and radiation therapy (RT) (n=508). All tumour volume parameters were significantly mutually correlated ($R^2 > 0.500$, $P<.001$). None were predictive for EPE, SM or BCRFS after RP in multivariable analysis including age, PSA, number of positive biopsies and Grade group. In contrast, all tumour volume parameters were significant predictors for BCRFS (all $P<.03$) and DSS (all $P<.04$) after RT, except greatest tumour length. In multivariable analysis including only all tumour volume parameters as covariates, calculated tumour length was the only predictor for EPE after RP ($P=.024$) and DSS after RT ($P=.015$).

Conclusions: All tumour volume parameters had comparable prognostic value and could be used in clinical practice. If tumour volume quantification is a threshold for treatment decision, calculated tumour length seems preferential, slightly outperforming the other parameters.

INTRODUCTION

Men suspicious for prostate cancer receive biopsies to determine the presence and aggressiveness of a potential tumour. Apart from Gleason score (GS) and number of positive biopsies, an indication of tumour volume should be provided in pathology reports.[132] The College of American Pathologists and the World Health Organization (WHO) state that either linear cancer volume or proportion of prostate tissue involved by cancer should be reported as parameter for biopsy tumour volume.[133, 134] Biopsy tumour volume has been associated with outcome after radical prostatectomy (RP) and radiation therapy (RT), however tumour volume representation varies amongst studies.[15-17, 135] In addition, biopsy tumour involvement is an important threshold for patient eligibility for some active surveillance protocols, underlining the need for objective and reliable tumour volume quantification.[111, 136] It is yet unknown to what extent tumour volume parameters are mutually related and whether they all have similar prognostic value. The aim of this study was to compare different tumour volume parameters in relation to clinical outcome in a large prostate biopsy cohort.

MATERIALS AND METHODS

Patient selection

Prostate biopsy cores were taken in the scope of the European Randomized Study of Screening for Prostate Cancer (ERSPC), initial screening round between November 1993 and March 2000, of which the trial protocol has been published previously.[121, 122] Participating men underwent sextant prostate biopsies according to the study protocol, with addition of extra 7th or 8th biopsy in case of an hypoechoic lesions Transrectal Ultrasound (TRUS). Each individual biopsy core was embedded in a separate container to enable detailed pathologic evaluation. Three investigators reviewed all prostate biopsies according to the WHO and International Society of Urological Pathology (ISUP) 2014 guidelines.[9, 36, 83, 115] In case no slides were present for review or if metastasis was present at time of diagnosis, cases were excluded. For each patient, GS, Grade group, total number of biopsies, number of prostate cancer positive biopsies and tumour volume were recorded. The study was approved by the local Medical Ethics Committee (MEC-2018-1614).

Tumour volume quantification

Tumour volume was quantified in six different ways, as depicted in Fig. 1. First, estimated tumour percentage per core was determined by eyeballing. The average estimated tumour percentage for the entire case was calculated by dividing the sum of the estimated percentages per core by the total number of prostate cancer positive biopsies per patient. Second, measured total tumour length was defined as the sum of the tumour lengths in all biopsies containing cancer as measured in mm using a micro-ruler. Third, the average calculated tumour percentage was determined by dividing the sum of the tumour lengths of the entire case by the total length of the prostate cancer positive biopsies of the entire case as measured in mm using a micro-ruler. Fourth, greatest tumour length was defined as the maximum tumour length of an individual biopsy core per patient as measured by a micro-ruler in mm. Fifth, greatest tumour percentage was defined as the maximum tumour percentage on an individual core per patient. Sixth, average tumour percentage of all biopsies was determined by dividing the sum of the estimated tumour percentages by the total number of biopsies. Assessment of each tumour volume parameter included intervening non-malignant tissue in case more than one tumour focus was present within a single biopsy.[14, 137]

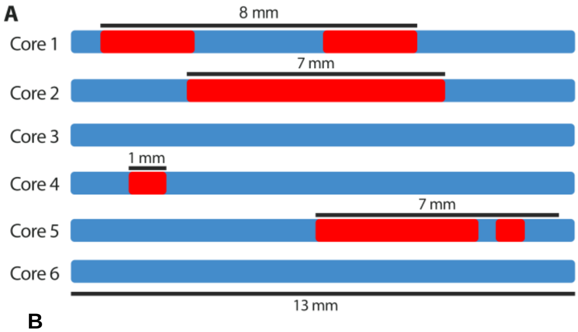

B

Individual core	Estimated percentage	Measured tumour length (mm)	Measured total core length (mm)	Calculated percentage
1	60	8	13	62
2	50	7	13	54
3	0	0	13	0
4	10	1	13	8
5	50	7	13	54
6	0	0	13	0

C

Average estimated tumour percentage	(60+50+10+50)/4=	43 %
Measured total tumour length	8+7+1+7=	23 mm
Calculated tumour percentage	((8/13)+(7/13)+(1/13)+(7/13))/4=	44 %
Greatest tumour length	8	8 mm
Greatest tumour percentage	8/13=	62 %
Average total estimated tumour percentage	(60+50+10+50)/6=	28 %

Figure 1. Example of tumour volume quantification methods on prostate cancer biopsies of a single patient. A) Each individual core is reviewed. Total biopsy length is depicted in blue, whereas the red areas represent tumour fields. B) For each core, the tumour percentage was estimated after which the length of the total biopsy as well as the tumour area was measured. C) All the tumour volume parameters were calculated for the patient based on the biopsy measurements.

Clinical follow-up

Progression and secondary treatment were recorded by semi-annually monitoring each patient after diagnosis and initial treatment. Biochemical recurrence (BCR) was defined as two successive Prostate Specific Antigen (PSA) levels of ≥0.2 ng/ml after RP, or any PSA increase >2 ng/ml above the lowest PSA value after RT.[123, 124] An independent cause-of-death committee reviewed cause of death, including deaths related to screening within the prostate cancer deaths, and determined disease-specific survival (DSS).[125]

Statistical analysis

Correlations between tumour volume parameters were calculated using the Pearson's R^2 correlation coefficient. Parameters were log-transformed to normalise data for logistic regression analysis. Crude and adjusted odds ratios (OR) were estimated for extra-prostatic expansion (EPE, pT stage ≥3) and surgical margins (SM) status using logistic regression. Hazard ratios (HR) for biochemical-recurrence free survival (BCRFS) and DSS were estimated using Cox regression analysis, in which men lost to follow-up or death of other causes were censored. Multivariable logistic regression analysis with each separate tumour volume parameter was corrected for age, PSA, number of positive biopsies and Grade group. P-values of <.05 were considered statistically significant. All statistical analysis were performed in R version 3.2.2 (R, Vienna, Austria).

RESULTS

Patient characteristics

At time of diagnosis, the median age of the entire cohort (n=1031) was 67 years (interquartile range (IQR) 62-71 years) and median PSA level was 5.6 ng/ml (IQR 3.9-8.8 ng/ml). In total 486 men were diagnosed with GS 6 (Grade group 1) on biopsy, 370 with GS 3+4=7 (Grade group 2), 71 with GS 4+3=7 (Grade group 3), 55 with GS 8 (Grade group 4) and 49 with GS 9-10 (Grade group 5) prostate cancer. Four hundred six men (39%) were treated with RP, 508 men (49%) received RT, 8 men (1%) underwent endocrine therapy and 108 men (11%) were put on watchful waiting, while treatment was unknown for one patient. The median follow-up was 13 years (IQR 8.7-17 years).

Correlation between tumour volume parameters

In total 549 (53%) men received 6 biopsies, 460 (45%) 7 biopsies and 22 (2%) 8 biopsies. The mean total positive biopsy length per patient was 26 mm (IQR 12-36 mm) and the mean total tumour length was 11 mm (IQR 2.4-16 mm). The median estimated and calculated tumour percentages were 33% (IQR 15-55%) and 33% (IQR 15-55%) respectively. Average estimated tumour percentage strongly correlated with the average calculated tumour percentage (R^2=0.98, P<.001). Measured total tumour length moderately correlated with calculated tumour percentage (R^2=0.71, P<.001). The median greatest tumour length was 4.5 mm (IQR 2.0-7.8 mm) and the median greatest tumour percentage was 50% (IQR 20-80%). Both parameters correlated moderately with calculated tumour percentage (R^2=0.84 and R^2=0.87, respectively). Average tumour percentage of all biopsies (median 12%, IQR 3.7-26%) correlated moderately with calculated tumour percentage (R^2=0.74, Fig. 2). Since average estimated tumour percentage and calculated tumour percentage were strongly correlated, and estimated tumour percentage is more easily established in daily practice, we excluded average calculated tumour percentage from further analysis.

Pathologic features at radical prostatectomy

Of the 406 patients treated with RP, 98 men (24%) had EPE and 101 men (25%) had positive SM. Since RP specimens were not available for review we did not have information on the contemporary GS or Grade group. All tumour volume parameters were strongly associated with EPE (all P<.001) and SM status (all P<.01) in univariate analysis (Suppl. Table 1). In multivariable analysis including all tumour volume parameters as covariates, calculated tumour length was the only significant predictive parameter for EPE (P=.024), whereas none of the parameters were predictive for SM status (Table 1). Multivariable analysis including age, PSA level, Grade group, number of positive biopsies and each of the tumour volume parameters separately revealed that none of the biopsy tumour volume parameters had independent predictive value for EPE or SM status (Suppl. Table 1). In contrast, PSA and Grade group were independently associated with EPE (Suppl. Table 2).

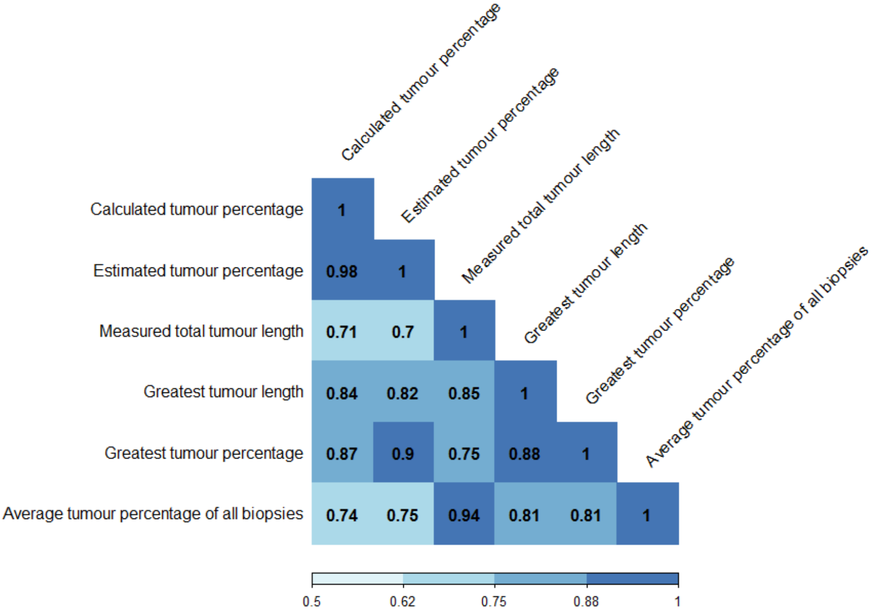

Figure 2. Schematic representation of Pearson correlations between six different tumour volume parameters. Correlation values can range between 0 and 1, where 1 is the highest possible correlation.

Table 1. Multivariable analysis of all tumour volume parameters on outcome after radical prostatectomy, including all tumour volume parameters as covariates.

	Extra-prostatic expansion			Surgical margin status		
	Adjusted OR[a]	95% CI	P-value	Adjusted OR[a]	95% CI	P-value
Estimated tumour percentage	1.2	0.6-2.4	.55	1.0	0.5-1.9	.94
Calculated tumour length	2.8	1.1-7.0	.024	2.0	0.8-4.6	.12
Greatest tumour percentage	1.0	0.4-2.5	.91	0.4	0.2-1.1	.068
Greatest tumour length	0.5	0.2-1.2	.11	0.9	0.4-2.2	.83
Average tumour percentage of all biopsies	0.9	0.4-2.1	.74	1.5	0.7-3.3	.32

[a] Per doubling unit.

Outcome after radical prostatectomy and radiation therapy

In total 85 of 406 men (20%) experienced BCR and 12 men (3%) died from their disease after RP. All biopsy tumour volume parameters were associated with BCRFS in univariate analysis (all P<.05, Suppl. Table 3). None of the parameters was significant in multivariable analysis for BCFRS including all five volume parameters (Table 2). In multivariable analysis including age, PSA level, Grade group, number of positive biopsies and each of the tumour volume parameters separately, tumour volume did not have predictive value for post-operative BCRFS, however age did (Suppl. Table 3). The low number of disease-specific deaths (n=12) did not allow statistical analysis for post-operative DSS.

Of the 508 men who received RT, 223 (44%) experienced BCR and 73 (14%) died of prostate cancer. In univariate analysis all tumour volume parameters were significantly associated with BCRFS (all P<.001, Suppl. Table 3). In multivariable analysis including all tumour volume parameters as covariates none of the parameters was significant (Table 2). Multivariable analysis including clinicopathologic parameters and each of the separate tumour volume parameters separately revealed that all individual biopsy tumour volume parameters had independent predictive value for BCFRS after RT (all P<.03, Suppl. Table 3), as well as PSA and Grade group (Suppl. Table 4). For DSS after RT, univariate analysis showed that all tumour volume parameters had significant predictive value (all P<.001, Suppl. Table 3). In multivariable analysis including all tumour volume parameters as covariates, calculated tumour length was the only positive significant predictive parameter (P=.015, Table 2). Multivariable analysis including clinicopathologic parameters and the separate tumour volume parameters showed that all biopsy tumour volume parameters except greatest tumour length had independent predictive value for DSS (all P<.05, Suppl. Table 3) as well as age, PSA and Grade group (all P<.05, Suppl. Table 4).

Table 2. Multivariable analysis of all tumour volume parameters on survival after radical prostatectomy (RP) or radiation therapy (RT), including all tumour volume parameters as covariates.

	Biochemical recurrence-free survival after RP		
	Adjusted HR[a]	95% CI	P-value
Estimated tumour percentage	1.2	0.7-2.2	.47
Calculated tumour length	0.9	0.4-1.7	.68
Greatest tumour percentage	0.5	0.3-1.3	.17
Greatest tumour length	1.5	0.7-3.2	.32
Average tumour percentage of all biopsies	1.4	0.7-2.7	.34

[a] Per doubling unit.

	Biochemical recurrence-free survival after RT			Disease-specific survival after RT		
	Adjusted HR[a]	95% CI	P-value	Adjusted HR[a]	95% CI	P-value
Estimated tumour percentage	1.1	0.8-1.6	.45	1.2	0.6-2.4	.52
Calculated tumour length	1.3	0.8-2.0	.30	2.3	1.2-4.7	.015
Greatest tumour percentage	1.0	0.6-.8	.93	1.5	0.6-3.8	.42
Greatest tumour length	0.8	0.5-1.4	.49	0.4	0.2-1.0	.039
Average tumour percentage of all biopsies	1.2	0.7-1.8	.51	1.0	0.6-2.0	.90

[a] Per doubling unit.

DISCUSSION

Biopsy tumour volume is associated with clinical outcome and represents an inclusion parameter in some active surveillance cohorts.[138, 139] While a measure of tumour volume should be included in prostate biopsy reports, no consensus exists on the method of tumour volume quantification. In this study, we analysed six different methods for tumour volume reporting. We found overall moderate to good correlation between all tumour volume parameters. All had predictive value for EPE, SM status and BCRFS after RP, as well BCFRS and DSS after RT in univariate analysis. In multivariable analysis including all tumour volume parameters as covariates, calculated tumour length was the only predictor for EPE after RP and DSS after RT. Since their predictive value is comparable, all tumour volume parameters are acceptable for pathological reporting with calculated tumour length being slightly better in predicting some of the endpoints.

The lack of standardisation in biopsy tumour volume parameters leads to use of a wide variety of parameters in clinicopathological studies. While tumour volume measurements are associated with adverse outcome after RP in many studies, results on their independent predictive value in multivariable analysis are inconsistent.[18, 140-146] Here, we found that none of the volume parameters was independently predictive for BCRFS after RP. Discordant outcomes between studies can be explained by the application of tumour volume cut-off values in some studies, which might introduce study biases.[147] Furthermore, the clinicopathologic parameters included in multivariable analyses are highly variably amongst studies, potentially omitting relevant confounding factors.

The relation between tumour volume and outcome after RT has not yet been thoroughly studied. While greatest percentage tumour involvement was predictive for BCR in univariate analysis in several studies, it was not predictive when other clinicopathologic parameters were included in multivariable analysis.[148-150] This is in contrast with our study, in which we show independent predictive value of tumour volume parameters for BCRFS and DSS after RT. This can be explained by inclusion of different clinicopathologic covariates, size of patient cohorts and use of continuous variables instead of cut-offs.

In this study we show strong correlations between the biopsy tumour volume quantification methods and comparable predictive value for clinical outcome. In multivariable analyses including all tumour volume parameters, calculated total tumour volume outperformed the other quantitative parameters for prediction of post-operative EPE and DSS after RT. In their study of multiple tumour measurements, Brimo *et al*. found total tumour length as best predictive quantifier for post-operative BCRFS.[151] Calculated tumour length is a simple quantitative measurement that can objectively be assessed as compared to estimated tumour volume measurements and might be easily comparable between studies. A weakness of total calculated tumour length is that its quantification can be time consuming when many positive biopsies are present, in which case an estimated tumour percentage or maximal tumour length might be more easy to assess. The impact of tumour volume assessment might be strongest on selection of patients for active surveillance. Some surveillance protocols include tumour volume parameters such as 20% or 50% tumour involvement as criteria for eligibility, stressing the importance of reliable tumour volume quantification.[111, 136] Whereas estimated tumour percentage can be determined by eyeballing and is less time-consuming, it is not as not as objective as measuring tumour length and might result in volume overestimation in small biopsy specimens. A practical solution could be that estimated tumour percentage is given in all patients and that in case of potential surveillance eligibility objective calculated tumour length is added.

A strong point of this study is its inclusion of patients from a well-characterised screening cohort with long term follow-up. An inherent limitation of this screening cohort from the 1990s was that it included sextant biopsies, while current biopsy protocols generally include a larger number of systematic biopsies, often together with additional magnetic resonance imaging targeted biopsies.[131] Finally, we were not able to re-evaluate the tumour grade at RP specimens according to the 2014 WHO/ISUP guidelines since most of the surgical procedures were performed in other hospitals.

In conclusion, all tumour volume parameters showed moderate to strong mutual correlation, had comparable prognostic value for outcome after RP and RT, and could be used in clinical practice. In case tumour quantification is a threshold for treatment decisions, such as eligibility for active surveillance, calculated tumour length seems preferential since it slightly outperformed the other parameters and is an objective quantitative measurement.

Supplementary Tables may be found in the online version of this article.

CHAPTER VIII

General discussion

INTRODUCTION

Pathologists examine thin tissue sections under a microscope for disease diagnosis, and as a consequence grading is based on one single moment in time of a dynamically growing tumour. Transitions and mutual relations between tumour patterns cannot be appreciated on these thin sections. In the current chapter an overview will be provided of the two- and three-dimensional morphology of benign as well as cancerous prostate glands and the implications of our findings, with a special focus on the mutual relationships of cancerous growth patterns and their clinical relevance.

Pathology: a brief history

Since the 1960's, pathological grading of prostate cancer on biopsies and radical prostatectomy specimens is done using the Gleason score, which is based on the presence of architectural tumour growth patterns on thin two-dimensional hematoxylin and eosin (HE) stained tissue sections.[6] It is considered the most important parameter for patient prognosis and clinical decision making. Since its development it has been subject to change but only recently there is increased interest for the prognostic value of individual growth patterns behind the different tumour grades, especially within Gleason grade 4.[152, 153] It has previously been shown that cribriform Gleason grade 4 is associated with adverse patient outcome in contrast to the other grade 4 growth patterns, suggesting it could be the most relevant growth pattern for patient prognosis.[84, 102, 154] Apart from their prognostic value, understanding of individual prostate cancer growth patterns could explain the substantial inter-observer variability amongst pathologists when assigning Gleason grade 4.[43, 87, 155] When pathologists misinterpret Gleason grade 3 glands for Gleason grade 4 glands, this can have major implications for the treatment of the patient. Hence, it is needed to shed light on the three-dimensional growth and mutual coherence of the static growth patterns, and to provide evidence for their differences in biological behaviour and prognostic value.

The road to three-dimensional imaging

Better understanding the actual growth of prostate glands can be achieved when the structures are viewed in their original three-dimensional shape, for which miscellaneous techniques are available. For formalin-fixed, paraffin-embedded (FFPE) tissues the most commonly used method is serial tissue sectioning followed by staining and imaging of numerous slides, as this usually does not require additional expensive equipment and is the easiest method to implement in routine practice.[40, 41, 54, 156] However, this technique is laborious and has several disadvantages, such as loss of detail, folds and cracks in the tissue, and distortion and uneven staining, which have major impact on the three-dimensional reconstructions. On top of that, serial sectioning removes the spatial connections between structures and introduces discontinuity in the three-dimensional renderings.[157]

Thus, it would be preferred to use unsectioned tissue samples to visualise the glands in their original context. However, tissue is not transparent due to the scattering of light passing through the sample and structures deep within the tissue can therefore not be visualised. Scattering is caused by the refraction of light by each of the different molecules and cells within the tissue, and limits imaging of structures in thick samples. The molecular inhomogeneity causing the scattering can be reduced by matching the refractive indexes of the tissue and the surrounding medium, leaving the tissue optically transparent. Many different protocols are available to achieve optical transparency, for instance simple immersion, hyperhydration and solvent based clearing.[32, 158] However, none of these protocols were optimised yet for use with FFPE tissues and we found that simple immersion and hyperhydration protocols were not feasible for these specimens (data not published). For solvent based clearing, multiple protocols were published for fresh-fixed tissues, but none were used in combination with embedded archival tissues yet.[35, 49] Since archival FFPE tissues offer the opportunity to select and study specific regions and growth patterns of interest, we wanted to optimise one of the solvent based protocols for these tissues. In 2016 our group was the first to successfully apply an adapted solvent based clearing protocol on fresh and FFPE prostate tissue, enabling us to image fluorescent nuclear dyes as well as fluorescently labelled antibodies up to a depth of 800 µm.[67] Below, I will discuss the findings from our three-dimensional reconstructions of benign as well as cancerous prostate lesions and the implications of these findings.

About benign prostate cancer mimickers

Several benign prostate lesions present with a prostate cancer-like morphology on HE sections, especially atrophy and adenosis.[70-72] In some cases it is even necessary to apply additional immunohistochemistry to distinguish them from true cancer.[63, 64, 66] The four most commonly appearing atrophic lesions showed three-dimensional acinar growth similar to pre-existent glands, supporting their benign nature and clearly distinguishing them from cancerous glands.[68, 159] While investigating these four variants we discovered an atrophic variant not described before, characterised in three-dimensions by atrophic spaces with a Golgi-like morphology, running parallel to the prostate surface. On HE sections, these glands were represented by thin, elongated tubular structures. Due to its three-dimensional morphological similarity to the Golgi-system, we designated these glands Golgi-like atrophy. We consider it likely that these glands are the result of compression of pre-existent glands, for instance by expanding benign hyperplastic nodules.[159]

Another common prostate cancer mimicker is adenosis.[160, 161] In fact, Beltran *et al*. recently published that adenosis can be held accountable for most false-positive prostate biopsies.[162] In stark contrast to the previous atrophic structures, our three-dimensional renderings showed that adenosis presented with a similar three-dimensional architecture as low-grade prostate cancer and could only be distinguished by the presence of basal cells. Since its three-dimensional structure is so alike that of low-grade prostate cancer, one might think of adenosis as a prostate cancer precursor, however, data on its molecular background is contradictory. Whereas some studies show that adenosis might contain allelic imbalances indicative for prostate cancer, it does not contain other prostate-cancer specific genetic abnormalities such as the TMRPSS:ERG fusion.[76, 77, 163] Further molecular investigation of adenosis might elucidate its morphological resemblance to prostate cancer.

Pre-malignant prostate lesions

The most common prostate lesion considered as prostate cancer precursor is high-grade prostate intra-epithelial neoplasia (HGPIN), however its relationship with invasive cancer is not entirely clear yet. For instance, multiple studies have described a potential continuum between HGPIN and invasive cancer, as they share similar genetic alterations such as 8p12-21 allelic loss.[164-167] However, it is not clear yet in what way HGPIN and prostate cancer are connected and whether HGPIN is a true precursor of invasive prostate cancer.[31, 168] Unfortunately, even though we sampled multiple HG-PIN glands for three-dimensional imaging, we were not able to visualise areas containing HGPIN transitioning to invasive cancer.[159]

Whereas intraductal carcinoma of the prostate (IDC-p) has been acknowledged as a malignant lesion, it is not incorporated in the Gleason grading system and its origin is still under investigation.[153] Some studies regard IDC-p as pre-existent ducts containing retrograde invading tumour cells from the vicinity.[169, 170] In contrast, others have shown that IDC-p can also exist without invasive carcinoma in the same specimen, and therefore postulate that it represents a precursor of prostate cancer.[171, 172] Dawkins *et al*. used molecular analysis to show that IDC-p cannot be regarded as an extension or invasion of cancerous glands and showed that IDC-p does not share the same allelic losses as invasive cancer, suggesting that these lesions are separate events in prostate cancer evolution.[173] Currently, common thought is that IDC-p is formed by the invasion and spread of high-grade cancer into pre-existent ducts.[174] On thin HE and immunohistochemistry slides potential transitions between IDC-p and invasive cancer can be seen (Fig. 1A). We selected several of these regions for three-dimensional imaging, and found that the pre-existent glands containing IDC-p proliferations sprouted simple round tubules with scarce and scattered basal cells (Fig. 1B-D). The concept of tumour outgrowth could not be appreciated on thin tissue sections, however it would explain the scattered presence of basal cells in tumour glands surrounding IDC-p. As outgrowing tumour cells break through the basal cell layer of the pre-existent duct, they could pull along some of the basal cells. Unfortunately we were not able to determine the relationship between IDC-p and invasive cancer in detail since the IDC-p glands often proved larger than our microscopic field of view. In addition, the glandular crowding of these areas hindered us in distinguishing the individual transitions.

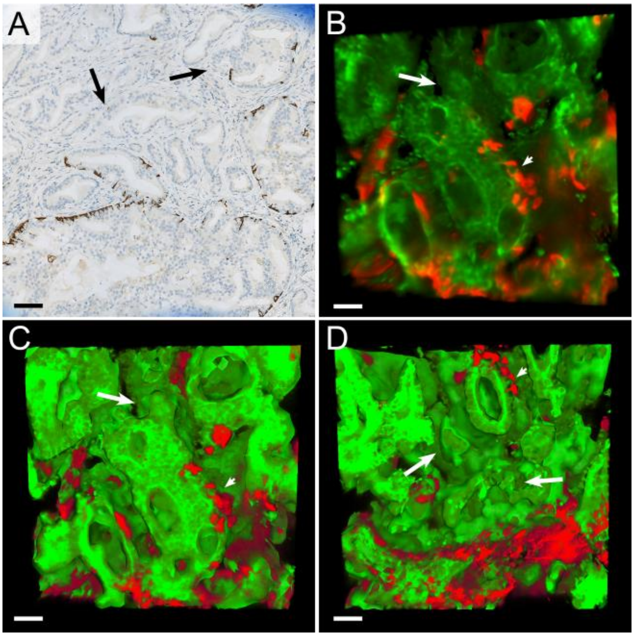

Figure 1. Transition between an intraductal gland and invasive prostate cancer. A) Immunohistochemical slide with intraductal carcinoma transitioning to invasive carcinoma, characterised by loss or scarce appearance of CK5 positive brown basal cells (arrows). B) Three-dimensional ImageJ and C) Amira rendering of the same case, where the intraductal gland with multiple basal cells (arrowhead) sprouts invasive tubules with scarce appearance of basal cells (arrow). D) Flipside of the Amira rendering, where the intraductal gland sprouted invasive prostate cancer tubules with scarce basal cells (arrows) as well as intraductal tubules with multiple basal cells (arrowheads). Original magnifications 20 ×; brown Keratin 5 in immunohistochemistry (A); green, Keratin 8/18 and red, Keratin 5 immunostaining in three-dimensional renderings. Scalebars: 100 µm.

Prostate cancer in a new dimension

Previous studies on the three-dimensional architecture of prostate cancer used serial sectioning, staining and alignment of FFPE sections to investigate its underlying morphology. For instance, Boag *et al*. showed that Gleason pattern 3 tubules consisted of an interconnecting network of tubules.[30] More recently, Tolkach *et al*. was the first to use serial sectioning on tissue from a prostate cancer patient with GS 3+4=7, describing connections between Gleason grade 3 and poorly-formed grade 4 glands.[31] However, aforementioned results are based on single cases and lack investigation of multiple growth patterns. Since Gleason grades are represented by a multitude of individual growth patterns, we hypothesised that intact tissue imaging might reveal connections between other individual prostate cancer growth patterns as well.

In contrast to the traditional grading system, our three-dimensional renderings revealed that Gleason pattern 3 and poorly-formed, fused and glomeruloid Gleason pattern 4 glands formed a structural continuum. In addition, we found that this structural continuum was extended by transition from the Grade 4 poorly-formed pattern into Gleason grade 5 single cells and cords.[175] We defined this continuum as one with interconnecting tubules with decreasing diameter, where the vast majority of tumour cells makes contact with the surrounding stroma. On the other hand, we found a second morphological continuum consisting of cribriform Gleason grade 4 glands and solid Gleason grade 5 fields with or without necrosis, which we defined as glands with contiguous tumour cells, where the vast majority of tumour cells did not make contact with the stroma (Fig. 2). Importantly, we did not find transitions or connections between the glands of the first and the second continuum.

Our model, consisting of two prostate cancer growth continuums, explains the substantial inter-observer variability of the current Gleason scoring system, as that assigns a tumour grade on static morphological features which in reality form a dynamic continuum. Many recent studies have shown that cribriform growth has an adverse prognosis and is highly associated with the development of metastasis, as opposed to other Gleason grade 4 patterns.[84, 102, 154, 176] Additionally, the outcome of patients presenting with Gleason score 3+4=7 without cribriform growth on biopsy tends towards that of patients with Gleason score 3+3=6.[83, 177] On the molecular level, two separate studies have shown that copy number alterations found in metastatic prostate cancer were enriched only in the cribriform growth pattern, indicating a clonal relation.[96, 178] In addition, a recent study by Böttcher *et al*. revealed no significant differences in genetic abnormalities between Gleason score 3+4=7 patients without cribriform and Gleason score 3+3=6 patients.[94] These results are completely in line with the three-dimensional continuity of these patterns as revealed in our studies. The biological relationships between the individual growth patterns as a continuum should be investigated further through molecular characterisation and in vivo models.

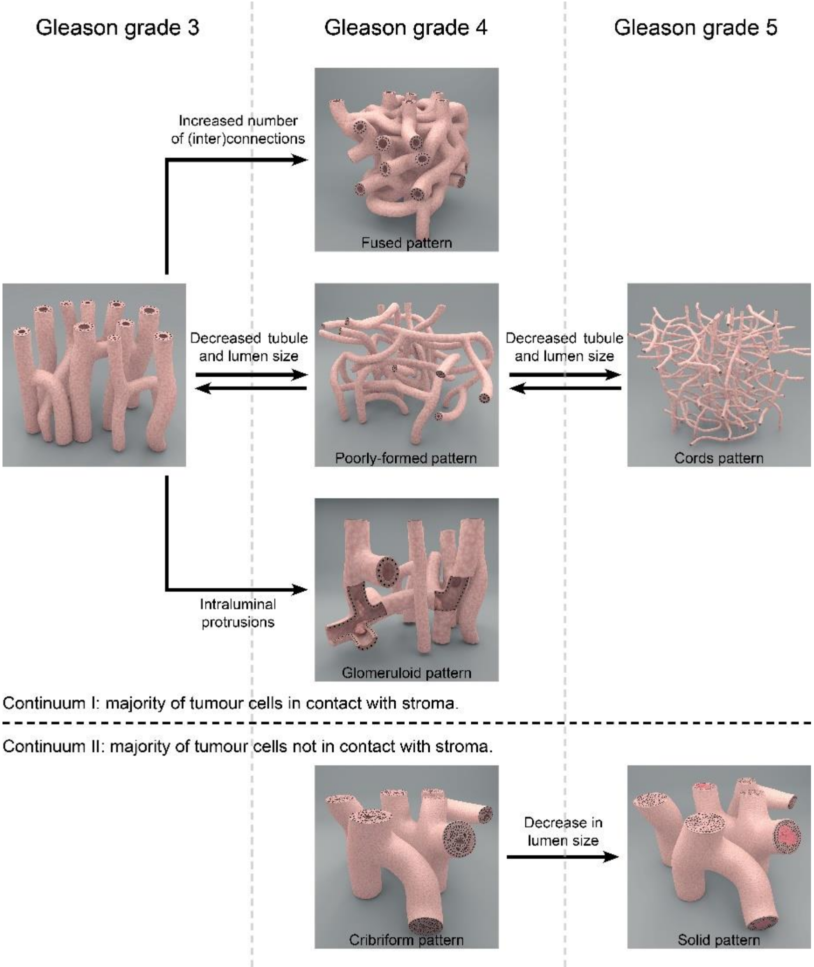

Figure 2. Proposed model with two structural growth pattern continuums. Continuum I exists of a tubular continuum where the majority of tumour cells make contact with the surrounding stroma, including Gleason pattern 3, fused, poorly formed and glomeruloid Gleason pattern 4, and single cells and cords Gleason pattern 5. Continuum II comprises epithelial proliferations where the majority of tumour cells do not make contact with the surrounding stroma, including cribriform Gleason grade 4 and solid Gleason grade 5.

Consequences of the dynamic continua

One of the major disadvantages of current pathological grading of prostate cancer is the substantial inter-observer variability in grading of Gleason grade 3, poorly-formed Gleason grade 4 and fused Gleason grade 4 glands, since these glands cannot always be well distinguished. On the other hand, the inter-observer agreement for the cribriform growth pattern is excellent.[43, 87, 88, 98] The first dynamical continuum as proposed in this thesis could provide an explanation for the high inter-observer variability mentioned above, considering that the changing and developing tumour merely shows tubules transforming from Gleason grade 3 to Gleason grade 4 poorly-formed or fused and vice versa. Considering that patients presenting with these non-cribriform Grade 4 patterns on biopsy have outcomes tending towards that of patients with Gleason score 3+3=6, the inter-observer variability might not be as important as thought before, as long as the cribriform pattern can be distinguished.[83, 177] Glomeruloid growth cannot always be well discriminated from cribriform growth on two-dimensional slides. However, our three-dimensional reconstructions show that the glomerulations represent epithelial protrusions close to tubule splitting points, suggesting that the tubule splitting process might have failed at this point and caused cells to accumulate. This is in contrast to the epithelial proliferations present in the cribriform pattern. Moreover, we and others have found that the glomeruloid pattern had a lower proliferation rate than the cribriform growth pattern using KI67 immunohistochemistry (data not published), which could be another indication that it is not a cribriform variant.[179]

Lately, multiple prognostic studies have shown that cribriform growth is the most critical predictor for adverse outcome in prostate cancer patients, underpinning our finding that cribriform growth forms a separate architectural continuum.[84, 101, 102, 153, 180, 181] A natural consequence of these findings is that it is clinically most relevant to distinguish the patients with cribriform growth. This is especially true for patients presenting with Gleason score 3+4=7 on their prostate biopsy, since men without cribriform growth had comparable outcome to patients with Gleason score 3+3=6 prostate cancer. Therefore, even though these patients are diagnosed with Gleason score 3+4=7, it might not be necessary for them to undergo therapeutic intervention; instead they could enrol in active surveillance protocols.[57] In anticipation of this, our group has demonstrated the feasibility of a revised prostate cancer grading system, where the Gleason score and Grade group system is stratified by presence of cribriform growth. This proposed cGrade grading system outperformed the current grading system in predicting clinical outcome.[182] However, it remains important to remember that prostate biopsies are prone to sampling artefacts. This can lead to undersampling with subsequent potentially false cribriform negative prostate biopsies and undertreatment of some patients, as we have shown before.[183]

Gleason 5 grade includes multiple growth patterns, namely single cells, cords and solid fields with or without comedonecrosis. We found that the single-cells and cords patterns showed continuity with poorly-formed Gleason grade 4 glands. Additionally, we found that the solid Grade 5 pattern formed a continuum with cribriform Gleason grade 4 glands. Where cribriform growth is defined as an expansile area of cancer cells without interfering stroma and punched out lumens, solid growth is all that as well on HE sections, lacking only the lumens.[103, 184] As has been shown before, the proliferation rate is highest in the cribriform prostate cancer pattern, and this high proliferative activity is part of the aggressive nature of cribriform cancer.[179, 185] Since we have shown that cribriform and solid patterns are part of the same continuum, it can be hypothesised that the increasing amount of cells compress the lumens in the cribriform glands, subsequently forming solid sheets of cells. To further support this assumption, their molecular background should be investigated in the future.

Prostate cancer tubulogenesis

It has not yet been unravelled what mechanisms lie behind prostate cancer growth pattern development and how they contribute to tumour invasiveness.

Tumour branching by budding is the most commonly proposed model for glandular carcinomas and in 2011 Nagle *et al*. proposed a model for tumour budding in prostate cancer as alternative to the EMT model. [186-188] An important factor in carcinogenesis via tumour budding is the interaction between the tumour and the surrounding stromal cells.[189, 190] This is supported by recent studies showing that reciprocal interactions between stroma and prostate epithelium do not only control normal glandular growth but can also promote carcinogenesis. [191, 192] I*n vitro* and *in vivo* model systems show that co-culturing of prostate epithelial cells together with carcinoma-associated fibroblasts (CAF) or tumourigenic rat prostate mesenchymal cells stimulated progression of prostate cancer tumourigenesis.[193, 194] In addition, Richards *et al*. showed that *in vitro* co-cultures of prostate organoids with stromal cells maintained the budding potential of the organoids.[195]

Prostate cancer invasion via tumour branching could mirror embryonic tubulogenesis, directed by a complex system of polarity genes.[188] Tubulogenesis has been extensively studied, and several mechanisms by which tube formation takes place during and after embryonic development are unravelled.[186, 196] Tubulogenesis via cord hollowing is initiated by cells forming a lumen in a cord of cells due to polarization. A pre-apical patch is formed, and subsequently the polarity proteins switch places, inducing lumen formation.[197, 198] Unfortunately, the MDCK cell line is currently the only in vitro model in which the concept of tubulogenesis can be studied extensively.[199] Considering prostate cancer as dynamical continua, rather than individual growth patterns, we hypothesise that the first continuum follows the mechanism of cord hollowing through changes in polarity. Tumour cells invade via budding of cords Grade 5, which hollow to form poorly-formed glands and finally form Grade 3 glands, although this has not yet been investigated in *in-vitro* prostate cancer models. However, as it is currently impossible to follow prostate cancer growth patterns in time, novel *in vitro* or *in vivo* models should be developed to study the differentiation of growth patterns and their polarization.

Implementation of three-dimensional pathology

Imaging of intact FFPE tissues and subsequent three-dimensional reconstruction promises major advances in the field of pathology. However, there is still a long way to go before this technique could be implemented routinely and pathologists will be able to interpret these images as HE stained thin sections. Regular nuclear fluorescent stains such as DAPI or HOECHST excite at short wave lengths and are not able to emit their signal from thick tissue samples, and as a consequence they are not feasible for intact tissue imaging. Emission of fluorescent signal from thick tissue samples can be achieved using nuclear stains with higher wavelength, such as TO-PRO3 or sulforhodamine 101. After imaging, these fluorescent dyes can be pseudocoloured by algorithms to resemble standard HE stainings, to provide information about structures in deeper levels of the tissue.[200, 201] Glaser *et al*. used DRAQ5 and eosin stains for thick tissue imaging and was able visualise structures up to a depth of 320µm, subsequently pseudocoloured these images to resemble the HE stain.[202] In addition, they were able to use this staining on larger tissue samples to superficially visualise wide surface areas, enabling use of these stains for rapid assessment of tumour-margin surfaces. Combining these HE-like fluorescent stains with tissue clearing can provide pathologists with images suitable for diagnostic grading of superficial as well as deep volumetric images.

Where traditional histology is done using tissue sectioning, a major advantage of three-dimensional imaging is its non-destructive nature. Current pathology protocols on prostate biopsy demand HE sections on multiple levels to ensure correct interpretation of the tumour, leading to waste of patient tissue and losing the opportunity to study this tissue later using specific immunohistochemical stainings or molecular markers. Optical clearing offers the opportunity to study the complete prostate biopsy without physical sectioning.

However, even though these HE-like images can be interpreted more routinely by pathologists, implementation of three-dimensional imaging protocols is not easy. Several limitations arise, for example the need for robust and automated protocols with short processing times, the lack of cytological information on the final converted images and availability of pathologists trained for interpretation of these images. Routine tissue processing causes artefacts such as tissue shrinkage and dis-cohesive cancerous glands which might help the pathologists with their diagnosis. However, tissue processing for fluorescent in-depth imaging does not cause these artefacts, and thus the pathologist misses this information.[202] In addition, nucleoli and other cytological features necessary for accurate pathologic classification are not always as clearly visible in three-dimensional images as in routine HE stained tissues.

To successfully implement three-dimensional pathology in routine diagnostics, the HE-like images should have a high resolution. However, high resolution images are usually obtained using confocal microscopy, which is time consuming and not suitable for high-throughput protocols as used in the diagnostic field. In order to maintain a high throughput protocol, the scanning time should be limited, which can be achieved by using low resolution imaging. However, especially in difficult cases, the pathologist needs to use a high magnification and thus high resolution to confirm the suspected diagnosis, and low magnifications as used in large-area imaging for fast processing times do not provide this detail. This calls for technological development of microscopes able to produce fast, high resolution images compatible with solvent cleared tissues. On top of that, standardised algorithms should be developed to objectively quantify structures at a low resolution. This could be applied via for instance deep learning, however this is still under development.[203] Current two-dimensional digital pathology offers great potential for daily practise on regular thin slides, and the developments in that field might be applicable on three-dimensional images in the future.[90, 204]

Future perspectives

Three-dimensional imaging offers a wide range of options for further investigation of prostate cancer. In particular, areas with suspected transition between HGPIN or IDC-p and invasive cancer should be studied. In our study, we were limited by a small field of view and not capable of clear reconstruction of these areas. In addition, imaging of thick tissue samples using confocal microscopy proved time consuming. To enable high-throughput imaging, microscopes capable of three-dimensional imaging with a larger field of view and faster scanning times should be used, such as light sheet microscopes. For instance, Reder *et al*. previously showed the feasibility of this microscope for in depth imaging, using a water-based X-CLARITY optical clearing protocol.[205] However, the combination of organic clearing solvents and light sheet microscopy is still under development, since organic clearing solvents dissolve plastics and erode metals, thus excluding the use of standard objectives for these microscopes.

Application of fluorescent stainings combined with optical clearing also offers opportunities for other purposes. During resection of the prostate, it can be uncertain whether the surgical margins are free of tumour and currently this is determined on snap-frozen sections in some institutions. Using HE-like stainings, Glaser imaged large surface areas for the fast detection of positive surgical margins.[202] The non-destructive nature of optical clearing combined with large tissue volume imaging offers the opportunity to provide fast whole slide images whilst conserving tissue for further investigation. Recently, several studies confirmed the feasibility of this protocol in prostate and breast tissue using fluorescent HE-like stainings, however use of organic clearing solvent in these protocols is still under investigation.[201, 205, 206]

There are multiple challenges when implementing three-dimensional imaging in digital pathology and thus daily practise. For instance, the ability to store large data files, use of computers capable of handling large data files and user-friendly programs for three-dimensional renderings. At this moment, several applications can be used for digital pathology. For instance the Hamamatsu Nanozoomer, however this application is not designed to view Z-stacks generated with three-dimensional imaging. Currently, ImageJ and Amira are most frequently used for such renderings.[51] Unfortunately these programs require specialised training and are not feasible in daily diagnostic practice, and new, more user-friendly applications should be developed.

In our protocols, we have used the robust immunohistochemical markers Keratin 5 and Keratin 8/18, which mark the basal and luminal epithelial cells of the prostate. Visualising the expression of other proteins in prostate cancer would greatly enhance understanding of intra-tumoural heterogeneity, which plays an important part in tumour biology, progression and clinical outcome.[207] Therefore, other tissue or tumour specific stainings should also be applied in solvent based clearing protocols. For instance, three-dimensional analysis of the ETS-related gene (ERG), proliferation marker KI67 or other biological markers could improve understanding of prostate cancer biology.[208-211] Even though these markers are commonly used in routine FFPE immunohistochemistry, we have not been able to apply them using our protocol. Incorporation of antigen retrieval steps could enhance the feasibility of other protein markers, as well as directly labelled antibodies which can avoid multiple antibody incubation steps.

Conclusion

In this thesis, we have taken prostate cancer into a new dimension, showing that benign and malignant glands can easily be distinguished by their three-dimensional morphology. We proposed two continua consisting of multiple prostate cancer growth patterns based on novel insight in the three-dimensional morphology of prostate cancer in fixed patient samples. Implementation the acquired knowledge on three-dimensional pathology in daily practice will facilitate better interpretation of tumour growth patterns, leading to optimisation of prostate cancer diagnosis and tumour grading.

CHAPTER IX

Summary

SUMMARY

Since prostate cancer is the most common cancer in Western men, it is important to understand the histopathological features that form the basis of clinical decision making for the patient and their relation to disease outcome. Pathological reports of prostate cancer include, amongst other things, the individual and global Gleason scores and the tumour volume. In this thesis a broader view on these important parameters in two- and three-dimensions is presented. **Chapter I** provides a short introduction to the current parameters used in pathological grading of prostate cancer, as well as an overview of methods used for three-dimensional imaging and reconstruction of tissue samples. In **chapter II** we aimed to develop a method to image formalin-fixed, paraffin embedded tissues without physical sectioning. We show that fluorescent immunostaining in combination with optical clearing could be used to image prostate glandular structures up to a depth of 800 µm. Subsequently, the unsectioned tissue could still be used for molecular analysis and standard histological characterisation. Thus, this imaging technique provided the opportunity to study the mutual relationships of prostate growth patterns in 3D and the possibility to do subsequent molecular characterisation. **Chapter III** elaborates on the three-dimensional structures of benign and pre-cancerous epithelial lesions of the prostate, where we show that they are structurally different from prostate cancer. Although multiple lesions mimic prostate cancer on two-dimensional slides, only adenosis showed a three-dimensional tubular organisation similar to prostate cancer. In addition, we discovered a novel atrophic variant: Golgi-like atrophy, which presented with large elongated tubules parallel to the prostate surface. The three-dimensional structure of prostate cancer is described in **chapter IV**. There, we discovered a structural continuum between Gleason pattern 3 and glomeruloid, fused and poorly formed Gleason pattern 4, as well as a continuum between poorly formed Gleason pattern 4 and cords and single cells Gleason pattern 5. On the other hand, we showed that cribriform Gleason pattern 4 and solid Gleason pattern 5 formed a separate continuum. Taking into account the adverse nature of cribriform growth, it is important to identify patients with cribriform growth in an early stage. Therefore we have investigated the degree of undersampling of cribriform growth on prostate cancer biopsies, particularly in men with GS 3+4=7, as optimal treatment still under discussion for this subgroup. In **chapter V** we show that biopsies are false negative for cribriform growth in 52% of patients with cribriform growth on the radical prostatectomy. We did not find any predictive clinicopathological parameters for the presence of cribriform growth on the subsequent radical prostatectomy in these false negative subgroup. However, these patients had a better biochemical recurrence free survival rate than patients with true positive biopsies. The tumour multifocality and heterogeneity in a patient might result in a difference between the Gleason scores per individual biopsy core and the global Gleason score assigned. To

determine whether there are prognostic differences, we compared the outcome of patients with an overall Gleason score of 3 + 4 = 7 with and without presence of a higher individual Gleason score in **chapter VI**. We found that the patients with presence of a higher Gleason score had adverse clinicopathologic features such as elevated prostate specific antigen levels, more positive biopsies and more frequent cribriform and/or intraductal growth. However, the presence of a higher Gleason score on biopsy was not an independent predictor for biochemical recurrence free survival after radical prostatectomy or radiotherapy when standard clinical parameters were taken into account. Therefore, use of overall GS in clinical practice is justified to prevent overtreatment of these patients. In **chapter VII**, we investigated which tumour volume could best be reported in considering pathological and clinical outcome. Six well-defined parameters showed comparable prognostic value and could all be used in clinical practice. However, in case tumour quantification is a threshold for treatment decisions we recommend use of calculated tumour length, since it slightly outperformed the other parameters. Finally, in **chapter VIII** the main findings of this thesis are summarised and reviewed in the context of current knowledge. Here, I discuss the limitations of the different studies and potential clinical implications, as well as my thoughts on future research and implementation of our findings.

APPENDICES

Appendix I – Samenvatting

Omdat prostaatkanker de meest voorkomende vorm van kanker is in westerse mannen, is het belangrijk om de histopathologische karakteristieken te begrijpen welke de basis vormen van klinische beslisvorming voor de patiënt, en de relatie ervan met het verloop van de ziekte. In pathologie rapporten van prostaatkanker biopten staat onder andere de individuele en globale Gleason scores en het tumor volume. In dit proefschrift worden deze belangrijke factoren onderzocht in twee- en drie-dimensies. **Hoofdstuk I** geeft een korte introductie over de factoren die worden gebruikt binnen het pathologisch graderen van prostaatkanker, samen met een overzicht van methoden die gebruikt kunnen worden voor het maken van drie-dimensionale beelden en reconstructies. In **hoofdstuk II** streefden we naar het ontdekken van een methode om formaline gefixeerde, in paraffine ingebedde weefsels in drie dimensies te visualiseren zonder dat deze fysiek gesneden moeten worden. We laten zien dat een combinatie van fluorescente immuno-kleuring en het optisch doorzichtig maken van de weefsels gebruikt kon worden voor het zichtbaar maken van klierweefsel in de prostaat tot een diepte van 800 µm. Daarna kon het ongesneden weefsel nog gebruikt worden voor moleculaire analyse en gebruikelijke twee-dimensionale histologische karakterisatie. Zodoende geeft deze manier van beeldvorming de mogelijkheid om de groeipatronen in de prostaat in drie-dimensies te bestuderen met daarna de mogelijkheid tot moleculaire karakterisatie. **Hoofdstuk III** verdiept zich in de drie-dimensionale structuur van goedaardige epitheliale laesies en voorlopers van kanker in de prostaat, waarin we laten zien dat deze structureel verschillen van prostaatkanker. Hoewel deze laesies kunnen lijken op prostaatkanker op twee-dimensionale coupes, zagen we alleen bij adenose dezelfde tubulaire architectuur die ook aanwezig is in prostaatkanker. Daarbij hebben we ook een nieuwe atrofische variant ontdekt: Golgi-achtige atrofie, welke zich presenteerde met grote langgerekte buizen parallel aan de buitenkant van de prostaat. De drie-dimensionale structuur van prostaatkanker wordt beschreven in **hoofdstuk IV**. We ontdekten een structureel continuüm tussen Gleason patroon 3 en glomeruloid, gefuseerd en grillig Gleason patroon 4, in verbinding met een continuüm tussen grillig Gleason patroon 4 en strengen en losse cellen Gleason patroon 5. Aan de andere kan laten we zien dat cribriform Gleason patroon 4 en solide Gleason patroon 5 een apart tweede continuüm vormden. Omdat patiënten met cribriforme groei een slechte prognose hebben, is het belangrijk om deze patiënten in een vroeg stadium te kunnen diagnosticeren. Daarom hebben we onderzocht hoe vaak cribriforme groei wordt gemist in prostaat biopten, met name in mannen met GS 3+4= 7, omdat de optimale behandeling voor deze mannen nog steeds ter discussie staat. In **hoofdstuk V** laten we zien dat cribriforme groei wordt gemist in 52% van de patiënten met cribriform in hun daaropvolgende radicale prostatectomie. Daarbij vonden we geen klinisch pathologische karakteristieken die voorspellend waren voor de aanwezigheid van cribriforme groei op de radicale prostatectomie. Deze vals negatieve patiënten hebben echter wel een betere biochemisch-recidief vrije overleving dan patiënten met waar positieve biopten. Bij multifocale en heterogene tumoren kan het voorkomen dat er verschillen zijn tussen de Gleason score van individuele biopten en de globale Gleason score die wordt toegekend aan de patiënt. Daarom hebben we het ziekteverloop van patiënten met een globale Gleason score van 3+4=7 en wel of geen aanwezigheid van een hogere Gleason score op een individueel biopt met elkaar vergeleken in **hoofdstuk VI**. We hebben gevonden dat de patiënten met een hogere individuele Gleason score slechtere klinisch pathologische eigenschappen hadden, zoals een verhoogde waarde van het prostaat specifiek antigen in het bloed, meer positieve biopten en vaker aanwezigheid van cribriforme en/of intraductale groei dan patiënten zonder een hogere individuele Gleason score. Daarentegen was de aanwezigheid van een hogere Gleason score op een biopt geen onafhankelijke voorspeller voor biochemisch-recidief vrije overleving na een radicale prostatectomie of radiotherapie wanneer andere gebruikelijke klinische factoren ook meegenomen werden in de analyse. Daarom is het gebruik van de globale Gleason score in de kliniek gerechtvaardigd zodat overbehandeling van deze patiënten voorkomen wordt. In **hoofdstuk VII** onderzochten we welke tumor volume maat het beste gerapporteerd kan worden in relatie tot pathologische en klinisch verloop. Zes goed omschreven parameters lieten allen een vergelijkbare prognostische waarde zien en kunnen allen gebruikt worden in de kliniek. Echter, als tumor volume een grenswaarde is voor de beslisvorming van behandeling de patiënt raden wij aan om het gemeten tumor volume te gebruiken omdat deze een net iets betere voorspeller was dan de andere parameters. Tot slot vat ik de bevindingen van dit proefschrift samen in **hoofdstuk VIII** in de context van de huidige kennis. Hierin belicht ik de limitaties van de verschillende onderzoeken en mogelijke klinische toepassingen ervan, en mijn ideeën voor toekomstig onderzoek en de implementatie van onze bevindingen.

Appendix II – List of publications

Hollemans E, **Verhoef EI**, Bangma CH, Rietbergen J, Helleman J, Roobol MJ, van Leenders GJLH. *Clinicopathological characteristics of glomeruloid architecture in prostate cancer.* Modern Pathology, accepted January 2020.

Hollemans E, **Verhoef EI**, Bangma CH, Rietbergen J, Helleman J, Roobol MJ, van Leenders GJLH. *Clinical outcome comparison of Grade Group 1 and Grade Group 2 prostate cancer with and without cribriform architecture at radical prostatectomy*. Histopathology, in press 2020 Jan.

Verhoef EI, Kweldam CF, Kummerlin IP, Weng YC, Nieboer D, Bangma CH, Incrocci L, van der Kwast TH, Roobol MJ, van Leenders GJ. *Comparison of tumour volume parameters on prostate cancer biopsies.* Arch Path & Lab Med, 2020 Jan 6.

Hollemans E, **Verhoef EI**, Bangma CH, Rietbergen J, Helleman J, Roobol MJ, van Leenders GJLH. *Prostate carcinoma grade and length but not cribriform architecture at positive surgical margins are predictive for biochemical recurrence after radical prostatectomy.* American Journal of Surgical Pathology, 2019 Oct 4.

Hollemans E*, **Verhoef EI***, Bangma CH, Rietbergen J, Roobol MJ, Helleman J, van Leenders GJLH. *Concordance of cribriform architecture in matched prostate cancer biopsy and radical prostatectomy specimens.* Histopathology, 2019 Sep;75(3):338-345.

Doebar SC, Sieuwerts AM, **Verhoef EI**, de Weerd V, Martens JWM, van Deurzen CHM. *APOBEC3B gene expression in ductal carcinoma in situ and synchronous invasive breast cancer.* Cancers (Basel), 2019 Jul 27;11(8).

van Leenders GJ, Kweldam CF, Hollemans E**,** Kummerlin IP, Nieboer D, **Verhoef EI**, Remmers S, Incrocci L, Bangma CH, van der Kwast TH, Roobol MJ. *Improved prostate cancer biopsy grading by incorporation of invasive cribriform and intraductal carcinoma in the 2014 grade groups.* Eur Urol, 2019 Aug 19.

Duijvesz D, Rodriguez G, Hoogland AM, **Verhoef EI**, Dekker LJ, van Leenders GJLH, Luider TM, Jenster G. *Differential tissue expression of extracellular vesicle-derived proteins in prostate cancer.* The Prostate, 2019 Jun;79(9):1032-1042.

Agahozo MC, Sieuwerts AM, Doebar SC, **Verhoef EI**, Beaufort CM, Ruigrok-Ritstier K, de Weerd V, Sleddens HFBM, Dinjens WNM, Martens JWM, van Deurzen CHM. *PIK3CA mutations in ductal carcinoma and adjacent invasive breast cancer.* Endocr Relat Cancer, 2019 Mar 1.

Verhoef EI, van Cappellen WA, Slotman JA, Kremers G, Ewing-Graham PC, Houtsmuller AB, van Royen ME, van Leenders GJLH. *Three-dimensional architecture of common benign and pre-cancerous prostate epithelial lesions*. Histopathology, 2019 Jun;74(7):1036-1044

Verhoef EI, van Cappellen WA, Slotman JA, Kremers G, Ewing-Graham PC, Houtsmuller AB, van Royen ME, van Leenders GJLH. *Three-dimensional analysis reveals two major architectural subgroups of prostate cancer growth patterns*. Mod Pathol, 2019 Jul;32(7):1032-1041

Hollemans E, **Verhoef EI**, Bangma CH, Rietbergen J, Helleman J, Roobol MJ, van Leenders GJLH. *Large cribriform growth pattern identifies ISUP grade 2 prostate cancer patients at high risk for recurrence and metastasis.* Mod Pathol. 2019 Jan;32(1):139-146.

Rodriguez G, Zeneyedpour L, Duijvesz D, Hoogland AM, **Verhoef EI**, Kweldam CF, Burgers PC, Bangma CH, Jenster GW, van Leenders GJL, Luider TM. *Tissue proteomics outlines AGR2 AND LOX5 as markers for biochemical recurrence of prostate cancer.* Oncotarget. 2018 Nov 23;9(92):36444-36456.

Kolijn K, **Verhoef EI**, Smid M, Böttcher R, Jenster GW, Debets R, van Leenders GJ. *Epithelial-mesenchymal transition in human prostate cancer demonstrates enhanced immune evasion marked by IDO1 expression.* Cancer Res. 2018 Aug 15;78(16):4671-4679.

Mout L, de Wit R, Stuurman D**, Verhoef E**, Mathijssen R, de Ridder C, Lolkema M, van Weerden W. *Testosterone diminishes Cabazitaxel efficacy and intratumoural accumulation in a prostate cancer xenograft model.* EBioMedicine. 2018 Jan;27:182-186.

Verhoef EI, Kweldam CF, Kummerlin IP, Nieboer D, Bangma CH, Incrocci L, van der Kwast TH, Roobol MJ, van Leenders GJ. *Characteristics and outcome of prostate cancer patients with overall and highest Gleason score 3+4=7 at diagnostic biopsy.* Histopathology. 2018 Apr;72(5):760-765.

Chua MLK, Lo W, Pintilie M, Murgic J, Lalonde E, Bhandari V, Mahamud O, Gopalan A, Kweldam CF, van Leenders GJLH, **Verhoef EI**, Hoogland AM, Livingstone J, Berlin A, Dal Pra A, Meng A, Zhang J, Orain M, Picard V, Hovington H, Bergeron A, Lacombe L, Fradet Y, Têtu B, Reuter VE, Fleshner N, Fraser M, Boutros PC, van der Kwast TH, Bristow RG. *A Prostate Cancer "Nimbosus": Genomic Instability and SChLAP1 Dysregulation Underpin Aggression of Intraductal and Cribriform Subpathologies.* Eur Urol. 2017 Nov;72(5):665-674.

Zoni E, Chen L, Karkampouna S, Granchi Z, **Verhoef EI**, La Manna F, Kelber J, Pelger R, Henry M, Snaar-Jagalska E, van Leenders GJ, Beimers L, Kloen P, Gray P, van der Pluijm G, Kruithof- de Julio M. *CRIPTO and its signaling partner GRP78 drive the metastatic phenotype in human osteotropic prostate cancer*. Oncogene. 2017 Aug 17;36(33):4739-4749.

Van Royen ME*, **Verhoef EI***, Kweldam CF, van Cappellen WA, Kremers G, Houtsmuller AB, van Leenders GJ. *Three-dimensional microscopic analysis of clinical prostate cancer specimens*. Histopathology. 2016 Dec;69(6):985-992

Böttcher R, Dulla K, van Strijp D, Dits N, **Verhoef EI**, Baillie GS, van Leenders GJ, Houslay MD, Jenster G, Hoffman R. *Human PDE4D isoform composition is deregulated in primary prostate cancer and indicative for disease progression and development of distant metastases*. Oncotarget. 2016 Oct 25;7(43):70669-70684.

Kweldam CF, Kümmerlin IP, Nieboer D**, Verhoef EI**, Streyerberg E, Incrocci L, Bangma CH, van der Kwast T, Roobol MJ, van Leenders GJ. *Prostate cancer outcomes of men with biopsy Gleason score 6 and 7 without cribriform or intraductal carcinoma*. Eur J Cancer. 2016 Oct;66:26-33.

Hoogland AM, Böttcher R, **Verhoef E**, Jenster G, van Leenders GJ. *Gene-expression analysis of gleason grade 3 tumour glands embedded in low- and high-risk prostate cancer.* Oncotarget. 2016 Jun 21;7(25):37846-37856.

Kweldam CF, Kümmerlin IP, Nieboer D, **Verhoef EI**, Steyerberg EW, van der Kwast TH, Roobol MJ, van Leenders GJ. *Disease-specific survival of patients with invasive cribriform and intraductal prostate cancer at diagnostic biopsy*. Mod Pathol. 2016 Jun;29(6):630-6.

Verhoef EI, Kolijn K, de Herdt MJ, van der Steen B, Hoogland AM, Sleddens HF, Looijenga LH, van Leenders GJ. *MET expression during prostate cancer progression*. Oncotarget. 2016 May 24;7(21):31029-36.

De Herdt MJ, Willems SM, van der Steen B, Noorlag R, **Verhoef EI**, van Leenders GJ, van Es RJ, Koljenović S, Baatenburg de Jong RJ, Looijenga LH. *Absent and abundant MET immunoreactivity is associated with poor prognosis of patients with oral and oropharyngeal squamous cell carcinoma.* Oncotarget. 2016 Mar 15;7(11):13167-81.

Kolijn K, **Verhoef EI**, van Leenders GJ. *Morphological and immunohistochemical identification of epithelial-to-mesenchymal transition in clinical prostate cancer.* Oncotarget. 2015 Sep 15;6(27):24488-98.

Böttcher R, Hoogland AM, Dits N, **Verhoef EI**, Kweldam C, Waranecki P, Bangma CH, van Leenders GJ, Jenster G. *Novel long non-coding RNAs are specific diagnostic and prognostic markers for prostate cancer.* Oncotarget. 2015 Feb 28;6(6):4036-50.

Ghotra VP, He S, van der Horst G, Nijhoff S, de Bont H, Lekkerkerker A, Janssen R, Jenster G, van Leenders GJ, Hoogland AM, **Verhoef EI**, Baranski Z, Xiong J, van de Water B, van der Pluijm G, Snaar-Jagalska BE, Danen EH, *SYK is a candidate kinase target for the treatment of advanced prostate cancer.* Cancer Res. 2015 Jan 1;75(1):230-40.

Hoogland AM, **Verhoef EI**, Roobol MJ, Schröder FH, Wildhagen MF, van der Kwast TH, Henster G, van Leenders GJ, *Validation of stem cell markers in clinical prostate cancer: α6-integrin is predictive for non-agressive disease.* Prostate. 2014 May;74(5):488-96.

*These authors contributed equally to this paper

Appendix III – Curriculum Vitae

Esther Verhoef is geboren op 15 mei 1990 in Dordrecht. In 2008 slaagde zij voor het eindexamen van het VWO op het Stedelijk Dalton Lyceum te Dordrecht. Daarna begon zij aan de opleiding Biologie en Medische Laboratorium Wetenschappen aan de Hogeschool Rotterdam, waar zij in 2011 haar diploma behaalde. In augustus van dat jaar begon zij als research analist bij de afdeling pathologie binnen de onderzoeksgroep van dr. G.J.L.H. van Leenders. In mei 2016 is ze begonnen met haar promotie onderzoek binnen dezelfde groep. Naast het onderzoek dat ze doen was zij van 2016 tot 2018 medeoprichter en penningmeester van de stichting Hoeksche Waard Running Crew. Esther is momenteel woonachtig in Strijen met haar man en dochter.

Appendix IV – PhD portfolio

Name PhD student:	Esther I. Verhoef
Department:	Pathology
Research school:	Molecular Medicine
PhD period:	2016-2020
Promotor:	Prof. dr. F.J. van Kemenade
Copromotor:	Dr. G.J.L.H. van Leenders

	Year	Workload (ECTS)
Courses		
Biomedical Scientific English Writing	2015	2
Statistical package R	2016	1.8
Survival Analysis	2017	0.6
Molecular diagnostics	2017	1
Wetenschappelijke Integriteit	2017	0.3
BROK	2018	1.5
Presenting skills for junior researchers	2018	1
Personal leadership and communications	2018	1
Seminars and workshops		
20th Molecular Medicine day	2016	0.3
4th OIC AMIE symposium	2016	0.3
Annual PhD day	2017-2018	0.5
Erasmus MC Cancer Institute Research Day	2017	0.2
Career development for PhD candidates	2018	0.15
Oral presentations		
20th Molecular Medicine Day Best oral presentation award nominee	2016	1
Urology Research meetings	2016-2019	3
JNI meetings	2016-2019	3
Journal club	2017-2019	2
European Congress of Pathology	2018	1

(Inter)national conferences

20th Molecular Medicine day	2016	0.5
International Congress for Pathologists - Rotterdam	2017	0.5
International Congress for Pathologists - Bilbao	2018	1.5
EAU section of Urological Research - Athens	2018	2

Teaching and lecturing

Kimberley Kolijn	2016	1
Charlotte Kweldam	2016	1
Sarah Roshani	2016	1
Ying Weng	2017	0.5
Eva Hollemans	2017-2019	2
Ramona Jacobs	2019	1
VO digital microscopy	2016-2019	6

Appendix V – References

1. Adams J. The case of scirrhous of the prostate gland with corresponding affliction of the lymphatic glands in the lumbar region and in the pelvis. Lancet 1853;1:393.
2. Siegel RL, Miller KD, Jemal A. Cancer statistics, 2018. CA: a cancer journal for clinicians 2018;68(1);7-30.
3. van den Tweel JG, Taylor CR. A brief history of pathology: Preface to a forthcoming series that highlights milestones in the evolution of pathology as a discipline. Virchows Arch 2010;457(1);3-10.
4. Feldman AT, Wolfe D. Tissue processing and hematoxylin and eosin staining. Methods Mol Biol 2014;1180(31-43.
5. Okoye JO. Immunohistochemistry: A Revolutionary Technique in Laboratory Medicine. Clinical Medicine and Diagnostics 2015;5(4);60-69.
6. Gleason DF. Classification of prostatic carcinomas. Cancer Chemother Rep 1966;50(3);125-128.
7. Epstein JI. An update of the Gleason grading system. J Urol 2010;183(2);433-440.
8. Kim KH, Lim SK, Shin TY *et al.* Upgrading of Gleason score and prostate volume: a clinicopathological analysis. BJU Int 2013;111(8);1310-1316.
9. Kweldam CF, Kummerlin IP, Nieboer D *et al.* Disease-specific survival of patients with invasive cribriform and intraductal prostate cancer at diagnostic biopsy. Mod Pathol 2016;29(6);630-636.
10. Van der Kwast T, Al Daoud N, Collette L *et al.* Biopsy diagnosis of intraductal carcinoma is prognostic in intermediate and high risk prostate cancer patients treated by radiotherapy. Eur J Cancer 2012;48(9);1318-1325.
11. Amin M, Boccon-Gibod L, Egevad L *et al.* Prognostic and predictive factors and reporting of prostate carcinoma in prostate needle biopsy specimens. Scand J Urol Nephrol Suppl 2005216);20-33.
12. Hameed O, Humphrey PA. Immunohistochemistry in diagnostic surgical pathology of the prostate. Semin Diagn Pathol 2005;22(1);88-104.
13. van Leenders GJ, Boormans JL, Vissers CJ *et al.* Antibody EPR3864 is specific for ERG genomic fusions in prostate cancer: implications for pathological practice. Mod Pathol 2011;24(8);1128-1138.
14. Karram S, Trock BJ, Netto GJ *et al.* Should intervening benign tissue be included in the measurement of discontinuous foci of cancer on prostate needle biopsy? Correlation with radical prostatectomy findings. Am J Surg Pathol 2011;35(9);1351-1355.
15. Egawa S, Suyama K, Arai Y *et al.* Treatment outcome by risk group after radical prostatectomy in Japanese men. Int J Urol 2001;8(6);295-300.
16. King CR, Patel DA, Terris MK. Prostate biopsy volume indices do not predict for significant Gleason upgrading. Am J Clin Oncol 2005;28(2);125-129.
17. Cuzick J, Fisher G, Kattan MW *et al.* Long-term outcome among men with conservatively treated localised prostate cancer. Br J Cancer 2006;95(9);1186-1194.
18. Freedland SJ, Aronson WJ, Csathy GS *et al.* Comparison of percentage of total prostate needle biopsy tissue with cancer to percentage of cores with cancer for predicting PSA recurrence after radical prostatectomy: results from the SEARCH database. Urology 2003;61(4);742-747.
19. Salisbury JR, Whimster WF. Progress in computer-generated three-dimensional reconstruction. J Pathol 1993;170(3);223-227.
20. Huijsmans DP, Lamers WH, Los JA *et al.* Toward computerized morphometric facilities: a review of 58 software packages for computer-aided three-dimensional reconstruction, quantification, and picture generation from parallel serial sections. Anat Rec 1986;216(4);449-470.
21. Wang CW, Budiman Gosno E, Li YS. Fully automatic and robust 3D registration of serial-section microscopic images. Sci Rep 2015;5(15051.
22. Varnavas A, Carrell T, Penney G. Fully automated 2D-3D registration and verification. Med Image Anal 2015;26(1);108-119.
23. Wang Y, Chen S, Ni Y *et al.* Three-dimensional reconstruction with serial whole-mount sections of oral tongue squamous cell carcinoma: A preliminary study. J Oral Pathol Med 2018;47(1);53-59.

24. Schwier M, Bohler T, Hahn HK *et al.* Registration of histological whole slide images guided by vessel structures. J Pathol Inform 2013;4(Suppl);S10.
25. Moles Lopez X, Barbot P, Van Eycke YR *et al.* Registration of whole immunohistochemical slide images: an efficient way to characterize biomarker colocalization. J Am Med Inform Assoc 2015;22(1);86-99.
26. Benoit G, Cailleaux F, Quillard J *et al.* Computer assisted anatomical reconstruction: a prostate model. Surg Radiol Anat 1991;13(1);45-47.
27. Timms BG, Mohs TJ, Didio LJ. Ductal budding and branching patterns in the developing prostate. J Urol 1994;151(5);1427-1432.
28. Timms BG. Prostate development: a historical perspective. Differentiation 2008;76(6);565-577.
29. Kay PA, Robb RA, Bostwick DG. Prostate cancer microvessels: a novel method for three-dimensional reconstruction and analysis. Prostate 1998;37(4);270-277.
30. Boag AH, Kennedy LA, Miller MJ. Three-dimensional microscopic image reconstruction of prostatic adenocarcinoma. Arch Pathol Lab Med 2001;125(4);562-566.
31. Tolkach Y, Thomann S, Kristiansen G. 3D-reconstruction of prostate cancer architecture with serial immunohistochemical sections: hallmarks of tumour growth, tumour compartmentalization and implications for grading and heterogeneity. Histopathology 2018;72(6);1051-1059.
32. Spalteholz. Über das Durchsichtigmachen von menschlichen und tierischen Präparaten und seine theoretischen Bedingungen, nebst Anhang: Über Knochenfärbung. Leipzig: Hirzel, 1914.
33. Steinke H, Wolff W. A modified Spalteholz technique with preservation of the histology. Ann Anat 2001;183(1);91-95.
34. Chung K, Wallace J, Kim SY *et al.* Structural and molecular interrogation of intact biological systems. Nature 2013;497(7449);332-337.
35. Erturk A, Becker K, Jahrling N *et al.* Three-dimensional imaging of solvent-cleared organs using 3DISCO. Nat Protoc 2012;7(11);1983-1995.
36. Epstein JI, Egevad L, Amin MB *et al.* The 2014 International Society of Urological Pathology (ISUP) Consensus Conference on Gleason Grading of Prostatic Carcinoma: Definition of Grading Patterns and Proposal for a New Grading System. Am J Surg Pathol 2015.
37. Berney DM, Algaba F, Camparo P *et al.* The reasons behind variation in Gleason grading of prostatic biopsies: areas of agreement and misconception among 266 European pathologists. Histopathology 2014;64(3);405-411.
38. Rodriguez-Urrego PA, Cronin AM, Al-Ahmadie HA *et al.* Interobserver and intraobserver reproducibility in digital and routine microscopic assessment of prostate needle biopsies. Hum Pathol 2011;42(1);68-74.
39. Thomsen FB, Marcussen N, Berg KD *et al.* Repeated biopsies in patients with prostate cancer on active surveillance: clinical implications of interobserver variation in histopathological assessment. BJU Int 2015;115(4);599-605.
40. Booth ME, Treanor D, Roberts N *et al.* Three-dimensional reconstruction of ductal carcinoma in situ with virtual slides. Histopathology 2015;66(7);966-973.
41. Marchio C, Sapino A, Arisio R *et al.* A new vision of tubular and tubulo-lobular carcinomas of the breast, as revealed by 3-D modelling. Histopathology 2006;48(5);556-562.
42. Onozato ML, Klepeis VE, Yagi Y *et al.* A role of three-dimensional (3D)-reconstruction in the classification of lung adenocarcinoma. Anal Cell Pathol (Amst) 2012;35(2);79-84.
43. Zhou M, Li J, Cheng L *et al.* Diagnosis of "Poorly Formed Glands" Gleason Pattern 4 Prostatic Adenocarcinoma on Needle Biopsy: An Interobserver Reproducibility Study Among Urologic Pathologists With Recommendations. Am J Surg Pathol 2015;39(10);1331-1339.
44. Gibson E, Gaed M, Gomez JA *et al.* 3D prostate histology image reconstruction: Quantifying the impact of tissue deformation and histology section location. J Pathol Inform 2013;4(31.
45. Gibson E, Gaed M, Gomez JA *et al.* 3D prostate histology reconstruction: an evaluation of image-based and fiducial-based algorithms. Med Phys 2013;40(9);093501.
46. Hama H, Kurokawa H, Kawano H *et al.* Scale: a chemical approach for fluorescence imaging and reconstruction of transparent mouse brain. Nat Neurosci 2011;14(11);1481-1488.
47. Norton KA, Namazi S, Barnard N *et al.* Automated reconstruction algorithm for identification of 3D architectures of cribriform ductal carcinoma in situ. PLoS One 2012;7(9);e44011.
48. Sun L, Wang D, Zubovits JT *et al.* An improved processing method for breast whole-mount serial sections for three-dimensional histopathology imaging. Am J Clin Pathol 2009;131(3);383-392.

49. Renier N, Wu Z, Simon DJ *et al.* iDISCO: a simple, rapid method to immunolabel large tissue samples for volume imaging. Cell 2014;159(4);896-910.
50. Yokomizo T, Yamada-Inagawa T, Yzaguirre AD *et al.* Whole-mount three-dimensional imaging of internally localized immunostained cells within mouse embryos. Nat Protoc 2012;7(3);421-431.
51. Schindelin J, Arganda-Carreras I, Frise E *et al.* Fiji: an open-source platform for biological-image analysis. Nat Methods 2012;9(7);676-682.
52. Scott GD, Blum ED, Fryer AD *et al.* Tissue optical clearing, three-dimensional imaging, and computer morphometry in whole mouse lungs and human airways. Am J Respir Cell Mol Biol 2014;51(1);43-55.
53. Yang B, Treweek JB, Kulkarni RP *et al.* Single-cell phenotyping within transparent intact tissue through whole-body clearing. Cell 2014;158(4);945-958.
54. Okada H, Tsubura A, Okamura A *et al.* Keratin profiles in normal/hyperplastic prostates and prostate carcinoma. Virchows Arch A Pathol Anat Histopathol 1992;421(2);157-161.
55. van Leenders G, Dijkman H, Hulsbergen-van de Kaa C *et al.* Demonstration of intermediate cells during human prostate epithelial differentiation in situ and in vitro using triple-staining confocal scanning microscopy. Lab Invest 2000;80(8);1251-1258.
56. Torres R, Vesuna S, Levene MJ. High-resolution, 2- and 3-dimensional imaging of uncut, unembedded tissue biopsy samples. Arch Pathol Lab Med 2014;138(3);395-402.
57. Dall'Era MA, Albertsen PC, Bangma C *et al.* Active surveillance for prostate cancer: a systematic review of the literature. Eur Urol 2012;62(6);976-983.
58. Boran C, Kandirali E, Yilmaz F *et al.* Reliability of the 34betaE12, keratin 5/6, p63, bcl-2, and AMACR in the diagnosis of prostate carcinoma. Urologic oncology 2011;29(6);614-623.
59. Dabir PD, Ottosen P, Hoyer S *et al.* Comparative analysis of three- and two-antibody cocktails to AMACR and basal cell markers for the immunohistochemical diagnosis of prostate carcinoma. Diagn Pathol 2012;7(81.
60. Martens MB, Keller JH. Routine immunohistochemical staining for high-molecular weight cytokeratin 34-beta and alpha-methylacyl CoA racemase (P504S) in postirradiation prostate biopsies. Mod Pathol 2006;19(2);287-290.
61. Molinie V, Herve JM, Lugagne PM *et al.* Diagnostic utility of a p63/alpha-methyl coenzyme A racemase (p504s) cocktail in ambiguous lesions of the prostate upon needle biopsy. BJU Int 2006;97(5);1109-1115.
62. Shah RB, Zhou M, LeBlanc M *et al.* Comparison of the basal cell-specific markers, 34betaE12 and p63, in the diagnosis of prostate cancer. Am J Surg Pathol 2002;26(9);1161-1168.
63. Kowalewski A, Szylberg L, Skorczewska A *et al.* Diagnostic Difficulties With Atrophy, Atypical Adenomatous Hyperplasia, and Atypical Small Acinar Proliferation: A Systematic Review of Current Literature. Clin Genitourin Cancer 2016;14(5);361-365.
64. Zhou M. High-grade prostatic intraepithelial neoplasia, PIN-like carcinoma, ductal carcinoma, and intraductal carcinoma of the prostate. Mod Pathol 2018;31(S1);S71-79.
65. Herawi M, Parwani AV, Irie J *et al.* Small glandular proliferations on needle biopsies: most common benign mimickers of prostatic adenocarcinoma sent in for expert second opinion. Am J Surg Pathol 2005;29(7);874-880.
66. Al Diffalha S, Shaar M, Barkan GA *et al.* Immunohistochemistry in the workup of prostate biopsies: Frequency, variation and appropriateness of use among pathologists practicing at an academic center. Ann Diagn Pathol 2017;27(34-42.
67. van Royen ME, Verhoef EI, Kweldam CF *et al.* Three-dimensional microscopic analysis of clinical prostate specimens. Histopathology 2016;69(6);985-992.
68. De Marzo AM, Platz EA, Epstein JI *et al.* A working group classification of focal prostate atrophy lesions. Am J Surg Pathol 2006;30(10);1281-1291.
69. Verhoef EI, van Cappellen WA, Slotman JA *et al.* Three-dimensional analysis reveals two major architectural subgroups of prostate cancer growth patterns. Mod Pathol 2019.
70. Berney DM, Fisher G, Kattan MW *et al.* Pitfalls in the diagnosis of prostatic cancer: retrospective review of 1791 cases with clinical outcome. Histopathology 2007;51(4);452-457.
71. Epstein JI. Diagnosis of limited adenocarcinoma of the prostate. Histopathology 2012;60(1);28-40.
72. Netto GJ, Epstein JI. Benign Mimickers of Prostate Adenocarcinoma on Needle Biopsy and Transurethral Resection. Surg Pathol Clin 2008;1(1);1-41.

73. Helpap B. Differential diagnosis of glandular proliferations in the prostate. A conventional and immunohistochemical approach. Virchows Arch 1998;433(5);397-405.
74. Srigley JR. Benign mimickers of prostatic adenocarcinoma. Mod Pathol 2004;17(3);328-348.
75. Bettendorf O, Schmidt H, Eltze E *et al.* Cytogenetic changes and loss of heterozygosity in atypical adenomatous hyperplasia, in carcinoma of the prostate and in non-neoplastic prostate tissue using comparative genomic hybridization and multiplex-PCR. Int J Oncol 2005;26(1);267-274.
76. Doll JA, Zhu X, Furman J *et al.* Genetic analysis of prostatic atypical adenomatous hyperplasia (adenosis). Am J Pathol 1999;155(3);967-971.
77. Cheng L, Davidson DD, Maclennan GT *et al.* Atypical adenomatous hyperplasia of prostate lacks TMPRSS2-ERG gene fusion. Am J Surg Pathol 2013;37(10);1550-1554.
78. Green WM, Hicks JL, De Marzo A *et al.* Immunohistochemical evaluation of TMPRSS2-ERG gene fusion in adenosis of the prostate. Hum Pathol 2013;44(9);1895-1901.
79. Gleason DF, Mellinger GT. Prediction of prognosis for prostatic adenocarcinoma by combined histological grading and clinical staging. J Urol 1974;111(1);58-64.
80. Epstein JI. Gleason score 2-4 adenocarcinoma of the prostate on needle biopsy: a diagnosis that should not be made. Am J Surg Pathol 2000;24(4);477-478.
81. Choy B, Pearce SM, Anderson BB *et al.* Prognostic Significance of Percentage and Architectural Types of Contemporary Gleason Pattern 4 Prostate Cancer in Radical Prostatectomy. Am J Surg Pathol 2016;40(10);1400-1406.
82. Dong F, Yang P, Wang C *et al.* Architectural heterogeneity and cribriform pattern predict adverse clinical outcome for Gleason grade 4 prostatic adenocarcinoma. Am J Surg Pathol 2013;37(12);1855-1861.
83. Kweldam CF, Kummerlin IP, Nieboer D *et al.* Prostate cancer outcomes of men with biopsy Gleason score 6 and 7 without cribriform or intraductal carcinoma. Eur J Cancer 2016;66(26-33.
84. Kweldam CF, Wildhagen MF, Steyerberg EW *et al.* Cribriform growth is highly predictive for postoperative metastasis and disease-specific death in Gleason score 7 prostate cancer. Mod Pathol 2015;28(3);457-464.
85. Al Nemer AM, Elsharkawy T, Elshawarby M *et al.* The updated grading system of prostate carcinoma: an inter-observer agreement study among general pathologists in an academic practice. APMIS 2017;125(11);957-961.
86. Egevad L, Delahunt B, Berney DM *et al.* Utility of Pathology Imagebase for Standardization of Prostate Cancer Grading. Histopathology 2018;73(1);8-18.
87. Kweldam CF, Nieboer D, Algaba F *et al.* Gleason grade 4 prostate adenocarcinoma patterns: an interobserver agreement study among genitourinary pathologists. Histopathology 2016;69(3);441-449.
88. Egevad L, Ahmad AS, Algaba F *et al.* Standardization of Gleason grading among 337 European pathologists. Histopathology 2013;62(2);247-256.
89. Erturk A, Lafkas D, Chalouni C. Imaging cleared intact biological systems at a cellular level by 3DISCO. J Vis Exp 2014;(89)(89).
90. Singh M, Kalaw EM, Giron DM *et al.* Gland segmentation in prostate histopathological images. J Med Imaging (Bellingham) 2017;4(2);027501.
91. Shah RB, Li J, Cheng L *et al.* Diagnosis of Gleason pattern 5 prostate adenocarcinoma on core needle biopsy: an interobserver reproducibility study among urologic pathologists. Am J Surg Pathol 2015;39(9);1242-1249.
92. Lotan TL, Epstein JI. Gleason grading of prostatic adenocarcinoma with glomeruloid features on needle biopsy. Hum Pathol 2009;40(4);471-477.
93. Hannezo E, Scheele C, Moad M *et al.* A Unifying Theory of Branching Morphogenesis. Cell 2017;171(1);242-255 e227.
94. Bottcher R, Kweldam CF, Livingstone J *et al.* Cribriform and intraductal prostate cancer are associated with increased genomic instability and distinct genomic alterations. BMC Cancer 2018;18(1);8.
95. Chua MLK, Lo W, Pintilie M *et al.* A Prostate Cancer "Nimbosus": Genomic Instability and SChLAP1 Dysregulation Underpin Aggression of Intraductal and Cribriform Subpathologies. Eur Urol 2017;72(5);665-674.

96. Williams JL, Greer PA, Squire JA. Recurrent copy number alterations in prostate cancer: an in silico meta-analysis of publicly available genomic data. Cancer Genet 2014;207(10-12);474-488.
97. Humphrey PA. Variants of acinar adenocarcinoma of the prostate mimicking benign conditions. Mod Pathol 2018;31(S1);S64-70.
98. McKenney JK, Wei W, Hawley S *et al.* Histologic Grading of Prostatic Adenocarcinoma Can Be Further Optimized: Analysis of the Relative Prognostic Strength of Individual Architectural Patterns in 1275 Patients From the Canary Retrospective Cohort. Am J Surg Pathol 2016;40(11);1439-1456.
99. Kir G, Sarbay BC, Gumus E *et al.* The association of the cribriform pattern with outcome for prostatic adenocarcinomas. Pathol Res Pract 2014;210(10);640-644.
100. Truong M, Frye T, Messing E *et al.* Historical and contemporary perspectives on cribriform morphology in prostate cancer. Nat Rev Urol 2018;15(8);475-482.
101. Hollemans E, Verhoef EI, Bangma CH *et al.* Large cribriform growth pattern identifies ISUP grade 2 prostate cancer at high risk for recurrence and metastasis. Mod Pathol 2019;32(1);139-146.
102. Kweldam CF, Kummerlin IP, Nieboer D *et al.* Presence of invasive cribriform or intraductal growth at biopsy outperforms percentage grade 4 in predicting outcome of Gleason score 3+4=7 prostate cancer. Mod Pathol 2017;30(8);1126-1132.
103. Trudel D, Downes MR, Sykes J *et al.* Prognostic impact of intraductal carcinoma and large cribriform carcinoma architecture after prostatectomy in a contemporary cohort. Eur J Cancer 2014;50(9);1610-1616.
104. Sauter G, Steurer S, Clauditz TS *et al.* Clinical Utility of Quantitative Gleason Grading in Prostate Biopsies and Prostatectomy Specimens. Eur Urol 2016;69(4);592-598.
105. Corcoran NM, Hovens CM, Hong MK *et al.* Underestimation of Gleason score at prostate biopsy reflects sampling error in lower volume tumours. BJU Int 2012;109(5);660-664.
106. Weinreb JC, Barentsz JO, Choyke PL *et al.* PI-RADS Prostate Imaging - Reporting and Data System: 2015, Version 2. Eur Urol 2016;69(1);16-40.
107. Buyyounouski MK, Choyke PL, McKenney JK *et al.* Prostate cancer - major changes in the American Joint Committee on Cancer eighth edition cancer staging manual. CA: a cancer journal for clinicians 2017;67(3);245-253.
108. Corcoran NM, Hong MK, Casey RG *et al.* Upgrade in Gleason score between prostate biopsies and pathology following radical prostatectomy significantly impacts upon the risk of biochemical recurrence. BJU Int 2011;108(8 Pt 2);E202-210.
109. Epstein JI, Feng Z, Trock BJ *et al.* Upgrading and downgrading of prostate cancer from biopsy to radical prostatectomy: incidence and predictive factors using the modified Gleason grading system and factoring in tertiary grades. Eur Urol 2012;61(5);1019-1024.
110. Masoomian M, Downes MR, Sweet J *et al.* Concordance of biopsy and prostatectomy diagnosis of intraductal and cribriform carcinoma in a prospectively collected data set. Histopathology 2019;74(3);474-482.
111. Amin MB, Lin DW, Gore JL *et al.* The critical role of the pathologist in determining eligibility for active surveillance as a management option in patients with prostate cancer: consensus statement with recommendations supported by the College of American Pathologists, International Society of Urological Pathology, Association of Directors of Anatomic and Surgical Pathology, the New Zealand Society of Pathologists, and the Prostate Cancer Foundation. Arch Pathol Lab Med 2014;138(10);1387-1405.
112. Montironi R, Hammond EH, Lin DW *et al.* Consensus statement with recommendations on active surveillance inclusion criteria and definition of progression in men with localized prostate cancer: the critical role of the pathologist. Virchows Arch 2014;465(6);623-628.
113. Truong M, Feng C, Hollenberg G *et al.* A Comprehensive Analysis of Cribriform Morphology on Magnetic Resonance Imaging/Ultrasound Fusion Biopsy Correlated with Radical Prostatectomy Specimens. J Urol 2018;199(1);106-113.
114. Prendeville S, Gertner M, Maganti M *et al.* Role of Magnetic Resonance Imaging Targeted Biopsy in Detection of Prostate Cancer Harboring Adverse Pathological Features of Intraductal Carcinoma and Invasive Cribriform Carcinoma. J Urol 2018;200(1);104-113.
115. Moch H, Humphrey PA, Ulbright TM *et al.* *WHO Classification of Tumours of the Urinary System and Male Genital Organs*. 4th revised edition. ed. Lyon, France: IARC Press, 2016.

116. Simpkin AJ, Tilling K, Martin RM *et al.* Systematic Review and Meta-analysis of Factors Determining Change to Radical Treatment in Active Surveillance for Localized Prostate Cancer. Eur Urol 2015;67(6);993-1005.
117. Berney DM, Beltran L, Fisher G *et al.* Validation of a contemporary prostate cancer grading system using prostate cancer death as outcome. Br J Cancer 2016;114(10);1078-1083.
118. Kunz GM, Jr., Epstein JI. Should each core with prostate cancer be assigned a separate gleason score? Hum Pathol 2003;34(9);911-914.
119. Poulos CK, Daggy JK, Cheng L. Preoperative prediction of Gleason grade in radical prostatectomy specimens: the influence of different Gleason grades from multiple positive biopsy sites. Mod Pathol 2005;18(2);228-234.
120. Tolonen TT, Kujala PM, Tammela TL *et al.* Overall and worst gleason scores are equally good predictors of prostate cancer progression. BMC Urol 2011;11(21.
121. Roobol MJ, Schroder FH. European Randomized Study of Screening for Prostate Cancer: achievements and presentation. BJU Int 2003;92 Suppl 2(117-122.
122. Schroder FH, Hugosson J, Roobol MJ *et al.* Screening and prostate-cancer mortality in a randomized European study. N Engl J Med 2009;360(13);1320-1328.
123. Aus G, Abbou CC, Bolla M *et al.* EAU guidelines on prostate cancer. Eur Urol 2005;48(4);546-551.
124. Roach M, 3rd, Hanks G, Thames H, Jr. *et al.* Defining biochemical failure following radiotherapy with or without hormonal therapy in men with clinically localized prostate cancer: recommendations of the RTOG-ASTRO Phoenix Consensus Conference. Int J Radiat Oncol Biol Phys 2006;65(4);965-974.
125. De Koning HJ, Blom J, Merkelbach JW *et al.* Determining the cause of death in randomized screening trial(s) for prostate cancer. BJU Int 2003;92 Suppl 2(71-78.
126. Algaba F, Montironi R. Impact of prostate cancer multifocality on its biology and treatment. J Endourol 2010;24(5);799-804.
127. Andreoiu M, Cheng L. Multifocal prostate cancer: biologic, prognostic, and therapeutic implications. Hum Pathol 2010;41(6);781-793.
128. Muezzinoglu A. Clinicopathologic significance of multifocal prostate cancer. Lab Invest 2006;[Abstract](86);p. 151A.
129. Chen RC, Rumble RB, Loblaw DA *et al.* Active Surveillance for the Management of Localized Prostate Cancer (Cancer Care Ontario Guideline): American Society of Clinical Oncology Clinical Practice Guideline Endorsement. J Clin Oncol 2016;34(18);2182-2190.
130. Morash C, Tey R, Agbassi C *et al.* Active surveillance for the management of localized prostate cancer: Guideline recommendations. Canadian Urological Association journal = Journal de l'Association des urologues du Canada 2015;9(5-6);171-178.
131. Scattoni V, Zlotta A, Montironi R *et al.* Extended and saturation prostatic biopsy in the diagnosis and characterisation of prostate cancer: a critical analysis of the literature. Eur Urol 2007;52(5);1309-1322.
132. Egevad L, Allsbrook WC, Jr., Epstein JI. Current practice of diagnosis and reporting of prostate cancer on needle biopsy among genitourinary pathologists. Hum Pathol 2006;37(3);292-297.
133. Humphrey PA, Moch H, Cubilla AL *et al.* The 2016 WHO Classification of Tumours of the Urinary System and Male Genital Organs-Part B: Prostate and Bladder Tumours. Eur Urol 2016;70(1);106-119.
134. Srigley JR, Humphrey PA, Amin MB *et al.* Protocol for the examination of specimens from patients with carcinoma of the prostate gland. Arch Pathol Lab Med 2009;133(10);1568-1576.
135. Harnden P, Shelley MD, Naylor B *et al.* Does the extent of carcinoma in prostatic biopsies predict prostate-specific antigen recurrence? A systematic review. Eur Urol 2008;54(4);728-739.
136. Iremashvili V, Burdick-Will J, Soloway MS. Improving risk stratification in patients with prostate cancer managed by active surveillance: a nomogram predicting the risk of biopsy progression. BJU Int 2013;112(1);39-44.
137. Arias-Stella JA, 3rd, Varma KR, Montoya-Cerrillo D *et al.* Does discontinuous involvement of a prostatic needle biopsy core by adenocarcinoma correlate with a large tumor focus at radical prostatectomy? Am J Surg Pathol 2015;39(2);281-286.
138. Tosoian JJ, Mamawala M, Epstein JI *et al.* Intermediate and Longer-Term Outcomes From a Prospective Active-Surveillance Program for Favorable-Risk Prostate Cancer. J Clin Oncol 2015;33(30);3379-3385.

139. van den Bergh RC, Roemeling S, Roobol MJ *et al.* Prospective validation of active surveillance in prostate cancer: the PRIAS study. Eur Urol 2007;52(6);1560-1563.

140. Cheney MD, Chen MH, Zhang D *et al.* Greatest percentage of involved core length and the risk of death from prostate cancer in men with highest Gleason score >/= 7. Clin Genitourin Cancer 2014;12(4);234-240.

141. Cheney MD, Zhang D, Chen MH *et al.* Greatest Percentage Involved Core Length and Risk of Clinically Significant Prostate-Specific Antigen Failure After Radical Prostatectomy. Clin Genitourin Cancer 2015;13(4);338-343.

142. Freedland SJ, Csathy GS, Dorey F *et al.* Clinical utility of percent prostate needle biopsy tissue with cancer cutpoints to risk stratify patients before radical prostatectomy. Urology 2002;60(1);84-88.

143. Gretzer MB, Epstein JI, Pound CR *et al.* Substratification of stage T1C prostate cancer based on the probability of biochemical recurrence. Urology 2002;60(6);1034-1039.

144. Heidenreich A, Bellmunt J, Bolla M *et al.* EAU guidelines on prostate cancer. Part 1: screening, diagnosis, and treatment of clinically localised disease. Eur Urol 2011;59(1);61-71.

145. Linson PW, Lee AK, Doytchinova T *et al.* Percentage of core lengths involved with prostate cancer: does it add to the percentage of positive prostate biopsies in predicting postoperative prostate-specific antigen outcome for men with intermediate-risk prostate cancer? Urology 2002;59(5);704-708.

146. Noguchi M, Stamey TA, McNeal JE *et al.* Relationship between systematic biopsies and histological features of 222 radical prostatectomy specimens: lack of prediction of tumor significance for men with nonpalpable prostate cancer. J Urol 2001;166(1);104-109; discussion 109-110.

147. Royston P, Altman DG, Sauerbrei W. Dichotomizing continuous predictors in multiple regression: a bad idea. Stat Med 2006;25(1);127-141.

148. Chopra S, Toi A, Taback N *et al.* Pathological predictors for site of local recurrence after radiotherapy for prostate cancer. Int J Radiat Oncol Biol Phys 2012;82(3);e441-448.

149. D'Amico AV, Schultz D, Silver B *et al.* The clinical utility of the percent of positive prostate biopsies in predicting biochemical outcome following external-beam radiation therapy for patients with clinically localized prostate cancer. Int J Radiat Oncol Biol Phys 2001;49(3);679-684.

150. Spratt DE, Zumsteg Z, Ghadjar P *et al.* Prognostic importance of Gleason 7 disease among patients treated with external beam radiation therapy for prostate cancer: results of a detailed biopsy core analysis. Int J Radiat Oncol Biol Phys 2013;85(5);1254-1261.

151. Brimo F, Vollmer RT, Corcos J *et al.* Prognostic value of various morphometric measurements of tumour extent in prostate needle core tissue. Histopathology 2008;53(2);177-183.

152. Epstein JI, Allsbrook WC, Jr., Amin MB *et al.* The 2005 International Society of Urological Pathology (ISUP) Consensus Conference on Gleason Grading of Prostatic Carcinoma. Am J Surg Pathol 2005;29(9);1228-1242.

153. Epstein JI, Egevad L, Amin MB *et al.* The 2014 International Society of Urological Pathology (ISUP) Consensus Conference on Gleason Grading of Prostatic Carcinoma: Definition of Grading Patterns and Proposal for a New Grading System. Am J Surg Pathol 2016;40(2);244-252.

154. Hassan O, Matoso A. Clinical significance of subtypes of Gleason pattern 4 prostate cancer. Transl Androl Urol 2018;7(Suppl 4);S477-S483.

155. McKenney JK, Simko J, Bonham M *et al.* The potential impact of reproducibility of Gleason grading in men with early stage prostate cancer managed by active surveillance: a multi-institutional study. J Urol 2011;186(2);465-469.

156. Humphrey PA. Complete histologic serial sectioning of a prostate gland with adenocarcinoma. Am J Surg Pathol 1993;17(5);468-472.

157. Malandain G, Bardinet E, Nelissen K *et al.* Fusion of autoradiographs with an MR volume using 2-D and 3-D linear transformations. Neuroimage 2004;23(1);111-127.

158. Richardson DS, Lichtman JW. Clarifying Tissue Clearing. Cell 2015;162(2);246-257.

159. Verhoef EI, van Cappellen WA, Slotman JA *et al.* Three-dimensional architecture of common benign and precancerous prostate epithelial lesions. Histopathology 2019;74(7);1036-1044.

160. Bostwick DG, Srigley J, Grignon D *et al.* Atypical adenomatous hyperplasia of the prostate: morphologic criteria for its distinction from well-differentiated carcinoma. Hum Pathol 1993;24(8);819-832.

161. Epstein JI. Adenosis (atypical adenomatous hyperplasia): histopathology and relationship to carcinoma. Pathol Res Pract 1995;191(9);888-898.

162. Beltran L, Ahmad AS, Sandu H *et al.* Histopathologic False-positive Diagnoses of Prostate Cancer in the Age of Immunohistochemistry. Am J Surg Pathol 2019;43(3);361-368.

163. Cheng L, Shan A, Cheville JC *et al.* Atypical adenomatous hyperplasia of the prostate: a premalignant lesion? Cancer Res 1998;58(3);389-391.

164. Bostwick DG, Qian J. Atypical adenomatous hyperplasia of the prostate. Relationship with carcinoma in 217 whole-mount radical prostatectomies. Am J Surg Pathol 1995;19(5);506-518.

165. Calvo A, Xiao N, Kang J *et al.* Alterations in gene expression profiles during prostate cancer progression: functional correlations to tumorigenicity and down-regulation of selenoprotein-P in mouse and human tumors. Cancer Res 2002;62(18);5325-5335.

166. Putzi MJ, De Marzo AM. Morphologic transitions between proliferative inflammatory atrophy and high-grade prostatic intraepithelial neoplasia. Urology 2000;56(5);828-832.

167. Wang W, Bergh A, Damber JE. Morphological transition of proliferative inflammatory atrophy to high-grade intraepithelial neoplasia and cancer in human prostate. Prostate 2009;69(13);1378-1386.

168. Trabzonlu L, Kulac I, Zheng Q *et al.* Molecular Pathology of High-Grade Prostatic Intraepithelial Neoplasia: Challenges and Opportunities. Cold Spring Harb Perspect Med 2019;9(4).

169. Kovi J, Jackson MA, Heshmat MY. Ductal spread in prostatic carcinoma. Cancer 1985;56(7);1566-1573.

170. McNeal JE, Yemoto CE. Spread of adenocarcinoma within prostatic ducts and acini. Morphologic and clinical correlations. Am J Surg Pathol 1996;20(7);802-814.

171. Miyai K, Divatia MK, Shen SS *et al.* Heterogeneous clinicopathological features of intraductal carcinoma of the prostate: a comparison between "precursor-like" and "regular type" lesions. Int J Clin Exp Pathol 2014;7(5);2518-2526.

172. Robinson BD, Epstein JI. Intraductal carcinoma of the prostate without invasive carcinoma on needle biopsy: emphasis on radical prostatectomy findings. J Urol 2010;184(4);1328-1333.

173. Dawkins HJ, Sellner LN, Turbett GR *et al.* Distinction between intraductal carcinoma of the prostate (IDC-P), high-grade dysplasia (PIN), and invasive prostatic adenocarcinoma, using molecular markers of cancer progression. Prostate 2000;44(4);265-270.

174. Cohen RJ, Wheeler TM, Bonkhoff H *et al.* A proposal on the identification, histologic reporting, and implications of intraductal prostatic carcinoma. Arch Pathol Lab Med 2007;131(7);1103-1109.

175. Verhoef EI, van Cappellen WA, Slotman JA *et al.* Three-dimensional analysis reveals two major architectural subgroups of prostate cancer growth patterns. Mod Pathol 2019;32(7);1032-1041.

176. Iczkowski KA, Torkko KC, Kotnis GR *et al.* Digital quantification of five high-grade prostate cancer patterns, including the cribriform pattern, and their association with adverse outcome. Am J Clin Pathol 2011;136(1);98-107.

177. Hollemans E. Clinical outcome comparison of Grade Group 1 and cribriform-negative Grade Group 2 prostate cancer at radical prostatectomy. Histopathology 2019.

178. Lindberg J, Kristiansen A, Wiklund P *et al.* Tracking the origin of metastatic prostate cancer. Eur Urol 2015;67(5);819-822.

179. Fu L, Hwang M, Adeniran AJ *et al.* Proliferation index of different Gleason pattern 4 histomorphologies and associated pattern 3 adenocarcinoma of the prostate. Hum Pathol 2017;70(1-5.

180. Flood TA, Schieda N, Sim J *et al.* Evaluation of tumor morphologies and association with biochemical recurrence after radical prostatectomy in grade group 5 prostate cancer. Virchows Arch 2018;472(2);205-212.

181. Sarbay BC, Kir G, Topal CS *et al.* Significance of the cribriform pattern in prostatic adenocarcinomas. Pathol Res Pract 2014;210(9);554-557.

182. van Leenders G, Kweldam CF, Hollemans E *et al.* Improved Prostate Cancer Biopsy Grading by Incorporation of Invasive Cribriform and Intraductal Carcinoma in the 2014 Grade Groups. Eur Urol 2019.

183. Hollemans E, Verhoef EI, Bangma CH *et al.* Concordance of cribriform architecture in matched prostate cancer biopsy and radical prostatectomy specimens. Histopathology 2019;75(3);338-345.

184. Kweldam CF, van der Kwast T, van Leenders GJ. On cribriform prostate cancer. Transl Androl Urol 2018;7(1);145-154.

185. Gallee MP, Visser-de Jong E, ten Kate FJ *et al.* Monoclonal antibody Ki-67 defined growth fraction in benign prostatic hyperplasia and prostatic cancer. J Urol 1989;142(5);1342-1346.
186. Andrew DJ, Ewald AJ. Morphogenesis of epithelial tubes: Insights into tube formation, elongation, and elaboration. Dev Biol 2010;341(1);34-55.
187. Bronsert P, Enderle-Ammour K, Bader M *et al.* Cancer cell invasion and EMT marker expression: a three-dimensional study of the human cancer-host interface. J Pathol 2014;234(3);410-422.
188. Nagle RB, Cress AE. Metastasis Update: Human Prostate Carcinoma Invasion via Tubulogenesis. Prostate Cancer 2011;2011(249290.
189. Bosman FT, de Bruine A, Flohil C *et al.* Epithelial-stromal interactions in colon cancer. Int J Dev Biol 1993;37(1);203-211.
190. Seljelid R, Jozefowski S, Sveinbjornsson B. Tumor stroma. Anticancer Res 1999;19(6A);4809-4822.
191. Cunha GR, Hayward SW, Wang YZ *et al.* Role of the stromal microenvironment in carcinogenesis of the prostate. Int J Cancer 2003;107(1);1-10.
192. Niu YN, Xia SJ. Stroma-epithelium crosstalk in prostate cancer. Asian J Androl 2009;11(1);28-35.
193. Giannoni E, Taddei ML, Morandi A *et al.* Targeting stromal-induced pyruvate kinase M2 nuclear translocation impairs oxphos and prostate cancer metastatic spread. Oncotarget 2015;6(27);24061-24074.
194. Olumi AF, Grossfeld GD, Hayward SW *et al.* Carcinoma-associated fibroblasts direct tumor progression of initiated human prostatic epithelium. Cancer Res 1999;59(19);5002-5011.
195. Richards Z, McCray T, Marsili J *et al.* Prostate Stroma Increases the Viability and Maintains the Branching Phenotype of Human Prostate Organoids. iScience 2019;12(304-317.
196. Lubarsky B, Krasnow MA. Tube morphogenesis: making and shaping biological tubes. Cell 2003;112(1);19-28.
197. Rodriguez-Fraticelli AE, Auzan M, Alonso MA *et al.* Cell confinement controls centrosome positioning and lumen initiation during epithelial morphogenesis. J Cell Biol 2012;198(6);1011-1023.
198. Ferrari A, Veligodskiy A, Berge U *et al.* ROCK-mediated contractility, tight junctions and channels contribute to the conversion of a preapical patch into apical surface during isochoric lumen initiation. J Cell Sci 2008;121(Pt 21);3649-3663.
199. Hirashima T, Hoshuyama M, Adachi T. In vitro tubulogenesis of Madin-Darby canine kidney (MDCK) spheroids occurs depending on constituent cell number and scaffold gel concentration. J Theor Biol 2017;435(110-115.
200. Giacomelli MG, Husvogt L, Vardeh H *et al.* Virtual Hematoxylin and Eosin Transillumination Microscopy Using Epi-Fluorescence Imaging. PLoS One 2016;11(8);e0159337.
201. Cahill LC, Giacomelli MG, Yoshitake T *et al.* Rapid virtual hematoxylin and eosin histology of breast tissue specimens using a compact fluorescence nonlinear microscope. Lab Invest 2018;98(1);150-160.
202. Glaser AK, Reder NP, Chen Y *et al.* Light-sheet microscopy for slide-free non-destructive pathology of large clinical specimens. Nat Biomed Eng 2017;1(7).
203. Madabhushi A, Lee G. Image analysis and machine learning in digital pathology: Challenges and opportunities. Med Image Anal 2016;33(170-175.
204. Avenel C, Tolf A, Dragomir A *et al.* Glandular Segmentation of Prostate Cancer: An of How the Choice of Histopathological Stain Is One Key to Success for Computational Pathology. Front Bioeng Biotechnol 2019;7(125.
205. Reder NP, Glaser AK, McCarty EF *et al.* Open-Top Light-Sheet Microscopy Image Atlas of Prostate Core Needle Biopsies. Arch Pathol Lab Med 2019;143(9);1069-1075.
206. Cahill LC, Fujimoto JG, Giacomelli MG *et al.* Comparing histologic evaluation of prostate tissue using nonlinear microscopy and paraffin H&E: a pilot study. Mod Pathol 2019;32(8);1158-1167.
207. Yadav SS, Stockert JA, Hackert V *et al.* Intratumor heterogeneity in prostate cancer. Urologic oncology 2018;36(8);349-360.
208. Gallee MP, Visser-de Jong E, van der Korput JA *et al.* Variation of prostate-specific antigen expression in different tumour growth patterns present in prostatectomy specimens. Urol Res 1990;18(3);181-187.

209. Lotan TL, Heumann A, Rico SD *et al.* PTEN loss detection in prostate cancer: comparison of PTEN immunohistochemistry and PTEN FISH in a large retrospective prostatectomy cohort. Oncotarget 2017;8(39);65566-65576.
210. Zellweger T, Gunther S, Zlobec I *et al.* Tumour growth fraction measured by immunohistochemical staining of Ki67 is an independent prognostic factor in preoperative prostate biopsies with small-volume or low-grade prostate cancer. Int J Cancer 2009;124(9);2116-2123.
211. Ayala G, Frolov A, Chatterjee D *et al.* Expression of ERG protein in prostate cancer: variability and biological correlates. Endocr Relat Cancer 2015;22(3);277-287.